UNIVERSITY OF CALIFORNIA

Santa Barbara

Understanding and Controlling Light Alkane Reactivity on Metal Oxides: Optimization Through Doping

A dissertation submitted in partial satisfaction of the

requirements for the degree

Doctor of Philosophy

in

Chemical Engineering

by

Alan Richard Derk

Committee in charge:

Professor Eric W. McFarland, Co-Chair

Professor Horia Metiu, Co-Chair

Professor Brad Chmelka

Professor Mike Gordon

Professor Galen Stucky

June 2015

The dissertation of Alan Richard Derk is approved.

Brad Chmelka

Mike Gordon

Galen Stucky

Eric McFarland, Co-chair

Horia Metiu, Co-chair

April 2015

Understanding and Controlling Light Alkane Reactivity on Metal Oxides:

Optimization Through Doping

by

Alan Richard Derk

ACKNOWLEDGEMENTS

Research in science is an open-ended journey of exploration, perseverance, and understanding. Like most scientific explorations, the work here would not have been accomplished, or even embarked upon, without the help of many people.

I would first like to express deep gratitude to my Ph.D. advisors, Eric McFarland and Horia Metiu. Eric, your strong encouragement has been absolutely instrumental to my graduate career and time here at UCSB. Your passion for pragmatic technological advancement for the betterment of mankind is inspiring. Horia, your scientific insight, curiosity, and appreciation for chemical history are wonderful. I don't think an experiment was shown without your sharing an insightful historical anecdote! Our times together at UCSB have been very memorable.

Next, I would like to thank the other members of my doctoral committee, Brad Chmelka, Mike Gordon, and Galen Stucky. You have brought unique perspectives and vast insight throughout my UCSB career.

I thank my fellow UCSB graduate students, both in the Department of Chemical Engineering and outside, and group member post-docs for great discussions: In particular, Louis Jones, Brian Giera, Serra Elliott, Matt Aronson, Scott Carmichael, Ches Upham, Kunlun Ding, and Sudhanshu Sharma. To my long-time office mate and friend, Nirala Singh, I thank you for your camaraderie and boundless kindness.

I would also like to thank my housemates, Nathan George, Shamon Walker, Robert Messinger, Mike Villet, Terry Keller, Robin Gee, Sean O'Brien, Heike Shirmer, Sebastian Sovero, Eric Danner, Matt Mock, and Joel Sherman, for the very unique community in which I resided for several years. The countless stimulating conversations, epic adventures,

new experiences, creative inspirations, and strong kinship are truly memories I will have for my lifetime.

I would like to thank the UCSB MRL user facility scientists for their superb training and understanding. Specifically Tom Mates and Stephan Kraemer were nothing short of excellent. I also thank the superb secretaries and staff in the Department of Chemical Engineering, especially Laura Crownover.

I would like to give a special thank you to Lauren Misch. Our wonderful times and adventures together of the past years are truly unforgettable. Thank you for your unending understanding and support.

To my family – my mother, Jane, and sister, Julia, especially, but also my brothers, Peter and Ian, and cousins of Utah, Ben, Jacob, and Katie – I owe you my deepest gratitude. You have forged who I am and any success I may have is due to you.

I would lastly like to extend appreciation for the funding sources, without which my rewarding, albeit challenging, time here at UCSB would have never been feasible. These are the National Science Foundation for a Graduate Research Fellowship and an Integrated Graduate Education Research Traineeship, and the Department of Energy for research funding.

VITA OF ALAN RICHARD DERK

March 2015

EDUCATION

Bachelor of Science in Chemical Engineering (with Honors), University of Colorado, Boulder, May 2009

Doctor of Philosophy in Chemical Engineering, University of California, Santa Barbara, March 2015 (expected)

PROFESSIONAL EMPLOYMENT

2006-08: Undergraduate Researcher, Department of Chemical and Biological Engineering, University of Colorado, Boulder

Summer 2008: Field Engineer Intern, Schlumberger Technology Corporation, Prudhoe Bay, Alaska

Summer 2009: Pre-graduate Researcher, Department of Chemical and Biological Engineering, University of Colorado, Boulder

January 2010-Current, Graduate Researcher, Department of Chemical Engineering, University of California, Santa Barbara

PUBLICATIONS

Derk, A. R., Funke, H. H., & Falconer, J. L. (2008). Methane Conversion to Higher Hydrocarbons by UV Irradiation. *Industrial & Engineering Chemistry Research,* 47 (17), 6568-6572.

Misch, L. M., Kurzman, J. A., Derk, A. R., Kim, Y.-il, Seshadri, R., Metiu, H., McFarland, E. W., et al. (2011). C-H Bond Activation by Pd-substituted CeO_2. *Chemistry of Materials*, 23 (24), 5432–5439.

Ding, K., Derk, A. R., Zhang, A., Hu, Z., Stoimenov, P., Stucky, G., Metiu, H., McFarland, E. (2012) Hydrodebromination and Oligomerization of Dibromomethane. *ACS Catalysis 2 (4), 479-486*

Derk, A. R., Li B., Sharma S., Moore G. M., McFarland E. W., Metiu H. (2013). Methane Oxidation by Lanthanum Oxide Doped with Cu, Zn, Mg, Fe, Nb, Ti, Zr, or Ta: The Connection Between the Activation Energy and the Energy of Oxygen-Vacancy Formation. *Catalysis Letters*, 143 (5), 406–410.

Derk, A. R., Moore G. M., Sharma S., McFarland E. W., Metiu H. (2014) Catalytic dry reforming of methane on ruthenium-doped ceria and ruthenium supported on ceria. *Topics in Catalysis* 57 (1-4), 118-124

Upham, D. C., Derk, A. R., Metiu, H., McFarland, E. W., (2015) CO2 methanation by Ru-doped ceria: The role of the oxidation state of the surface. *Catalysis Science & Technology 3 (5) 1783-1791*

AWARDS

- National Science Foundation Integrative Graduate Education and Research Traineeship Associate, 2011
- National Science Foundation Graduate Research Fellowship, 2010
- Marilyn and Howard L Anseth Outstanding Undergraduate Research Award, 2009
- Engineering Fellow, University of Colorado, Boulder, 2009
- Active Learning Award, College of Engineering and Applied Science, University of Colorado, Boulder 2009

ABSTRACT

Understanding and Controlling Light Alkane Reactivity on Metal Oxides:

Optimization Through Doping

by

Alan Richard Derk

Metal oxide catalysts have numerous industrial applications and have garnered research attention. Although oxides catalyze many important reactions, their yields to products are too low to be of economic value due to low conversion and/or low selectivity. For example, some oxides can catalyze the conversion of methane to intermediates or products that are liquefiable at yields no higher than 30%. With improved yield, such a process could help reduce the trillions of cubic feet of natural gas flared every year, saving billions of dollars and millions of tonnes of greenhouse gases. To this end, one goal of this work is to understand and improve the catalytic activity of oxides by substituting a small fraction of the cations of a "host oxide" with a different cation, a "dopant." This substitution disrupts chemical bonding at the surface of the host oxide, which can improve reactant and lattice oxygen activation where the reaction takes place. Another goal of this work is to combine catalysts with metal oxides reactants to improve thermodynamic limitations. Outstanding challenges for the study of doped metal oxide catalysts include (1) selection of dopants to

synthesize within a host oxide and (2) understanding the nature of the surface of the doped oxide during reaction.

Herein, strongly coupled theoretical calculations and experimental techniques are employed to design, synthesize, characterize, and catalytically analyze doped oxide catalysts for the optimization of light alkane conversion processes. Density Functional Theory calculations are used to predict different energies believed to be involved in the reaction mechanism. These parameters offer valuable suggestions on which dopants may perform with highest yield and activity and why. Synthesis is accomplished using a combination of wet chemical techniques, suited specifically for the preparation of doped (rather than supported or mixed) metal oxide catalysts of high surface area and high reactivity. Characterization is paramount in any doped-oxide investigation to determine if the catalyst under reaction conditions is truly doped or merely small clusters of supported catalyst. With that goal, diffraction, X-ray, electron microscopies, infrared spectroscopy, and chemical probes are used to determine the nanoscopic nature of the catalysts. Additional novel measurement techniques, such as transient oxidation reaction spectroscopy, determined the nature of the active site's oxidation state.

TABLE OF CONTENTS

1. Introduction 1

1.1. Organization of Dissertation 1

1.2. Background 4

1.2.1. Applications of alkane catalysis for energy and chemical production 4

1.2.2. Doped metal oxides as catalysts 5

1.2.3. Oxidative Coupling of Methane 7

1.2.4. Dry Reforming of Methane 8

1.2.5. The Sabatier reaction: CO2 methanation 9

1.3. References 10

2. Methods for Doped Metal Oxide Synthesis and Characterization 12

2.1. Synthesis Introduction 12

2.1.1. Incipient Wet Impregnation 13

2.1.2. Solution Combustion Synthesis 13

2.2. Characterization 14

2.2.1. N_2 Adsorption Isotherms 14

2.2.2. X-Ray Diffraction (XRD) 14

2.2.3. X-Ray Photoelectron Spectroscopy (XPS) 15

2.2.4. Transmission/Scanning Electron Microscopy 15

2.3. Reaction Studies 16

2.3.1. Thermodynamic Considerations 17

2.3.2. Chemical Reaction Kinetics 18

2.3.3. Mass Transfer Considerations 19

2.3.4. Heat Transport Limitations 20

2.4. General Algorithmic Optimization of Reaction Conditions to Maximize Reactor Performance 21
2.4.1. What are ideal conditions? 21
2.4.2. On metrics of reactor performance 22
2.4.3. Optimization algorithm 23
2.5. Computational Chemistry Methods 24
2.6. References 24
3. Catalytic Dry Reforming of Methane on Ruthenium-doped Ceria and Ruthenium supported on Ceria 27
3.1. Introduction 27
3.2. Experimental 28
3.2.1. Catalyst Synthesis 28
3.2.2. Catalyst Characterization 30
3.2.3. Reactivity Characterization 30
3.3. Results and Discussion 32
3.3.1. Catalyst Characterization 32
3.3.2. Catalyst Reactivity 37
3.3.3. Why Does Methane React with CO_2 at Lower Temperature than with Oxygen? 41
3.4. Conclusions 44
3.5. References 50
4. CO_2 Methanation by Ru-doped Ceria: The Role of the Oxidation State on the Surface 53
4.1. Introduction 53

4.2. Experimental 54
4.2.1. Catalyst Preparation 54
4.2.2. Reactors 55
4.2.3. Experimental Techniques 56
4.3. Results and Discussion 57
4.3.1. Three states of the $Ru_{0.05}Ce_{0.95}O_2$ Catalyst 57
4.3.2. The Mechanism of Steady-state Methanation Reaction on the SSC 58
4.3.3. IR Detection of Surface Carbonates 65
4.3.4. The Chemistry of the Oxidized Catalyst (OC) 71
4.3.5. The Chemistry of the SRC Surface 72
4.4. Conclusion 75
4.5. References 77
5. Methane Oxidation by Lanthanum Oxide Doped with Cu, Zn, Mg, Fe, Nb, Ti, Zr, or Ta: The Connection Between the Activation Energy and the Energy of Oxygen-vacancy Formation 82
5.1. Introduction 82
5.2. DFT Calculation Methodology 84
5.3. Experimental Methodology 84
5.4. Results and Discussion 86
5.5. References 92
6. Catalyst and Oxygen Carrier Compatibility Oxidative Dehydrogenation of Alkanes 94
6.1. Introduction: Benefits and goals of a SHC Solid Reactant 94
6.2. Experimental 97

6.2.1. Synthesis 97
6.2.2. Reactor studies 98
6.2.3. X-Ray Photoelectron Spectroscopy 99
6.3. Results and discussion 100
6.3.1. Selective Hydrogen Combustion by Bi_2O_3/SBA-15 100
6.3.2. Oxidative dehydrogenation of propane using a platinum-based dehydrogenation catalyst and Bi_2O_3/SBA-15 for selective hydrogen combustion 102
6.3.3. Oxidative dehydrogenation of propane using a chromium-based dehydrogenation catalyst and Bi_2O_3/SBA-15 for selective hydrogen combustion 107
6.4. Conclusions 111
6.5. Acknowledgements 112
6.6. Supplemental information 113
6.7. References 115
Appendix A: Hydrodebromination and Oligomerization of Dibromomethane 118
Results and Discussion 121
Conclusions 136
References 137
Appendix B: C-H Bond Activation by Pd-substituted CeO_2 : Substituted Ions versus Reduced Species 140
Introduction 140
Experimental Section 142
Results and Discussion 145
Characterization of $Ce_{1-x}Pd_xO_{2-\delta}$ 145
Reactivity Studies 156

References 164

1. Introduction

1.1. Organization of Dissertation

This dissertation describes the investigation of light alkane reactivity on metal oxides optimized through doping. First, it provides a background into the immense opportunity provided by improving the currently exorbitantly wasteful natural gas production. Secondly, it covers a means to this end -- alkane activation over doped metal oxides -- providing motivation and reviewing the state of the art (Chapter 1). The subsequent section (Chapter 2) explains the methods and techniques employed to elucidate and optimize chemical reactivity of the doped-metal oxide, and the nature thereof. With this requisite information covered, three foci are explored: (1) understanding dry reforming and CO_2 methanation on a doped catalyst (Chapters 3 and 4); (2) discovering a promising link between experimentally-derived activation energies and theoretically-predicted vacancy formation energies for new catalyst design (Chapter 5); and (3) augmenting dehydrogenation yields from traditional catalysts using additional metal oxides as solid sources of oxygen for hydrogen combustion (Chapter 6).

Chapter 1 presents an overview of alkane activation reactions (both industrial and academic), specifically with regard to doped metal oxide catalysis – its motivation, history and the state-of-the-art. Additionally, challenges unique to doped metal oxides are considered. The majority of the work discussed in this dissertation is on doped metal oxides and this chapter provides a basis to understand the subsequent chapters.

Chapter 2 elaborates on the background provided by the previous chapter, explaining the methods used in this work to interrogate the relevant physical phenomena which doped

metal oxides exhibit. These methods include adsorption-, diffraction-, and photoelectron-based instrumental techniques to characterize the catalysts. Theoretical techniques, including density functional theory, are discussed as they apply to predicting and understanding doped metal oxide catalysts. Another method explained is the reaction condition optimization capabilities of a reactor built in-house and the associated LabView-based software. Given a catalyst, the optimization routines can maximize an arbitrary fitness function based on reactant flows, effluent flows, and temperature. Appropriate fitness functions are discussed and optimized results compare favorably to results from literature. The question of, "Can reactor conditions be algorithmically optimized?" is answered. Also discussed are two of the governing phenomena during reaction testing: chemical kinetics and thermodynamics.

Chapter 3 investigates two types of Ru–ceria catalysts: one prepared by combustion to create an atomically doped metal oxide, and the other, prepared by impregnation, as supported Ru oxide. They have different physical properties (as measured by X-ray photoelectron spectroscopy, X-ray diffraction, and IR spectra of adsorbed CO), but identical catalytic activity for dry reforming of methane. Spectrographic results indicate that the catalyst for dry reforming is partially reduced using XPS and IR spectroscopy. Furthermore, transient oxidation reaction spectroscopy with oxygen pulses confirms partial reduction of the catalyst is necessary for dry reforming activity. Through understanding the role of surface reduction for C-H bond activation, this motivating question is answered: on ruthenium-doped ceria, why does CH_4 react with carbon dioxide at a lower temperature than molecular oxygen?

Chapter 4 shows $Ru_{0.05}Ce_{0.95}O_x$ is an active catalyst for methanation of CO_2 with H_2 and answers the question, what is the role of oxidation state for methanation on ruthenium-doped

ceria? Under reaction conditions one expects that oxygen vacancies are present on the oxide catalyst surface and that their steady-state concentration depends upon the relative ratio of the oxidant (CO_2) to the reductant (H_2). Results show the activity of the catalyst is sensitive to the degree of surface reduction: a surface that is too reduced or too oxidized loses activity. Exposing the oxidized surface to CO_2 and then to H_2 produces no methane, while on a reduced surface methane is produced by exposure to CO_2 followed by H_2. If the reaction is carried out at the steady state, purged, and then exposed to only hydrogen, methane is produced. Methane is formed through the reaction of hydrogen with surface species, whose infrared spectrum is associated with a variety of surface carbonates, and not through CO or a formate intermediate.

Chapter 5 answers the following critical question for combined DFT and experimental work: what DFT-calculated values can be used to guide dopant selection in lanthanum oxides for methane activating doped metal oxide catalysts? It explores the measurement of the effective activation energy of methane oxidation catalyzed by La_2O_3 doped with Cu, Zn, Mg, Fe, Nb, Ti, Zr, or Ta. The data shows that the measured activation energy is a linear function of the calculated energy of oxygen-vacancy formation. One hopes that in spite of the associated uncertainties in the trend (obtained by performing the same reaction, catalyzed by the same host oxide, doped with a variety of dopants) is robust and can serve as a guide for designing new doped oxide catalysts.

Chapter 6 discusses selective hydrogen combustion using metal oxides as reactants to compliment dehydrogenation catalysts and answers the following question: what makes a useful solid reactant for ODH and how can they augment alkane dehydrogenation processes? The results show an increase in alkene yield, which would be thermodynamically

unobtainable without the use of certain metal oxides. Furthermore, the results of compatibility investigations of selective hydrogen combustion with chromia- or platinum-tin-based catalysts are analyzed and discussed.

1.2. Background

1.2.1. Applications of alkane catalysis for energy and chemical production

Catalysis has the transformative potential to convert much of our petroleum-based infrastructure to one based on abundant methane (and associated light alkanes). Currently, production of methane far outweighs the consumption, resulting in 5.3 trillion SCF being flared or vented across the globe in 2011 (valued at 30 billion USD or 30% of US consumption)[1]. Furthermore, bio-derived sources of methane exist at landfills, anaerobic waste digesters, and elsewhere. Conversion of methane to useful chemical products is commercially practiced at only a few facilities throughout the world. This is done by first reacting methane to synthesis gas (carbon monoxide and hydrogen) and subsequently reacting the synthesis gas to hydrocarbons or methanol. The latter of which is comparatively easy, with synthesis gas production accounting for ca. 60% of plant cost[2] due to high temperatures and pressures. Although this process is energetically and capitally expensive, to date no other chemical technologies have been commercialized for gas-to-liquids (GTL). As oil reserves become more expensive and polluting to produce, new technologies exploiting the advantages of methane will become more economically competitive and widespread. Lower energy requirements would not only greatly improve these processes, but would also allow for the economical transportation of "stranded gas" from remote wells as a value-added, liquefied product. As a result, robust methane-activating catalysts working at moderate-conditions could have a profound effect on the society's energy sources and

transportation fuels. The specific reactions to harness this potential, and promising catalysts to perform such reactions, are described below.

1.2.2. Doped metal oxides as catalysts

Metal oxide catalysts are used industrially for many reactions.[3] There are many studies for different important reactions, although their conversion or selectivity is too low to be economically useful.[4] Doped metal oxides are oxides whereby lattice ions are substituted, usually one metal cation for another metal cation. The undoped oxide is referred to as the "host oxide". The catalytic activity is affected by the disruption of the chemical bonding at the surface of the catalyst, which can then activate an adsorbing molecule (e.g., methane). Although much is known about doped metal oxides for various applications (electronic materials, sensors, fuel cells, and magnetic materials), they have not been well-studied for catalytic applications.

Most metal-oxide-catalyzed oxidation reactions are believed to proceed via the Mars and van Krevelen (MvK) mechanism[5]. (This mechanism is in contrast to more typically seen mechanisms on metals, such as Langmuir-Hinshelwood where essentially both reactants adsorb, react to products, and desorb.) In the MvK mechanism, at least two reactants are flowed into the reactor, one reducing (e.g., hydrocarbons, carbon monoxide, or hydrogen) and one oxidizing (e.g., oxygen, water, carbon dioxide). The reductant is oxidized by the catalyst surface's lattice oxygen, which introduces an oxygen vacancy at the catalyst surface. Subsequently, another reactant reoxidizes the catalyst to fill the vacancy. The reoxidation is generally, although not always, very fast relative to the reduction; hence, the reduction of the catalyst step is rate-limiting (this is especially true when the reduction requires a carbon-hydrogen bond breaking step). Therefore, to improve catalytic activity, the

kinetic and thermodynamic propensity of a metal oxide catalyst to form oxygen vacancies is a key parameter. This has been thoroughly evaluated by Sauer, et al. in their review of metal oxide surface defects.[5]

Since the 1950s, it has been known dopants affect metal oxide reactivity when Parravano reacted hydrogen with doped nickel oxides[7]. In 1966, Cimino first demonstrated a doped catalyst (nickel (II) oxide doped with magnesium) to be more active at performing a reaction (N_2O decomposition)[8]. Although doping was desirable, it is difficult to tell if the material is truly doped or actually dopant oxide on the bulk oxide or metallic dopant on the bulk oxide surface. Likely, many oxide catalysts have been doped due to adventitious impurities, although these unintentional impurities were not studied explicitly. In other cases, such as industrial catalysis, many additives, such as promoters, may have functioned as unintentional doped-oxide catalysts. In 2002, Cimino and Stone reviewed doped metal oxide catalysis reporting only a few known examples[9]. Since then, many more examples have appeared (especially from the group of Hegde[10–14]), although the number of examples is small when compared to other classes of heterogeneous catalysts.

Doping is believed to promote the MvK mechanism by making the oxygen from the catalyst lattice more labile for reaction[15]. This comes from two effects. One, the environment around the oxygen is perturbed and the oxygen atom becomes more active for oxidation. Secondly, the Fermi level of the catalyst is changed by doping, which changes the thermodynamics of surface oxygen vacancy formation. Dopant effects can also be mitigated or even negated through changes in the surface functionality (in a process called the compensation effect). Such examples include surface hydroxylation of lanthanum-doped ceria and magnesium dopants in lanthanum oxide[15]. Hence through doping, metal-oxide

catalysts can have their high-temperature requirements lowered although surface processes can complicate the situation through the compensation effect.

1.2.3. Oxidative Coupling of Methane

Many aspects of oxidative coupling of methane (OCM) make it an ideal reaction for producing higher hydrocarbons from methane, including being thermodynamically irreversible and producing products directly, avoiding synthesis gas as an expensive intermediate as in the Fischer-Tropsch process. OCM comprises (heterogeneous) catalytic reactions and homogenous reactions of radicals in the gas phase, owing to the high temperatures of 1000 to 1200K[16]. In OCM, methane and oxygen are combined to form ethane, ethylene, and water. The products of carbon oxides are undesirable. Once the formation of the radicals is initiated on a catalytic surface, gas-phase reactions are believed to dominate: Methyl radicals recombine to form ethane (which can be further dehydrogenated). Methoxy species are thought to inexorably react to undesirable carbon oxides.[16] As a consequence of the high temperature conditions causing radical, homogenous reactions, yield of hydrocarbons is limited irrespective of the heterogeneous catalyst sites. Detailed analysis by Labinger has shown that OCM above certain temperatures may be fundamentally limited to yields of ~30%, irrespective of catalyst[17]. Hence, a high-performance OCM catalyst should initiate the formation of methyl radicals at low temperature (and not catalyze the formation of the carbon oxides), to avoid gas-phase reactions controlling and limiting the yield of higher hydrocarbon products. A wide variety of oxide catalysts have been studied, however achieving high yield has proved elusive.[9,16,18,19]

Magnesium oxide and lanthanum oxide based catalysts have been the most promising[19]. A commonly proposed mechanism for the reaction involves lattice oxygen, suggesting lattice-based dopants may be able to improve the reaction and lower the high temperatures normally required. In Chapter 5, a combination of experiment and theory work in tandem to elucidate a dopant in lanthanum that activates methane at as low of a temperature as possible in the hopes of enabling high-yield OCM.

1.2.4. Dry Reforming of Methane

Dry reforming of methane ($CO_2 + CH_4 \rightarrow 2\ CO + 2\ H_2$) is an interesting reaction for synthesis gas production because methane is oxidized with what is usually either a waste product or found naturally in the methane feedstock: carbon dioxide. Methane is usually reformed to syngas by reaction with steam[20], which requires water and methane purification. Furthermore, carbon dioxide and methane are the two strongest greenhouse gases, giving their conversion to other use products a large environmental advantage. The reaction has been studied over noble metals[21], nickel[22], and oxides[23] – but not on intentional doped oxides. The main drawback of carbon dioxide over steam is the strong thermodynamic potential to form coke (carbonaceous deposits which deactivate the catalyst). Industrial catalysts must last several years on-stream to be cost-effective, and extensive time-on-stream studies are necessary.

The mechanism of dry reforming, even on relatively simple catalysts such as platinum group metals, is debated[23–26]. For hybrid systems composed of oxides and metal oxides, two-site mechanisms have been proposed.[22]

Rostrup-Nielsen *et al.* performed a comprehensive investigation on this reaction in 1993 when they catalytically tested and characterized silica-supported nickel, ruthenium,

rhodium, palladium, iridium, and platinum catalysts[27]. Ruthenium catalyzed dry reforming well, as compared to the other metals, with the highest turnover number and no measurable coke formation. Ruthenium with ceria has been studied although questions still remain. Safariamin *et al.* studied ruthenium supported on alumina, ceria, and combinations thereof[28]. They found ceria increased the dry reforming activity. Dry reforming over ruthenium-ceria supported on mordenite was found to be very active with no coke formation by Hashimoto *et al.*[29]

1.2.5. The Sabatier reaction: CO2 methanation

The Sabatier reaction, discovered by Paul Sabatier in the 1910s, involves the reaction of hydrogen with carbon dioxide to form methane and water. The reactants can also perform reverse water gas shift to form carbon monoxide and water. Temperatures in the range of 300 to 400 ^{o}C are generally used[30]: With a higher temperature, the thermodynamics become less favorable leading to less conversion and a stronger driving force for carbon monoxide production. This reaction is not used in a large scale, but has been proposed for the consumption of CO_2 to reduce greenhouse gas emissions. Additionally, the reaction is of interest to NASA for the purposes of space exploration. CO_2 produced by human metabolic processes needs to be removed from manned spacecraft. Most mission vent the carbon dioxide to space, but this requires the electrolysis of water to replenish oxygen in the cabin atmosphere. The conversion of carbon dioxide to water and methane closes the oxygen cycle; the methane can subsequently be used for propellant. Nickel-based catalysts are the most commonly used[31], although ruthenium[32], rhodium[32], and doped oxides[33] have been explored as well.

1.3. References

1. Global Gas Flaring Reduction Partnership - The World Bank. *http://go.worldbank.org/425VOGDYS0* (2015).

2. Rostrup-Nielsen, J. Syngas in perspective. *Catal. Today* **71,** 243–247 (2002).

3. Bartolomew, C. H. & Farauto, R. J. *Fundamentals of Industrial Catalytic Processes*. (John Wiley & Sons, 2006).

4. McFarland, E. W. & Metiu, H. Catalysis by doped oxides. *Chem. Rev.* **113,** 4391–427 (2013).

5. Ganduglia-Pirovano, M. V., Hofmann, A. & Sauer, J. Oxygen vacancies in transition metal and rare earth oxides: Current state of understanding and remaining challenges. *Surf. Sci. Rep.* **62,** 219–270 (2007).

6. Mars, P. & van Krevelen, D. W. Oxidations carried out by means of vanadium oxide catalysts. *Chem. Eng. Sci.* **3,** 41–59 (1954).

7. Parravano, G. The reduction of nickel oxide by hydrogen. *J. Am. Chem. Soc.* **74,** 1194–1198 (1952).

8. CIMINO, A., BOSCO, R., INDOVINA, V. & SCHIAVELLO, M. Decomposition of nitrous oxide upon nickel oxide-magnesium oxide solid solutions. *J. Catal.* **5,** 271–278 (1966).

9. Cimino, A. & Stone, F. S. *Advances in Catalysis Volume 47*. **47,** (Elsevier, 2002).

10. Gupta, A., Waghmare, U. V. & Hegde, M. S. Correlation of Oxygen Storage Capacity and Structural Distortion in Transition-Metal-, Noble-Metal-, and Rare-Earth-Ion-Substituted CeO 2 from First Principles Calculation. *Chem. Mater.* **22,** 5184–5198 (2010).

11. Singh, P., Hegde, M. S. & Gopalakrishnan, J. Ce 2/3 Cr 1/3 O 2+y : A New Oxygen Storage Material Based on the Fluorite Structure. *Chem. Mater.* **20,** 7268–7273 (2008).

12. Chakraborty, K. R., Krishna, P. S. R. & Hegde, M. S. Neutron scattering study of combustion-synthesized Ce1−x Cu x O2−x. *Pramana* **63,** 245–249 (2004).

13. Bera, P. *et al.* Structural Investigation of Combustion Synthesized Cu/CeO 2 Catalysts by EXAFS and Other Physical Techniques: Formation of a Ce 1 - x Cu x O 2- δ Solid Solution. *Chem. Mater.* **14,** 3591–3601 (2002).

14. Singh, P. & Hegde, M. S. Ce 1− x Ru x O 2−δ (x =0.05, 0.10): A New High Oxygen Storage Material and Pt, Pd-Free Three-Way Catalyst. *Chem. Mater.* **21,** 3337–3345 (2009).

15. Hu, Z., Li, B., Sun, X. & Metiu, H. Chemistry of Doped Oxides: The Activation of Surface Oxygen and the Chemical Compensation Effect. *J. Phys. Chem. C* **115,** 3065–3074 (2011).

16. Zavyalova, U., Holena, M., Schlögl, R. & Baerns, M. Statistical analysis of past catalytic data on oxidative methane coupling for new insights into the composition of high-performance catalysts. *ChemCatChem* **3,** 1935–1947 (2011).

17. Labinger, J. A. Oxidative coupling of methane: An inherent limit to selectivity? *Catal. Letters* **1,** 371–375 (1988).

18. Sun, J., Thybaut, J. & Marin, G. Microkinetics of methane oxidative coupling. *Catal. Today* **137,** 90–102 (2008).

19. Wang, D. Oxidative Coupling of Methane over Oxide-Supported Sodium-Manganese Catalysts. *J. Catal.* **155,** 390–402 (1995).

20. Aasberg-Petersen, K. Technologies for large-scale gas conversion. *Appl. Catal. A Gen.* **221,** 379–387 (2001).

21. bak hansen, J.-H. & Rostrup-Nielsen, J. R. CO2-reforming of methane over transition metals. *J. Catal.* **144,** 38–49 (1993).

22. Gallego, G. S., Batiot-Dupeyrat, C., Barrault, J. & Mondragon, F. Dual Active-Site Mechanism for Dry Methane Reforming over Ni/La2O3 Produced from LaNiO3 Perovskite. *Ind. Eng. Chem. Res.* **47,** 9272–9278 (2008).

23. Bradford, M. & Vannice, M. CO2 reforming of CH4. *Catal. Rev. Sci. Eng.* **41,** 1–42 (1999).

24. Avetisov, A. K. *et al.* Steady-state kinetics and mechanism of methane reforming with steam and carbon dioxide over Ni catalyst. *J. Mol. Catal. A Chem.* **315,** 155–162 (2010).

25. Wang, S., Lu, G. Q. (Max) & Millar, G. J. Carbon Dioxide Reforming of Methane To Produce Synthesis Gas over Metal-Supported Catalysts: State of the Art. *Energy & Fuels* **10,** 896–904 (1996).

26. O'Connor, A. M., Schuurman, Y., Ross, J. R. H. & Mirodatos, C. Transient studies of carbon dioxide reforming of methane over Pt/ZrO2 and Pt/Al2O3. *Catal. Today* **115,** 191–198 (2006).

27. Rostrup-Nielsen, J. R. & Bak Hansen, J.-H. CO2-Reforming of Methane over Transition Metals. *J. Catal.* **144,** 38–49 (1993).

28. Safariamin, M., Tidahy, L. H., Abi-Aad, E., Siffert, S. & Aboukaïs, A. Dry reforming of methane in the presence of ruthenium-based catalysts. *Comptes Rendus Chim.* **12,** 748–753 (2009).

29. Hashimoto, K., Watase, S. & Toukai, N. Reforming of methane with carbon dioxide over a catalyst consisting of ruthenium metal and cerium oxide supported on mordenite. *Catal. Letters* **80,** 147–152 (2002).

30. Chen, A., Miyao, T., Higashiyama, K., Yamashita, H. & Watanabe, M. High Catalytic Performance of Ruthenium-Doped Mesoporous Nickel-Aluminum Oxides for Selective CO Methanation. *Angew. Chem. Int. Ed. Engl.* 9895 –9898 (2010). doi:10.1002/anie.201005650

31. Abe, T., Tanizawa, M., Watanabe, K. & Taguchi, A. CO2 methanation property of Ru nanoparticle-loaded TiO2 prepared by a polygonal barrel-sputtering method. *Energy Environ. Sci.* **2,** 315 (2009).

32. Junaedi, C. *et al.* Compact and Lightweight Sabatier Reactor for Carbon Dioxide Reduction. *41st Int. Conf. Envionmental Syst.* 1–10 (2011). doi:doi:10.2514/6.2011-5033

33. Sharma, S., Hu, Z., Zhang, P., McFarland, E. W. & Metiu, H. CO2 methanation on Ru-doped ceria. *J. Catal.* **278,** 297–309 (2011).

2. Methods for Doped Metal Oxide Synthesis and Characterization

2.1. Synthesis Introduction

There are many methods for metal oxide catalyst synthesis, some of which are applicable to forming doped metal oxide catalysts. These syntheses need to avoid forming impure phases such as the dopant oxide as a cluster. With all syntheses, it is difficult to prove a dopant has been incorporated into the lattice of the host oxide, especially at the surface or subsurface layers. These small clusters of dopant oxide are difficult to detect and can have reactivity different from the host oxide and the native dopant oxide[1,2]. As a result, determining between doped oxides and other catalyst systems is a challenge. To exacerbate

the difficulty, it is possible for an as-prepared catalyst to be doped, but reversibly change under reaction conditions, to a supported oxide catalyst.

2.1.1. Incipient Wet Impregnation

This technique is useful for producing both supported catalysts (usually metals or metal oxides supported on metal oxides) and some doped oxides. The host oxide is added to a minimal amount of aqueous solution of the added dopant or catalyst. The mixture is then dried and calcined. When the intent is to produce a supported oxide, the calcination temperature is kept low to prevent the dopant cations from diffusing into the host oxide. On the other hand, when the intent is to produce a doped oxide, calcination temperature is increased to encourage diffusion of the dopant into the surface layers of the host oxide. In this regard, incipient wet impregnation is a form of solid high-temperature synthesis, although the dopant precursors are so much smaller for incipient wet impregnation that in practice they are performed very differently (calcination temperatures and times are much longer, on the order of 1000 ^{o}C and days, for solid high-temperature synthesis).

2.1.2. Solution Combustion Synthesis

Solution combustion synthesis (SCS) is a versatile, simple, and rapid process which can produce a multitude of nano-scale materials[3], usually for applications in catalysis or photo-luminescent materials. To produce doped oxides, a homogenous aqueous solution of metal precursors (usually nitrates[4]) and a "fuel" (*e.g.,* urea[5], carbohydrates[3], or glycine[6]) are heated at moderate temperature (ca. 300 ^{o}C) to start boiling of the solvent and then combustion of the oxidizing salts with the fuel. Metal oxide particles are produced in the reaction with by-products of water, nitrogen gas, carbon dioxide, and others, depending on

precursor. For most syntheses, stoichiometric amounts of oxidizer (metal nitrates plus any additional oxidizer, such as ammonium nitrate) and fuel are used to produce the aforementioned products.

2.2. Characterization

2.2.1. N_2 Adsorption Isotherms

Surface area and pore diameters of synthesized catalysts were calculated using N_2 adsorption acquired on a Micrometrics Tristar 3000. To extract meaningful results from the isotherm data, Brunauer-Emmett-Teller (BET) and Barret-Joyner-Halenda (BJH) theories of adsorption were applied.

2.2.2. X-Ray Diffraction (XRD)

X-Ray Diffraction was used to determine crystallographic phases present based on the X-Ray reflections present. This is accomplished via Bragg's law. In this work, data was collected using two different X-Ray diffractometers. The more common of which was copper Kα radiation using a Philips XPERT MPD. Additional, high-resolution data was collected at Argonne National Lab's 11-BM synchrotron-source X-ray diffractometer with 30 keV X-rays. No evidence of sample degradation or damage was observed. Reitveld refinement was performed in order to determine phase compositions and peak widths using GSAS and EXPGUI[7,8]. Reitveld refinement involves minimizing the sum-squared-error between model-derived, calculated spectra and the experimental data points. Upon refinement, the fully-understood model is used as a proxy for the sample. For example, the Scherrer broadening equation was used for crystallite-size determination. Instrumental

broadening was accounted for when using copper Kα radiation (of 0.1º FWHM), but not for synchrotron radiation.

2.2.3. X-Ray Photoelectron Spectroscopy (XPS)

This technique is widely used for catalyst analysis, including doped metal oxide catalysts. The instrument operates in vacuum and subjects samples to monochromatic X-rays. These X-rays eject core electrons from the sample. By measuring these photo-emitted core electron's kinetic energy, one can determine chemical and elemental information from the outermost 1-10 nm of the sample.

X-ray photoelectron spectroscopy was used to determine surface concentrations of atomic species as well as to infer their oxidation state from the core-level binding energies. The measurements were performed on a Kratos Axis Ultra XPS using Al K_α radiation. To account for charging due to samples being electrical insulators, a charge neutralizer was employed and spectra were shifted to move the (adventitious) C (1s) peak to 285.0eV BE. Signal-to-noise ratios were poor for many dopants and the hemi-spherical analyzer required a large pass-energy of 80eV to achieve good statistics. As an unfortunate consequence, the peaks have been broadened slightly (likely instrumental broadening is 1.1eV FWHM). An additional source of error for calculating cerium and ruthenium oxidation states is their oxides partially reduce under XPS conditions[9,10].

2.2.4. Transmission/Scanning Electron Microscopy

Transmission/Scanning Electron Microscopy (TEM/SEM) was used to characterize catalysts as-synthesized and after catalysis to evaluate particle size, dopant location, and the effects of possible coking reactions. TEM micrographs were recorded with a FEI-Technai

G2 Sphera Microscope operating at 200 kV. SEM Micrographs were recorded with a FEI XL30 Sirion FEG Digital Electron Scanning Microscope operating at 12 kV.

2.3. Reaction Studies

Catalytic testing was performed in a (6mm ID) quartz-tube micro-reactor. The reactor's gas feed system is computer-controlled by Mass Flow Controllers (MFCs). The reactor is heated using electrical heaters and an externally-insulated stainless-steel block. Gas analysis is done by a differentially pumped mass spectrometer with a linear-algebra-based peak-deconvolution algorithm (Carbon, oxygen, and hydrogen steady-state atom balances are usually accurate to 1%). Control of temperature, feed-gas composition, and effluent gas analysis is integrated and automated by LabView software (see Figure 1). The temperature was controlled by a temperature controller (Omega CSC32) using a steel reactor block with heating cartridges that surrounded the reactor tube and pre-heated the gases. A thermocouple in the heating block controlled the temperature and the difference between the steady state bed temperature and the block temperature was less than 5 °C at all relevant temperatures. This was determined by measurement in an inert bed. All experiments were carried out at atmospheric pressure.

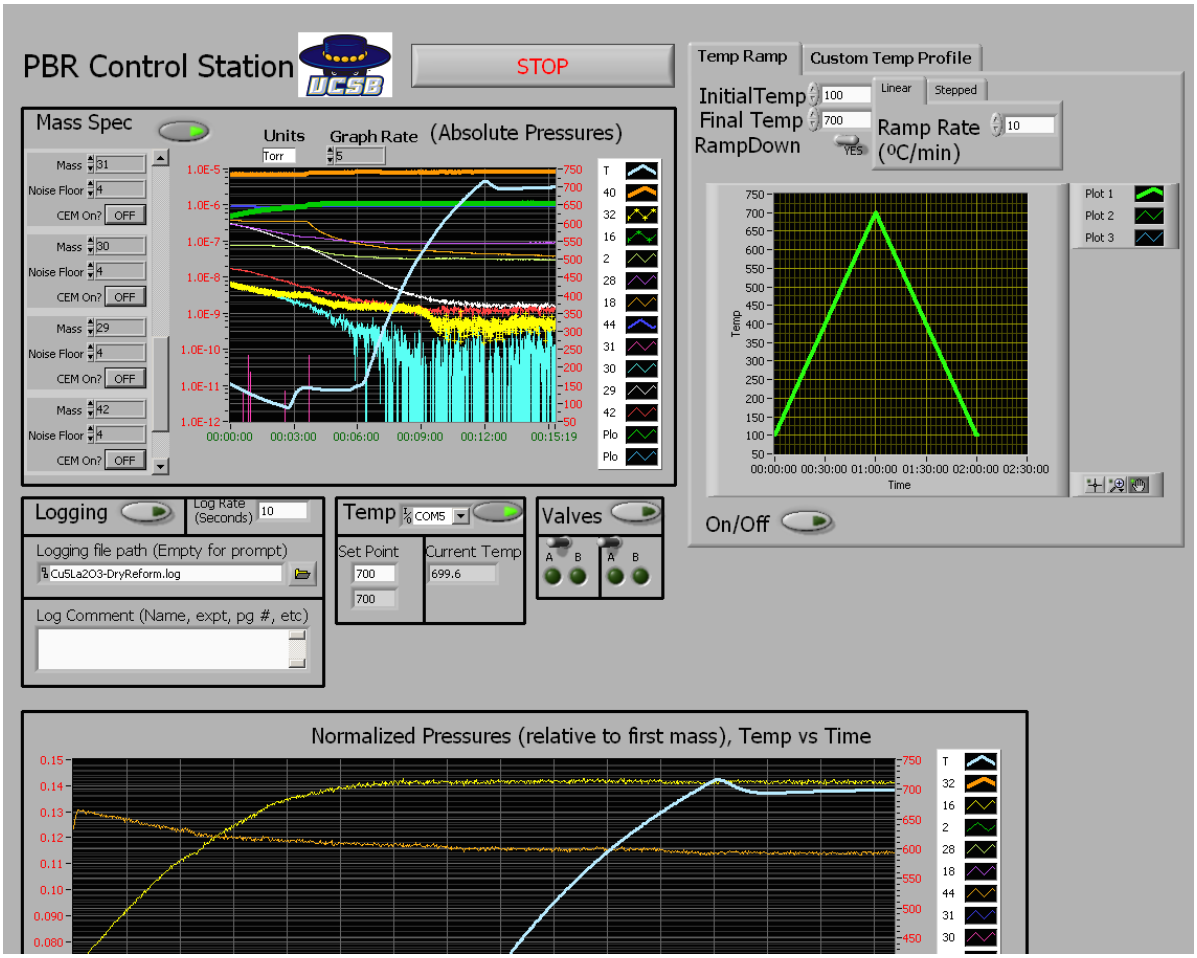

Figure 1. Frontend display of LabView software built to integrate catalytic testing by synchronizing mass spectrometer, temperature control, valving, and data logging.

When performing analysis on any chemical reaction – especially for catalytic or heterogeneous reactions – there are three classes of phenomena which dominate: reaction thermodynamics, reaction kinetics, and mass/heat transport limitations. Due to non-linear inter-dependencies between the respective differential equations, highly coupled phenomena result, as follows.

2.3.1. Thermodynamic Considerations

Ultimately, chemical potential is the driving force for any reaction and controls all catalytic processes. The equilibrium constant for a reaction is defined as follows:

$$K_{eq}(T) = \prod P_i^{v_i} = \exp(-\Delta G/RT)$$

Where P_i is the fugacity of reaction species i, $v_i$the stoichiometric coefficient (negative for reactant) of reaction species i, ΔG is the Gibbs free energy of reaction, and RT is the product of the gas constant with temperature. Chemical concentration equilibrium for multiple reactions can be calculated from individual reaction equilibrium constants using a method such as extent of reaction and performing a non-linear minimization to ensure each individual reaction's equilibrium is satisfied.

2.3.2. Chemical Reaction Kinetics

The catalyst-testing reactor is assumed to be a packed-bed reactor (PBR). The PBR model is a reactor in which there are no gradients in concentration, temperature, or reaction rate in the radial direction. In the axial direction, on the other hand, diffusion is negligible and the reactor's aforementioned key parameters change continuously leading to a differential material and energy balance on a circular slice through the reactor[11]:

$$\frac{dF_j}{dW} = \frac{-\sum r'_{ij}}{F_{j0}}$$

$$\frac{dT}{dW} = \frac{Q + \sum r'_{ij} \Delta H_{Rxij}}{\sum F_i Cp_i}$$

F_j is the molar flow-rate of species j, F_{j0} is the molar flow-rate of species j at the entrance, W is the catalyst weight (proportional to length in axial direction), r'_{ij} is the reaction rate for species j and reaction i normalized to catalyst weight, Q is the differential heat flow-rate into the reactor, and ΔH_{Rxij} is the enthalpy of reaction for reaction i. With mass balances specified, conversion (varying from 0 to 1) is defined for reactant j, X_j.

Similarly, the selectivity of product j with respect to product k, S_{jk}, is defined. The yield of j with respect to (usually limiting) reactant k, Y_{jk}, is defined as the following.

$$X_j = 1 - \frac{F_j}{F_{j0}} \qquad S_{jk} = \frac{F_j}{F_j + F_k} \qquad Y_{jk} = \frac{F_j}{F_{k0} - F_k}$$

The activity is defined as the moles of reactant consumed per second per catalyst active site (which in practice is difficult to measure):

$$activity = \frac{F_{k0} - F_{k,exit}}{\#\ sites}$$

2.3.3. Mass Transfer Considerations

For measuring intrinsic catalytic kinetics in heterogeneous catalysis, mass transfer limitations must be addressed. There are different sources of mass transfer limitations, namely from the bulk fluid to the external surface of the catalyst pellet and from the surface of the pellet to the core of the pellet, call the external and internal mass-transfer, respectively. With small particles and a fast flow-rate (and hence a high Schmidt number), very rarely is the external surface of the catalyst mass-limiting. Oftentimes, the internal mass transfer limitation can be quantified using the Thiele modulus and effectiveness factor, as follows.

$$\eta = \frac{Actual\ overall\ reaction\ rate}{\begin{array}{c} rate\ of\ reaction\ that\ would \\ result\ if\ entire\ surface \\ were\ exposed\ to\ the\ extrnal\ pellet \\ surface\ conditions \end{array}}$$

The Thiele modulus is the ratio of the reaction rate to the diffusion rate in the particle, hence when diffusion is fast, the concentration is uniform throughout and the effectiveness

factor is one. Otherwise the overall reaction rate quickly decreases as reactant concentrations rapidly decline. To measure intrinsic kinetics, the reaction must be limiting, meaning a small Thiele modulus. Although the equations listed are for spherical pellets, the Thiele modulus changes very little with respect to geometry and the equations are still fairly accurate for other shapes. Internal mass transfer limitations can certainly obscure a catalyst's properties, especially if measuring intrinsic rate constants. In 1971, Mears developed criteria for testing for mass transfer limitations which can elucidate if catalyst is diffusion or reaction limited[12].

2.3.4. Heat Transport Limitations

Applying the same formalism as mass-transport to heat-transport reiterates the highly-coupled nature between transport and kinetics, as follows by first defining two dimensionless groups.

$$\gamma_A = \frac{E}{RT_S} \qquad \beta_T = \frac{\Delta T_{Max}}{T_S}$$

γ_A is known as the Arrhenius number and is a dimensionless activation energy. Likewise, β_T is a dimensionless group, which represents the maximum-possible temperature change within the particle. T_S is the temperature at the catalyst particle's surface. Once again, these results show the ability of heat transfer to strongly obscure intrinsic catalyst studies. Additionally, this methodology describes "hot spot" behavior quantitatively. Furthermore, this analysis did not include the effect of temperature on thermodynamical equilibrium, which, if included, would likely introduce further anomalous behavior. Mears, as with mass-transfer limitations, developed a criterion for testing for heat-transfer limitations[13]. Notably, Mears demonstrates adding catalyst-bed diluent does not reduce

hotspot formation due to the low amount of inter-particle heat transfer as compared to particle-fluid.

2.4. General Algorithmic Optimization of Reaction Conditions to Maximize Reactor Performance

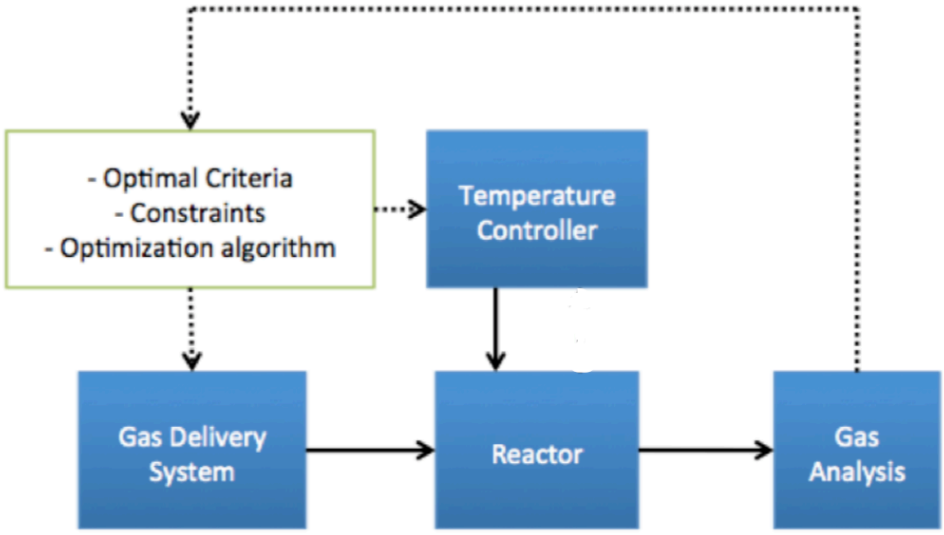

Figure 2. Schematic of the reactor software (upper left) receiving gas analysis data and controlling reactor parameters (shown in dotted lines). Physical flows (gas and power) are show in solid lines. The software considers the performance metric and maximizes it by employing the optimization algorithm.

2.4.1. What are ideal conditions?

The optimum reactor conditions for a catalyst depend on the process. For example, propylene production from propane requires limited methyl-acetylene production. Another such example is ethylene oxide produced from ethane and oxygen needs to be highly selective, due to the small increase in price between the two compounds. High-throughput

screening is a technique for screening many catalysts (with a constant set of reaction conditions) in a short amount of time[14], but this same attention has not been applied to the reaction conditions, where small changes can change the rate by several orders of magnitude[15].

There is always a function of parameters ("performance function") that can be defined so that its maximum corresponds to the best performance. Experiments in catalysis use packed-bed reactors, which depend on catalyst, feed flowrates, spacetime, temperature, and pressure. One would like to find values for these parameters that give optimal performance. This is not simple because there isn't a generally accepted definition of best performance. For example, naïvely optimizing for yield will result in arbitrarily large reactors for many reactions, including equilibrium limited reactions or reactions with a high reaction order. Nevertheless, we propose here a method that will vary automatically the input in a reactor to generate the optimal output according to a performance function, which is being maximized.

2.4.2. On metrics of reactor performance

There isn't a unique definition of best performance unless one examines the whole chemical process. Even then one can vary parameters for various goals: highest profit, lowest environmental impact, etc. Oftentimes conversion, selectivity, and yield are chosen as the relevant criteria for a set of reaction conditions, but these normalized metrics fail to capture the rate at which products are being produced in an absolute basis and therefore lead optimum reactor sizes which are unrealistically large or small.

Taking a step back at its most basic purpose, a reactor takes in a stream of low-value or unwanted reactants (e.g., feedstocks and pollutants) and converts them to more valuable products (e.g., marketable products or less harmful emissions). Therefore a reactor's primary

performance is measureable by the rate at which it generates value. This approach may be overly simplistic for optimizing a chemical plant or overall process (because it ignores capital costs, utilities, and other intricacies), but it is a good general criterion for catalyst performance, as shown below in Equation 1. Note that the "value" of components flowing into or out of the reactor is highly subjective. For commodity chemicals, there exists a market and price for many compounds, but other effects, such as location, regulation, and goal, will affect these values.

$$Value\ generation = \sum_{i}^{Feeds} F_i\ Value_i - \sum_{i}^{Effluents} F_i\ (Value_i + Sep_i) \quad (1)$$

Above in Equation 1, F_i is the flowrate (in mass or moles) of component i and $Value_i$ is similarly the value of the ith component (per mass or moles), such as the market price, Feeds is the number of reactor feed components and Effluents is the number of reactor effluent components. By optimizing this rate of reactor value generation, the catalyst creates the most value per time possible. For example, suppose one optimizes spacetime to maximize yield or conversion for a simple equilibrium-limited reaction A -> B, a slower spacetime will always produce asymptotically more B (thus raising the conversion or yield). On the contrary our proposed performance metric, the rate of value generation per catalyst, will be maximized at a finite spacetime given non-zero separation costs.

2.4.3. Optimization algorithm

Optimizing the discrete reaction conditions of a real reactor is provides unique challenges compared to the mathematical optimization of oftentimes well-defined, highly differentiable functions. These challenges include lack of derivative information on the

performance metric, experimental measurement error and drift, and different convergence criteria. Many optimization algorithms exist for optimizing numerical functions. Of those, relatively few (1) only evaluate function values (that is to say don't require the Hessian or Jacobian), (2) are robust against noise, and (3) are resilient against slowly drifting values. Methods that only evaluate function values are predominantly comprised of simplex methods, interpolation methods, and pattern search methods. Despite its simplicity, the Hooke-Jeeves pattern search is robust and can quickly reach convergence for a variety of problems.[16]

2.5. Computational Chemistry Methods

Although computational methods can be very accurate (~1 kcal/mol) for small, well-defined systems, heterogeneous catalytic systems are neither small nor well defined. Thus in general, accurately calculating and predicting heterogeneous catalyst properties is not feasible at this time (although there are some promising specific results[17–19]). Computational methods can be fruitful during investigations of heterogeneous catalysts for finding trends and for guiding experiments.

To do useful computations on a catalytic system (with a large number of electrons and nuclei), Density Functional Theory (DFT) is one of the most accurate computational tools which is still tractable to solve for catalyst-sized systems.

2.6. References

1. Wachs, I. E. & Routray, K. Catalysis Science of Bulk Mixed Oxides. *ACS Catal.* **2,** 1235–1246 (2012).

2. Weckhuysen, B. M. & Keller, D. E. Chemistry, spectroscopy and the role of supported vanadium oxides in heterogeneous catalysis. *Catal. Today* **78,** 25–46 (2003).

3. Aruna, S. T. & Mukasyan, A. S. Combustion synthesis and nanomaterials. *Curr. Opin. Solid State Mater. Sci.* **12,** 44–50 (2008).

4. Bera, P. *et al.* Structural Investigation of Combustion Synthesized Cu/CeO 2 Catalysts by EXAFS and Other Physical Techniques: Formation of a Ce 1 - x Cu x O 2- δ Solid Solution. *Chem. Mater.* **14,** 3591–3601 (2002).

5. Hegde, M. S., Madras, G. & Patil, K. C. Noble metal ionic catalysts. *Acc. Chem. Res.* **42,** 704–12 (2009).

6. Deshpande, S., Patil, S., Kuchibhatla, S. V. & Seal, S. Size dependency variation in lattice parameter and valency states in nanocrystalline cerium oxide. *Appl. Phys. Lett.* **87,** 133113 (2005).

7. Toby, B. EXPGUI, a graphical user interface for GSAS. *J. Appl. Crystallogr.* 210–213 (2001). at <http://scripts.iucr.org/cgi-bin/paper?hw0089>

8. Larson, A. C. & Von Dreele, R. B. *General Structure Analysis System (GSAS)*. *Structure* **748,** (2004).

9. Ernst, M. A. & Sloof, W. G. Unraveling the oxidation of Ru using XPS. *Surf. Interface Anal.* **40,** 334–337 (2008).

10. Tao, F. F. & Salmeron, M. In situ studies of chemistry and structure of materials in reactive environments. *Science* **331,** 171–4 (2011).

11. Scott Fogler, H. Elements of chemical reaction engineering. *Chem. Eng. Sci.* **42,** 2493–2493 (1987).

12. Taylor, H. S. Tests for Transport Limitations in Experimental Catalytic Reactors. *Ind. Eng. Chem. Process Des. Dev.* **10,** 541–547 (1971).

13. Mears, D. E. Diagnostic criteria for heat transport limitations in fixed bed reactors. *J. Catal.* **20,** 127–131 (1971).

14. Cong, P. *et al.* High-throughput Synthesis and Screening of Combinatorial Heterogeneous Catalyst Libraries. *Angew. Chemie* **38,** 483–488 (1999).

15. Temel, B., Meskine, H., Reuter, K., Scheffler, M. & Metiu, H. Does phenomenological kinetics provide an adequate description of heterogeneous catalytic reactions? *J. Chem. Phys.* **126,** 204711 (2007).

16. Hooke, R. & Jeeves, T. a. "Direct Search'' Solution of Numerical and Statistical Problems. *J. ACM* **8,** 212–229 (1961).

17. Medford, a. J. *et al.* Assessing the reliability of calculated catalytic ammonia synthesis rates. *Science (80-.).* **345,** 197–200 (2014).

18. Nørskov, J. K., Bligaard, T., Rossmeisl, J. & Christensen, C. H. Towards the computational design of solid catalysts. *Nat. Chem.* **1,** 37–46 (2009).

19. Nørskov, J. K. *et al.* The nature of the active site in heterogeneous metal catalysis. *Chem. Soc. Rev.* **37,** 2163–71 (2008).

3. Catalytic Dry Reforming of Methane on Ruthenium-doped Ceria and Ruthenium supported on Ceria

3.1. Introduction

Steam reforming of methane is the preferred commercial process [1, 2] for the preparation of syngas. There is, however, considerable interest in ‘‘dry reforming’’ [3–6], which uses CO_2 rather than steam, because large quantities of methane are found mixed with carbon dioxide. The expense of separating methane from CO_2, prior to syngas preparation, makes steam reforming of methane from such sources uneconomical. An efficient dry reforming catalyst would allow us to make use of low-cost CO_2 -containing methane to produce syngas. Here we study dry reforming by two catalysts: one which is assumed to be Ru-doped ceria and another which is assumed to be metallic Ru supported on ceria.

Rostrup-Nielsen and Bak Hansen [7] investigated dry reforming catalyzed by silica-supported nickel, ruthenium, rhodium, palladium, iridium, and platinum catalysts and found that the ruthenium performed best, with the highest turnover and minimal coke formation. Safariamin et al. [8] studied ruthenium supported on alumina and ceria and combinations thereof. They found that the performance of Ru supported on alumina impregnated with ceria is better than that of Ru supported on alumina. Other studies have found that oxidic ruthenium compounds are also active catalysts. For example, Nakagawa et al. [9] suggested that the coexistence of metallic ruthenium and ruthenium oxide was important for dry reforming activity. These results indicate a dual-site mechanism could likely be important. In a similar catalytic system, Gallego and co-workers [10] found Ni/La_2O_3 and the perovskite, $LaNiO_3$, catalyzed dry reforming via a dual-site mechanism.

We studied Ru-doped ceria for two reasons. (1) Our temperature programmed reaction studies of dry reforming and of partial oxidation of methane, catalyzed by Ru-doped ceria, found that dry reforming (producing predominantly synthesis gas) starts at a lower temperature than partial oxidation (producing predominantly carbon dioxide and water). If interpreted naively this would indicate that CO_2 is a better oxidant than O_2, which is not an acceptable conclusion. We show here that the dry reforming catalyst is the reduced oxide and this reduction is possible because CO_2 is a poorer oxidant than O_2. (2) The combustion method used here is one of the most reliable ways of preparing doped oxides [11]. However, no matter what the preparation method is, one is never completely sure that a doped oxide was prepared. Because of this uncertainty, we also prepared a Ru ceria catalyst by impregnation and reduction, with the intent of preparing metallic supported on ceria. We hoped to show that this catalyst is different from the presumed doped-oxide catalyst. To our surprise we found that the two catalysts have identical catalytic activity even though their physical properties are different.

3.2. Experimental

3.2.1. Catalyst Synthesis

Ruthenium-doped ceria was synthesized using the combustion method previously used by Hegde et al.[11]. To begin, 2.50 g of cerium(III) nitrate hexahydrate, 0.06 g of ruthenium(III) chloride, and 0.09 g of urea are dissolved in water (Millipore). A Pyrex dish with this mixture is placed into a furnace, which is heated to 450^{o}C to induce spontaneous combustion and produce an oxide. The combustion is very rapid and it is assumed that in this short time the Ru atoms are not able to migrate and make a separate phase, and they get trapped where they were when the combustion started. This is one of the most reliable

methods for producing a substitutionally doped oxide (i.e. single Ru atoms replace Ce atoms). In what follows we use for this material the notation $Ru_{0.05}Ce_{0.95}O_2$.

Ruthenium metal supported on ceria was synthesized by wet-impregnation. Cerium oxide powder, prepared by combustion synthesis (as described above, but without $RuCl_3$), was dried in air at 220°C after which it was added to an aqueous solution of $RuCl_3$. The Ru concentration was such that the ruthenium:cerium mole ratio was 5 %, as in the sample prepared by combustion. The mixture was sonicated and dried in air at 80°C and then heated in H_2 at 400°C for 6 h to reduce $RuCl_3$. We used a relatively low calcination temperature to minimize Ru diffusion into CeO_2. Temperature programmed reduction experiments [12–17] have shown that ceria is reduced by H_2. The temperature at which hydrogen consumption by ceria begins depends on the grain size [17] and also on surface contaminants (some ceria surfaces have hydroxyls or polydentate carbonates [12]) or bulk contaminants (e.g. La is present in ceria used in Ref. [13]). Because of this, different experiments, on different ceria samples, find different temperatures at which ceria starts being reduced by hydrogen (e.g. 200°C[12], 347°C[13], 327°C[14]); these values are below the temperature we used to reduce $RuCl_3$. Therefore we expect that the as-prepared catalyst is metallic Ru on a partially reduced ceria support. However, the material was in contact with air for a long time before being used as a catalyst (the shortest time was 1 day, the longest 2 weeks). We assume that this exposure to air reoxidized ceria. Perrichon et al. [13] found that ceria reduced with H_2 reoxidizes rapidly at room temperature, if it is not reduced too far. In what follows we denote the material prepared by the second procedure by Ru/CeO_2 and will call it metallic Ru supported on ceria.

We emphasize that there is no guarantee that the combustion method produces doped ceria or that all Ru in the sample prepared by impregnation is metallic.

3.2.2. Catalyst Characterization

X-ray diffraction (XRD) data were collected on a Philips X'PERT diffractometer. Synchrotron XRD patterns were collected in transmission mode at RT on beamline 11-BM at the Advanced Photon Source, Argonne National Laboratory, with a photon energy of approximately 30 keV. Rietveld refinements were performed using GSAS [18, 19].

X-Ray photoelectron spectroscopy (XPS) spectra were obtained with Al K_a radiation using a Kratos Axis Ultra X-ray photoelectron spectrometer. In order to account for charging, the XPS spectra were shifted using the C(1s) peak of adventitious carbon to 285.0 eV.

Diffuse reflectance infrared fourier-transform spectroscopy (DRIFTS) of adsorbed CO was performed using a Thermo Electron Corporation Nicolet 4700 with DRIFTS accessories by Harrick Scientific. Samples catalyzed dry reforming at 400 ^{o}C for an hour, and then cooled to 25 ^{o}C in argon. After that, 10 % CO in argon was flowed over the sample for 10 min. Subsequently, pure argon was flowed to remove CO from the gas phase while adsorbed CO remained bound to the surface. Spectra were collected at each of these steps.

3.2.3. Reactivity Characterization

The activity of the catalysts was determined in a packed bed reactor with a high flowrate to achieve a very short residence time (differential reactor). The reactor (a quartz tube with 4 mm inner diameter sealed with quartz wool) was filled with 25 mg of catalyst mixed with 50 mg of 200-mesh GC-grade alumina. Gases were delivered using mass-flow controllers

(MFCs, supplied by MKS). The CH_4:CO_2:Ar ratios were 1:1:3. The catalyst void-fraction was measured volumetrically with methanol and the gas flowrate was set such that the spacetime was 0.18 s (calculated at 20^{o}C), unless otherwise noted. This spacetime corresponds to 110 mol of CH_4/(g-catalyst * s). The reactor effluent was measured by a differentially pumped mass spectrometer (SRS). Frequent calibrations of the mass spectrometer, with mixtures of reactants, products, and argon with known composition, were made. All gases had a purity of at least 99.99 %. The temperature was controlled and varied by using a programmable controller (OMEGA CSC32).

Temperature programmed reaction (TPR) was used to determine the activity of the catalyst as a function of temperature. With a constant volumetric feed rate, the reactor temperature is varied linearly while the composition of the effluent is monitored. Due to the temperature increase, the space time decreases from 0.18 s at room temperature to 0.06 s at 600^{o}C. In TPR experiments, the system might not reach steady state during the temperature ramp. Because of this, we also performed staircase temperature programmed reaction (STPR) experiments to study the activity of the catalyst at steady state. In STPR, the temperature is increased from 250 to 600 ^{o}C in 50 ^{o}C increments. After each increase the temperature is held constant for 30 min to allow the reaction to reach steady state. After reaching 600 ^{o}C the temperature is decreased with a reversed stepwise evolution until the temperature is 250^{o}C.

Transient oxidation reaction spectroscopy (TORS) was used to investigate the dependence of catalyst oxidation state on catalytic activity. In these experiments, the dry reforming reaction is run at steady state, at fixed temperature, and 2-s-wide pulses of O_2 are injected into the reactor feed to observe the effect on reaction products. The pulse shape was

approximately square. The height of the pulse was set such that the oxygen and methane concentrations were equal for the duration of the pulse. This is the ratio used in the partial oxidation experiments.

3.3. Results and Discussion

3.3.1. Catalyst Characterization

The XRD data obtained in our laboratory are shown in Fig. S1, for Ru/CeO_2 (the figures labeled by S followed by a number are supplemental and to be found a the end of the chapter). One observes the diffraction peaks due to CeO_2 and small peaks corresponding to the *hcp*-phase of metallic Ru. The Rietveld-refined, synchrotron XRD data obtained from both as-prepared and post-reaction ruthenium-doped ceria are shown in Fig. 1. The refinement included data for wavenumbers between 0.8 and 11.6 $Å^{-1}$. No diffraction peaks corresponding to RuO_2 or metallic Ru are present in the spectra of $Ru_{0.05}Ce_{0.95}O_2$. The lattice constant for as- prepared Ru-doped CeO_2 is 5.4214 Å; it is 5.4022 Å after the catalyst was used. Scherer broadening analysis of the ruthenium metal on ceria catalyst indicated that ruthenium crystallites were 19 nm in size (accounting for instrumental broadening). Crystallites in this size range are typical for ruthenium wet-impregnated catalysts.

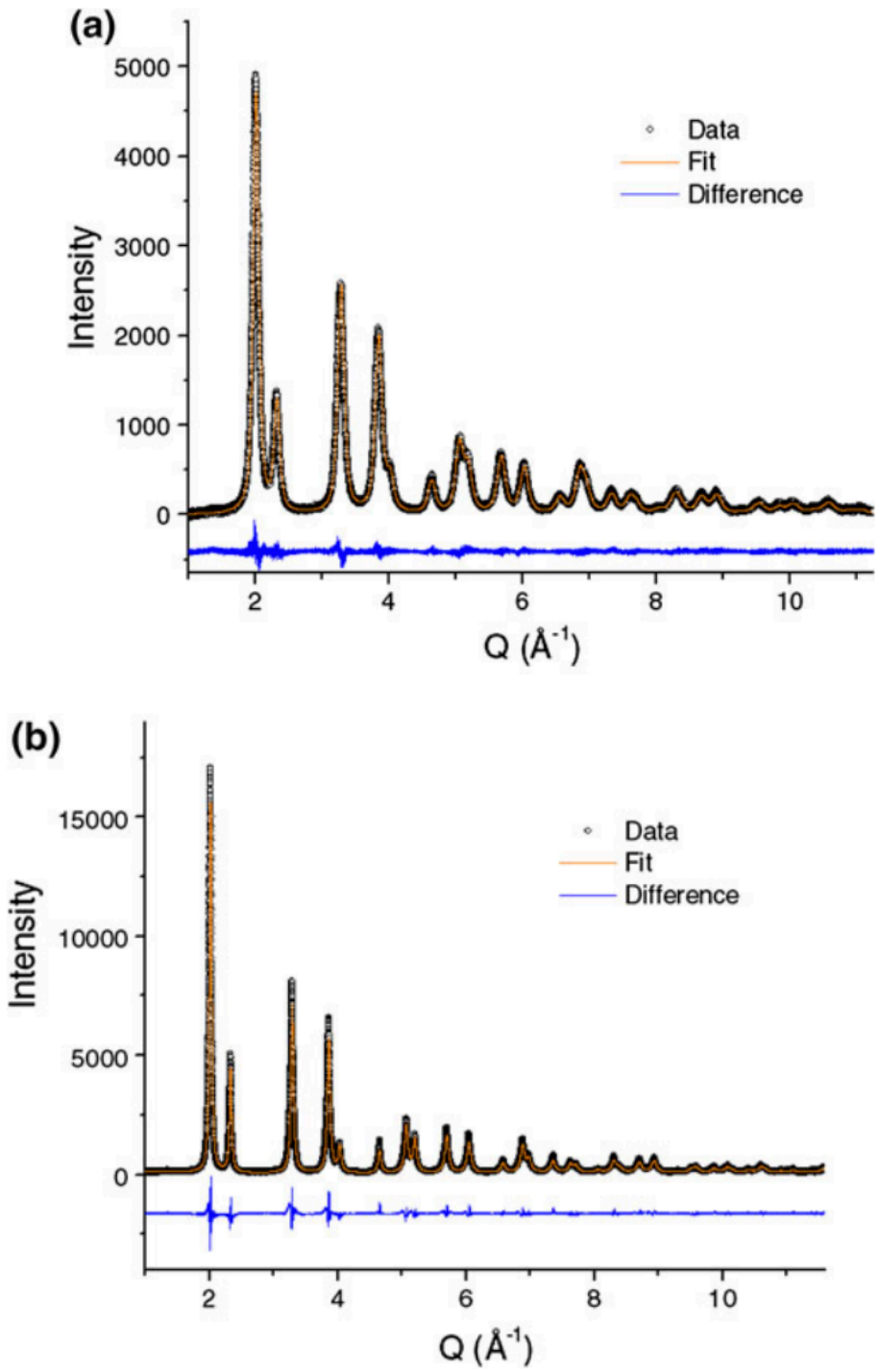

Figure 1. Synchrotron XRD patterns of ruthenium-doped ceria (a) as synthesized and (b) after catalyzing dry reforming at 500^{o}C for 5 h. Both samples are single-phase fluorite, exhibiting no *hcp*-Ru or RuO_2.

Table 1 gives the binding energies of the 3p3/2 orbital in the XPS spectrum of ruthenium atom, published by Ernst and Sloof [20], for Ru metal and RuO_2. Also included are the binding energies measured by us for $Ru_{0.05}Ce_{0.95}O_2$ and Ru/CeO_2, for the as-prepared catalysts, and for the catalysts after the reaction. According to the XPS results the Ru atoms in the two catalysts differ from each other: the Ru in $Ru_{0.05}Ce_{0.95}O_2$ is more oxidized than in Ru/CeO_2 or in RuO_2. It is difficult to understand why the binding energy in Ru/CeO_2 is closer to that of RuO_2 than Ru metal, even though the XRD measurements detect Ru metallic in Ru/CeO_2. This may be due to a size effect (Ru clusters are small) or to the oxidation of the Ru clusters by atmospheric oxygen prior to taking the XPS spectra. Finally, no chlorine was observed on the catalyst after reaction, indicating chlorine (from the ruthenium precursor) does not likely play a role in activity.

Table 1. XPS results for electron binding energy (BE) for Ru. Values in the first two rows are from Ref. 19.

compound	**BE $Ru3p_{3/2}$ eV**
Ru metal (lit.)	461.5
RuO_2 (lit.)	462.7
RuO_2 (this work)	462.6
$Ru_{0.05}Ce_{0.95}O_2$	
as prepared	464.1
after the dry reforming reaction	464.4
Ru/CeO_2	
as prepared	462.3
after the dry reforming reaction	462.0

To further test whether $Ru_{0.05}Ce_{0.95}O_2$ and Ru/CeO_2 are different materials we used CO as a surface probe, performed in situ after reaction (without exposure to air). We expect

from literature [21] that the CO vibrational energy is different when CO adsorbs on metallic Ru than when it adsorbs on Ru-doped ceria (where Ru is ionic). The DRIFTS spectra (Fig. 2) of CO adsorbed on $Ru_{0.05}Ce_{0.95}O_2$ and on Ru/CeO_2 show that the two materials interact differently with CO. The CO adsorbed on $Ru_{0.05}Ce_{0.95}O_2$ has an infrared (IR) absorption peak (marked by A1 in Fig. 2) that is absent for CO adsorbed on Ru/CeO_2. The frequency of this peak is very close to that of the gas-phase CO but it is not due to photon absorption by gaseous CO. To prove this we have also taken the IR absorption spectrum of the $Ru_{0.05}Ce_{0.95}O_2$ catalyst after exposure to CO but prior to purging with Ar. This spectrum (dotted lines in Fig. 2) has the M-shape typical of the R- and P-branches of gaseous CO. Clearly the A1 peak is not due to the gas. We also found that the peak A1 disappears when the sample is heated from 20 to 100 ^{o}C. This weakly bound CO vibrates roughly at the same frequency as gas-phase CO but it does not have the R- and P- branches because it is not free to rotate. The three peaks observed for the CO adsorbed on $Ru_{0.05}Ce_{0.95}O_2$ (namely A1, A2, and A3) suggest that on this surface CO has three distinct binding sites. In contrast, there is almost no CO adsorption (except perhaps for the two small peaks denoted B1 and B2 in Fig. 2) on Ru/CeO_2, which is surprising. We assume that this happens because the Ru clusters in Ru/CeO_2 are oxidized on the surface.

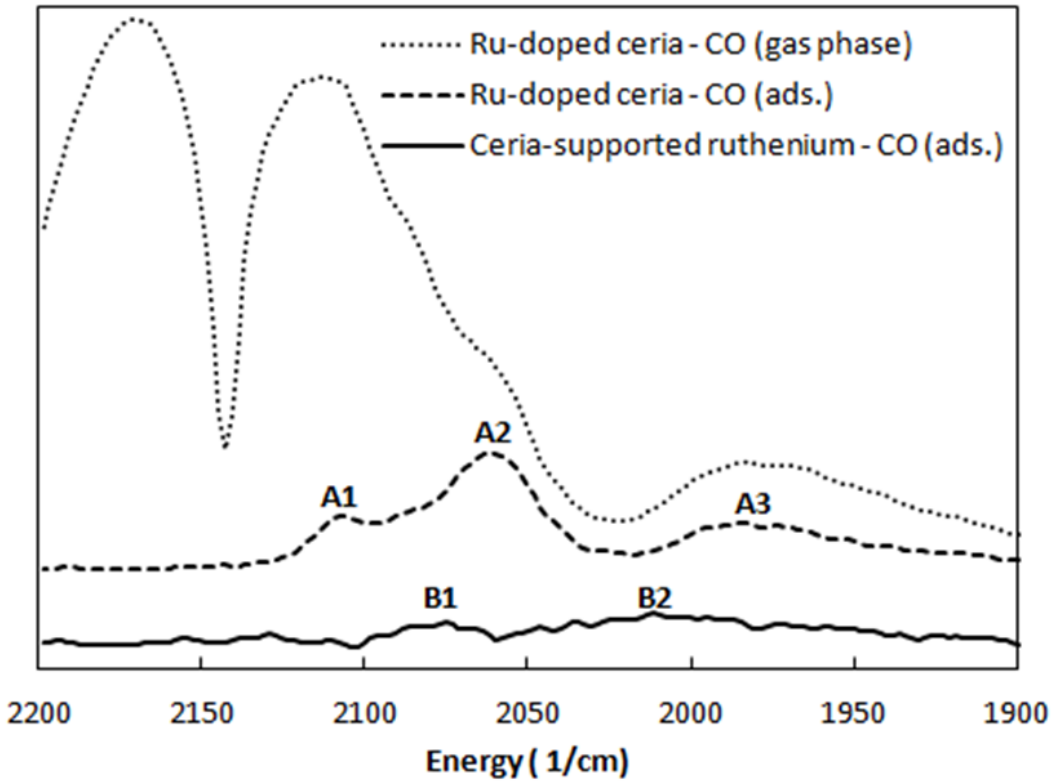

Figure 2. DRIFTS spectra of ruthenium-doped ceria (dashed line) and ruthenium supported on ceria (solid line), after exposure to CO followed by purging with Ar to remove gaseous CO from reactor. The catalyst was exposed to CO after it was used for dry reforming (see text). The dotted line shows the IR spectrum of Ru-doped ceria after exposure to CO and prior to purging with Ar.

Chin et al. [21] assigned the CO IR-absorption peaks to different CO–Ru binding moieties for various Ru oxidation states. While we do not dispute the assignment we prefer not to make use of it here.

In summary: XPS, XRD, and the IR spectrum of CO adsorbed on these catalysts indicate that $Ru_{0.05}Ce_{0.95}O_2$ and Ru/CeO_2 are different materials, as prepared and after they catalyzed

the dry reforming reaction. Nevertheless, they have practically identical catalytic activity, as we show below.

3.3.2. Catalyst Reactivity

Figure 3 shows methane conversion in two temperature programmed reaction (TPR) experiments: partial oxidation and dry reforming of methane. These results are surprising for two reasons. First, the oxidation of methane by dry reforming starts at lower temperature than partial oxidation with O_2, as if CO_2 is a better oxidant than O_2. Second, dry reforming and methane oxidation with O_2 are supposed to have the same rate-limiting step: the breaking of the C–H bond. If this is true, one would expect, perhaps naively, that the two reactions should take off at the same temperature.

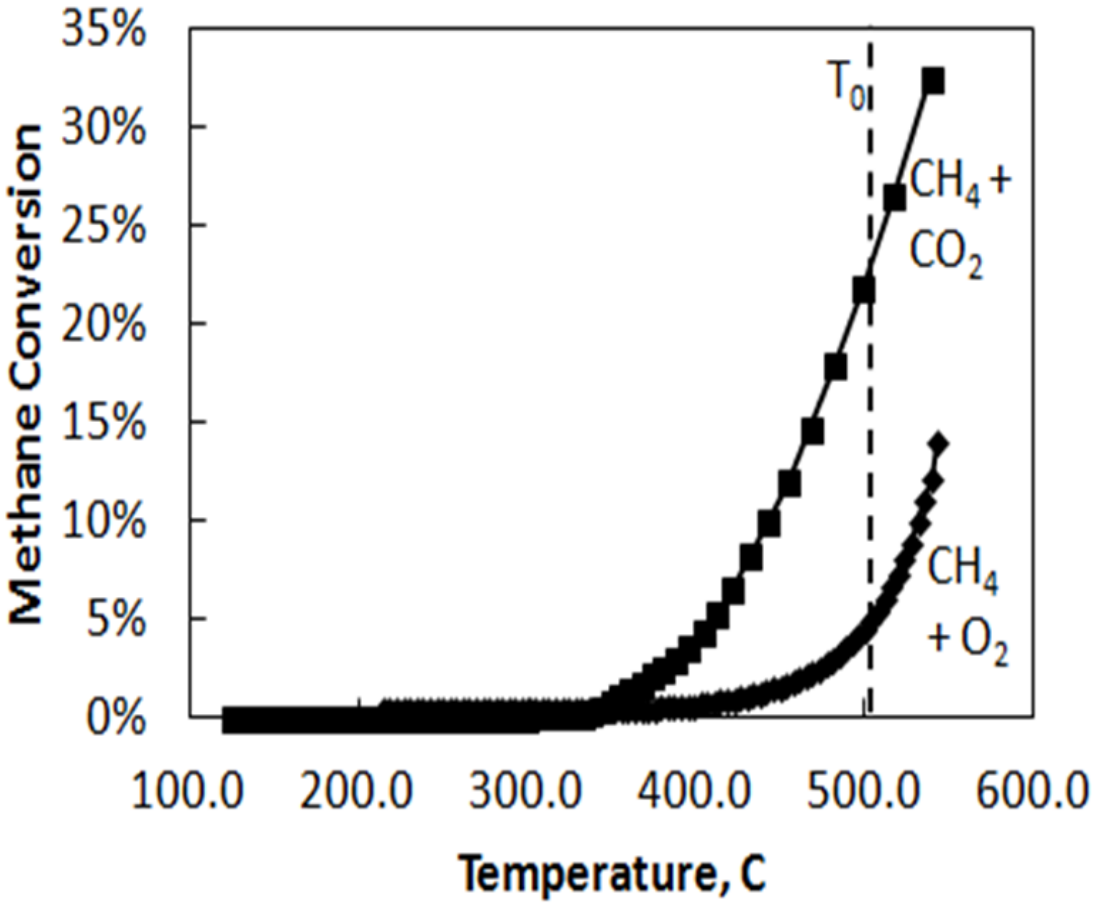

Figure 3. Methane partial oxidation using oxygen or carbon dioxide on a ruthenium-doped CeO_2 catalyst. The catalyst bed contained 25 mg of $Ru_{0.05}Ce_{0.95}O_2$, diluted with 50 mg of alumina. The temperature ramp was 10 °C/min. Feed composition was 1:1:3 (molar) for CH_4:CO_2:Ar (for dry reforming) and 2:1:3 for CH_4:O_2:Ar (for partial oxidation). Spacetime was 0.18 second at 20 °C. Dry reforming produced predominately synthesis gas and the methane partial oxidation produced predominately carbon dioxide and water.

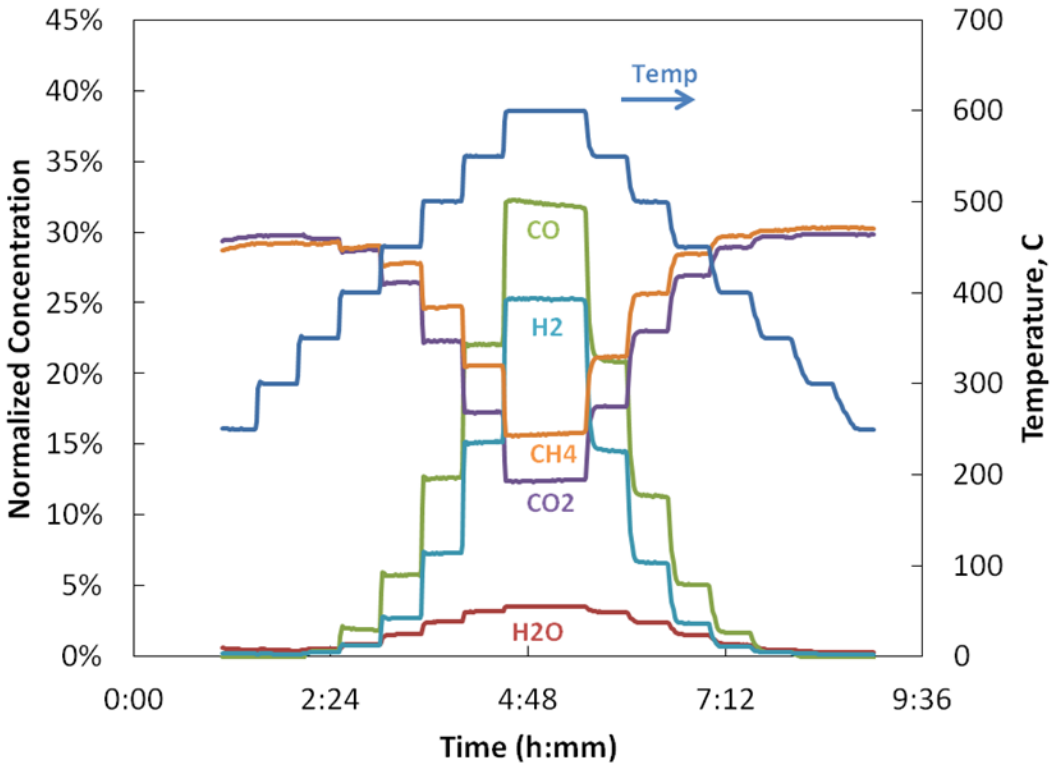

Figure 4a. The steady state composition of the reactor effluent for methane reacting with carbon dioxide on $Ru_{0.05}Ce_{0.95}O_2$, at various temperatures. The plug reactor contained 25 mg of $Ru_{0.05}Ce_{0.95}O_2$ diluted with 50 mg of alumina. Temperature was varied from 250 °C to 600 °C and back to 250 °C in steps of 50 °C. After each step the temperature was held constant for 30 minutes. Mass balances were approximately 100%. The feed molar

composition was 1:1:3 for CH_4:CO_2:Ar. Total volumetric flowrate corresponded to a spacetime of 0.18 seconds at 20 °C.

A possible resolution of these two puzzles is that $Ru_{0.05}Ce_{0.95}O_2$ evolves into two distinct catalysts when exposed to two different feeds (CH_4:O_2 or CH_4:CO_2). We show in Sect. 3.3 that this is the case.

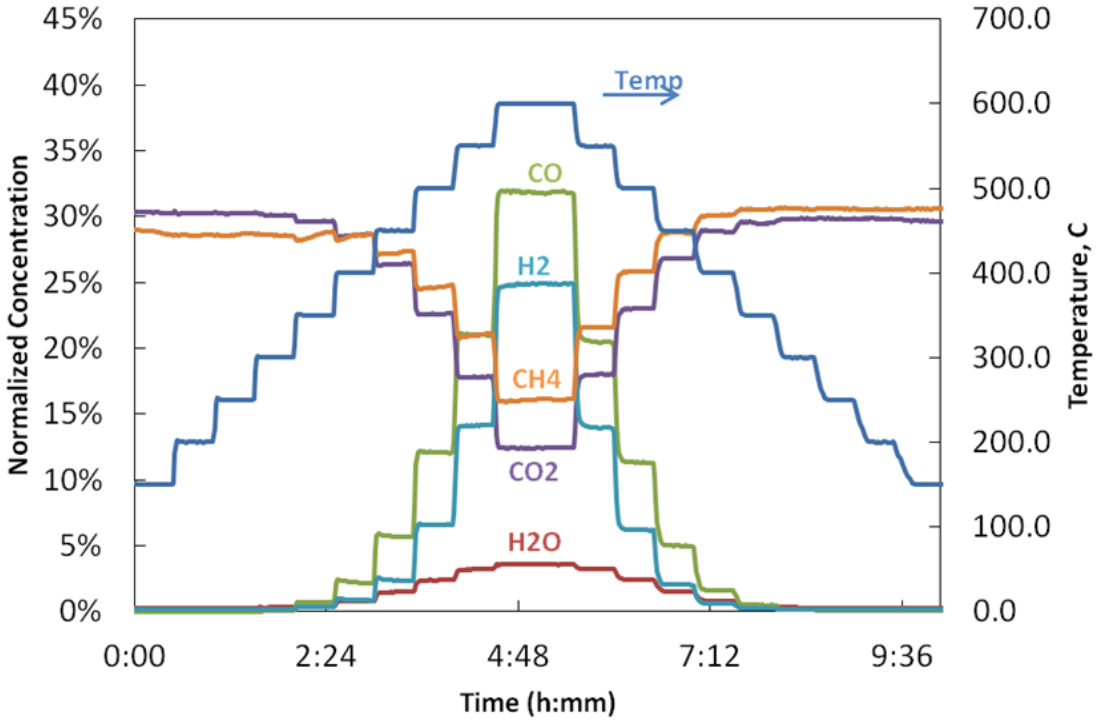

Figure 4b. The steady state composition of the reactor effluent for methane reacting with carbon dioxide on Ru/CeO_2, at various temperatures. The plug reactor contained 25 mg of $Ru_{0.05}Ce_{0.95}O_2$ diluted with 50 mg of alumina. Temperature was varied from 250 °C to 600 °C and back to 250 °C in steps of 50 °C. After each step the temperature was held constant for 30 minutes. Mass balances were approximately 100%. The feed molar

composition was 1:1:3 for CH_4:CO_2:Ar. Total volumetric flowrate corresponded to a spacetime of 0.18 seconds at 20 °C.

Figure 4a, b show the STPR data for dry reforming using $Ru_{0.05}Ce_{0.95}O_2$ and Ru/CeO_2, respectively. The mass balance for carbon, hydrogen, or oxygen is 100 ± 2%. The dark-blue curve in Fig. 4a shows how the temperature of the reactor was changed with time (the temperatures scale is on the right hand side of the graph). The measurements start at 250^{o}C and the temperature is held constant at that temperature for 30 min. As the purple and the yellow–orange curves show, the concentration of CO_2 and CH_4 in the effluent is the same as in the mixture entering the reactor. A small consumption of CH_4 and CO_2 is observed at 400^{o}C. The conversion of both CO_2 and CH_4 are largest at 600^{o}C. If dry reforming were the only reaction in the system then the conversion of CO_2 and CH_4 should be equal, and the amount of H_2 should equal the amount of CO. This is not what we observe: more CO_2 is consumed than methane and more CO is present than H_2. This indicates that the water–gas shift reaction $CO_2 + H_2 \rightarrow CO + H_2O$ also takes place in the system.

It is interesting that the data in Fig. 4b, which shows the STPR results for dry reforming on the Ru/CeO_2 catalyst, is practically identical to the data in Fig. 4a, for the same reaction catalyzed by $Ru_{0.05}Ce_{0.95}O_2$. For example at 600 ^{o}C, methane conversion respectively is 48 and 46 % for $Ru_{0.05}Ce_{0.95}O_2$ and Ru/CeO_2. We have two materials that have identical catalytic activity but give different XRD, XPS, and CO-DRIFTS signals. We are therefore tempted to conclude that the two catalysts contain identical catalytic sites and that the features that make the spectra different are unrelated to catalysis.

3.3.3. Why Does Methane React with CO_2 at Lower Temperature than with Oxygen?

As we have already mentioned we were puzzled by the results shown in Fig. 3 which show the onset of methane conversion, for dry reforming and for partial oxidation, both carried out on $Ru_{0.05}Ce_{0.95}O_2$. The reaction of CH_4 with CO_2 takes place at a temperature at which CH_4 does not react with O_2. This appears to run counter to two strongly held beliefs. One is that the rate-limiting step is the breaking of the C–H bond by the catalyst, which suggests that CH_4 should react at the same temperature regardless of whether O_2 or CO_2 is present. The other is that methane should react at lower temperature with O_2 than with CO_2, because O_2 is a much stronger oxidant. There is however a third possibility. If we assume a Mars-van Krevelen mechanism, then CH_4 reduces the oxide surface and the reduced surface is reoxidized by O_2 (for partial oxidation) or CO_2 (for dry reforming). Since O_2 is a better oxidant than CO_2, the surface is more reduced when the feed contains CO_2 than when it contains O_2 . The results presented in Fig. 3 can therefore be understood if we assume that the more-reduced oxide, present when the feed contains CO_2, is a better methane activation catalyst than the oxidized surface that is present when the feed contains O_2 . This hypothesis can be tested by pulsing O_2 through the reactor while we are running the dry reforming reaction at steady state. If the hypothesis is true then the injection of oxygen should lower methane conversion. The results of these experiments (Fig. 5) show that this is what happens.

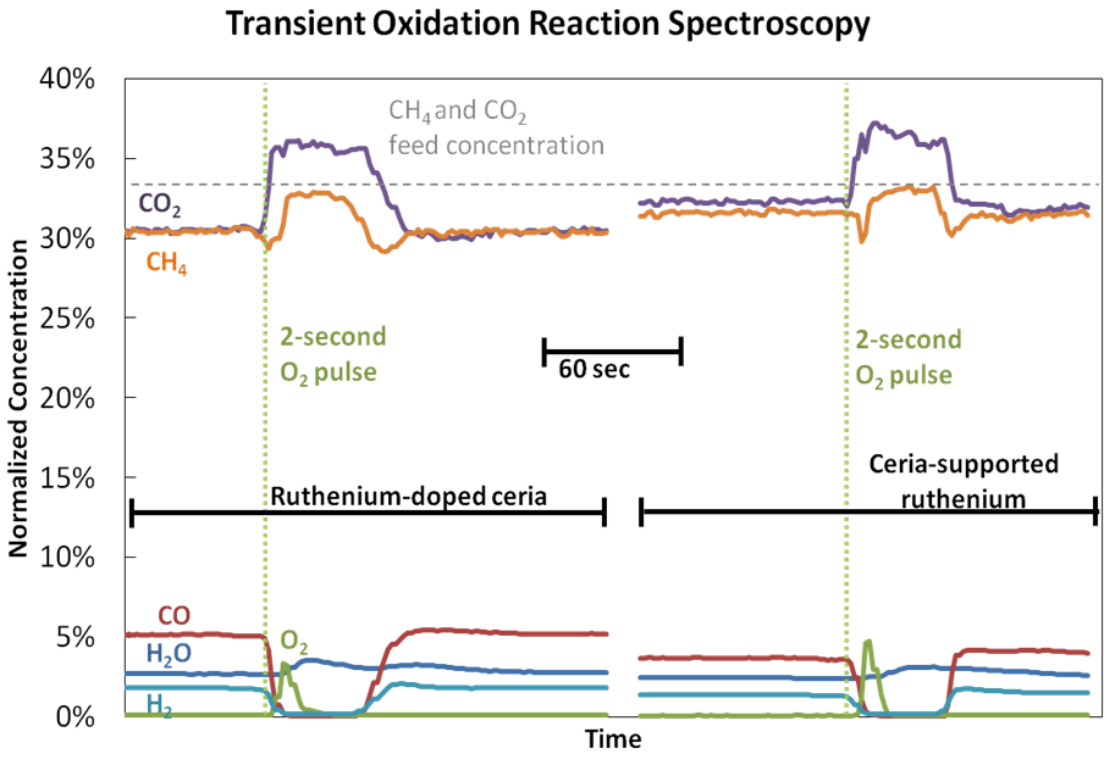

Figure 5. Transient oxidation reaction spectroscopy of methane dry reforming on ruthenium-doped ceria and ceria-supported ruthenium metal. Temperature was maintained at 500 °C. Feed molar composition was 1:1:3 for CH_4:CO_2:Ar. Spacetime was set to 0.07 second, calculated at the reactor temperature of 500 °C. The square O_2 pulse had a width of 2 seconds. The oxygen flowrate equaled that of the methane (overall composition of 1:1:1:3 of O_2:CH_4:CO_2:Ar). Further details are given in the text.

We flowed through the reactor CH_4:CO_2:Ar = 1:1:3 at 500 °C with a flowrate of 0.07 s, until the system reached steady state. The catalyst was either $Ru_{0.05}Ce_{0.95}O_2$ (first panel) or Ru/CeO_2 (second panel). We chose the flowrate so that the reactor is differential, to minimize the complications caused by changes in the catalyst and gas composition along the reactor, which are significant at low flowrates.

The vertical, green, dotted line indicates the moment when the oxygen pulse was sent through the reactor. Prior to that moment the reactor was running the dry reforming reaction at steady state. The dashed horizontal line indicates the concentration of methane and CO_2 at the entrance of the reactor. The yellow and purple lines indicate the concentration of CH_4 and CO_2, respectively, in the effluent. These two lines are below the dashed line because CH_4 and CO_2 were consumed during the passage through the reactor. In the lower part of the graph we show the amount of CO (reddish-brown), H_2O (dark blue), H_2 (cyan), and O_2 (green) in the effluent. The oxygen pulse prior to its entrance in the reactor is not plotted because it is too narrow (2 s) to show on the time scale of the plot. The oxygen pulse seen in the lower part of the graph is oxygen that survived passage through the reactor. The pulse is broadened because of different arrival times at the exit.

The injection of oxygen suppresses the dry reforming reaction: the amount of

methane coming out of the reactor is nearly equal to the amount supplied at the entrance (i.e. the orange line is close to the dashed horizontal line) and is higher than the amount exiting the reactor when no oxygen is introduced. Also, CO and H2 production is suppressed immediately after O_2 is injected. It takes approximately 30 s for the reactor to reach the steady state it had before the oxygen was introduced. We do not understand why the response of the methane has slight dips, immediately after oxygen introduction and right before the steady state is reached. The slow restoration of the steady state indicates the slowness of the rate of catalyst reduction by methane.

The right-hand panel shows the results of the same experiments on Ru/CeO_2 catalyst. The slight differences between the results on the two catalysts are within the error of our

measurements. We conclude that transient response of the two catalysts following oxygen injection is essentially the same.

3.4. Conclusions

We performed experiments meant to answer two questions. Why does CH_4 react with CO_2 at a lower temperature than with O_2, on a catalyst prepared by the combustion method, which is assumed to produce Ru-doped ceria? And if this behavior is typical of Ru-doped ceria, does one observe different chemistry on a catalyst prepared by impregnation (which is assumed to be metallic Ru supported on ceria)?

We find that the two catalysts, prepared by different methods, have different physical properties (XRD, Ru- XPS, and the IR spectrum of CO adsorbed on them) but have essentially the same catalytic chemistry and catalytic activity. Obviously catalytic chemistry on these materials does not take place on surface sites that affect the physical measurements we made. We do not have a reliable explanation for this. It is possible that when the Ru/CeO_2 catalyst was prepared, some Ru atoms ended up as substitutional dopants and they are the active sites. We tried to avoid this from happening, by using a low reduction temperature, but we cannot rule out this possibility. Another possible explanation is that the reaction on Ru/CeO_2 takes place at the border of the metallic Ru with the CeO_2 surface and that the reactivity of the oxygen atoms at this border is similar to that of the oxygen atoms surrounding the Ru dopants. A similar dual-site model could explain some of the observed behavior. In such a model, the cerium oxide site could be rate-limiting and the ruthenium site differs between the catalysts. Hence in such a model, the catalysts show stark differences in characterization (due to different ruthenium [oxide] sites), but the cerium oxide site dominates the control of reactivity. The transient oxygen reaction spectroscopy

shows that reduction is crucial to the activity. Whatever the active site may be—whether it is on ruthenium, cerium, or both—it is strongly activated by incomplete reduction.

The transient reaction experiments using oxygen pulses suggest strongly that methane is more readily activated by the partially reduced catalyst (for both catalyst preparations). In these two reactions ($CH_4 + CO_2$ and $CH_4 + O_2$), methane reduces the oxide surface while CO_2 or O_2 reoxidizes it. Because O_2 is a more effective oxidant than CO_2 , the surface exposed to CO_2 + CH_4 has more oxygen vacancies (is more reduced) than the surface exposed to O_2 + CH_4. While we start with the same catalyst (e.g. Ru- doped ceria), by the time the steady state is reached the catalyst performing dry reforming has evolved to a different, more active state than the catalyst performing partial oxidation: one is more reduced than the other.

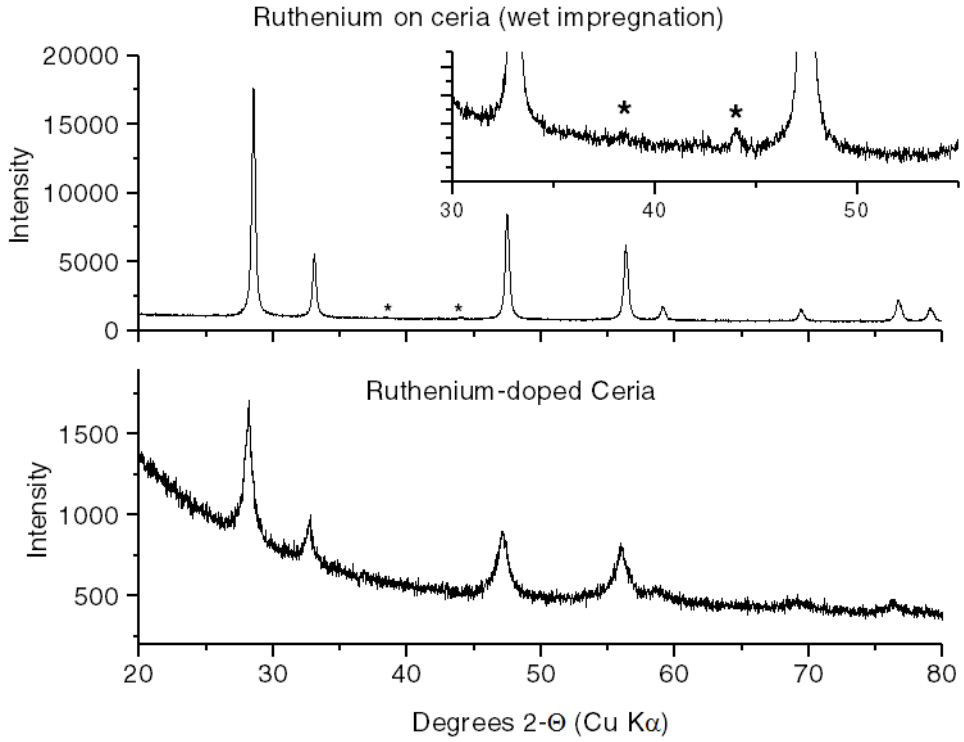

Figure S1. Lab XRD patterns of ruthenium-ceria catalysts as synthesized. Prominent peaks correspond to cubic-phase CeO_2 and asterisks denote *hcp*-phase metallic ruthenium.

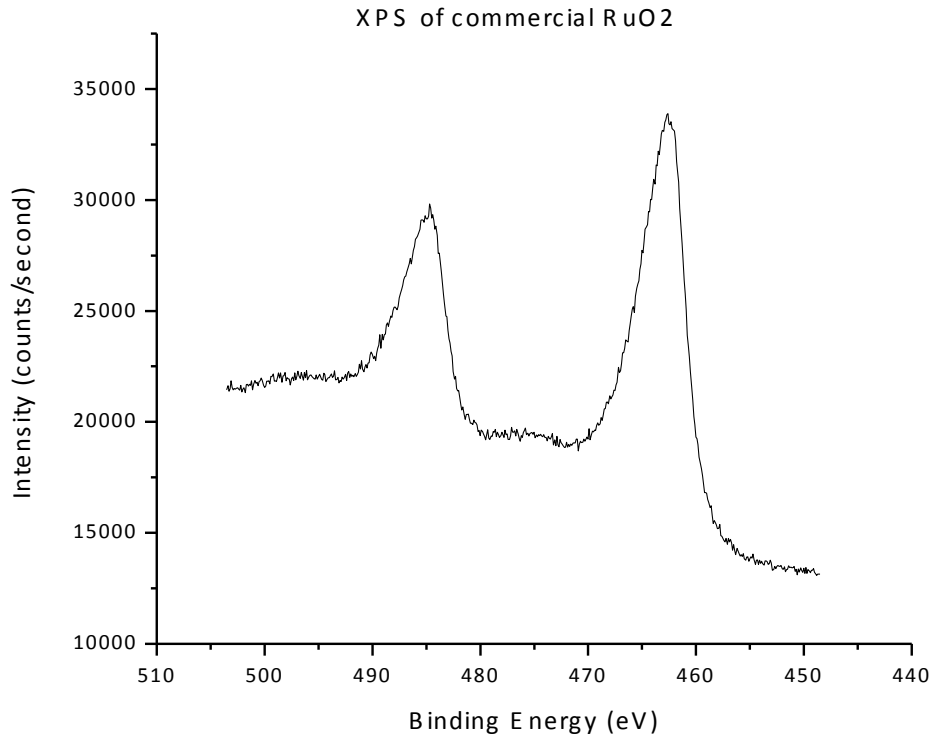

Figure S2. XPS binding energies from Ru $3p_{3/2}$ emission. Commercial RuO_2 (Sigma Aldrich) was analyzed. Ru $3p_{3/2}$ has a BE of 462.6eV, agreeable with the BE of 462.7, as reported by Ernst.

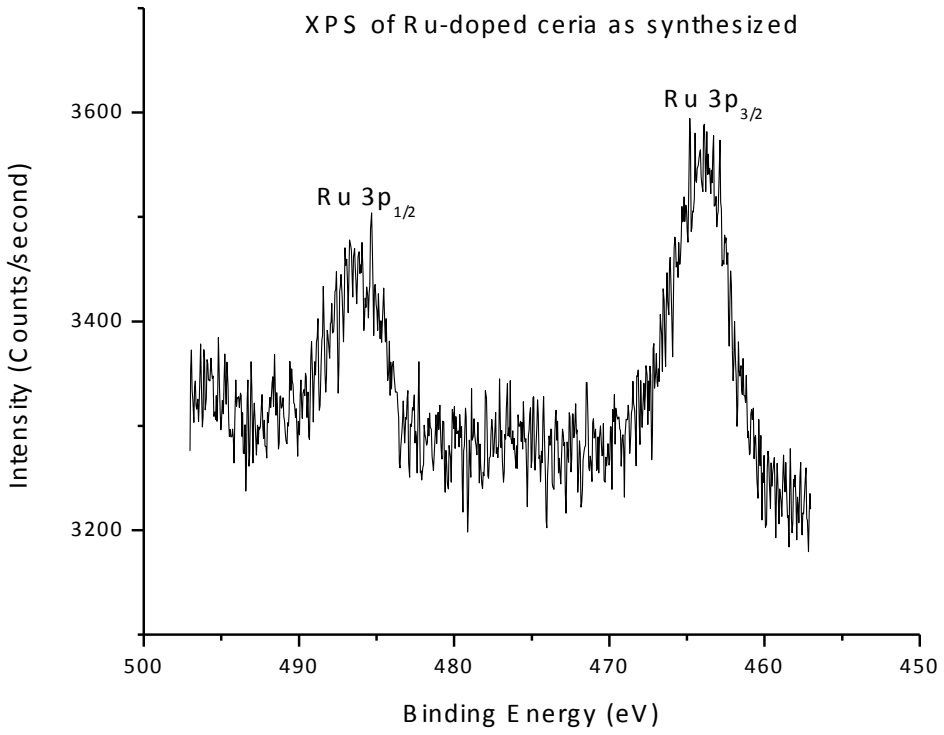

Figure S3. XPS binding energy from Ru $3p_{3/2}$ emission. XPS of as-synthesized Ru-doped CeO_2 shows a Ru $3p_{3/2}$ BE of 464.1eV.

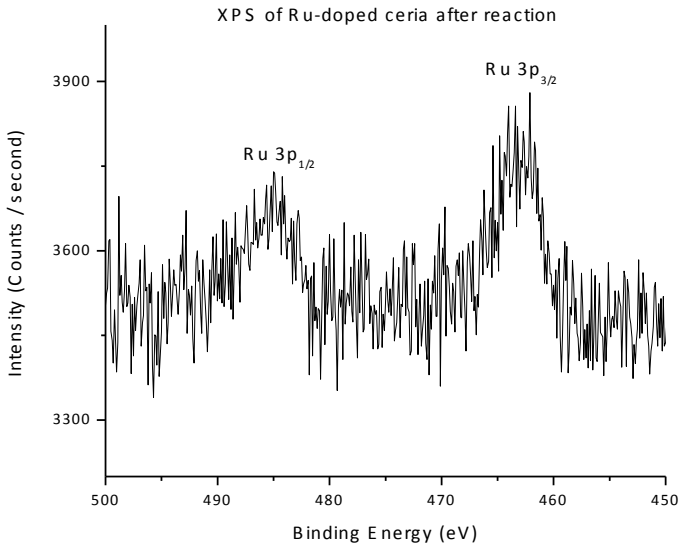

Figure S4. XPS binding energy from Ru $3p_{3/2}$ emission. XPS Dry reforming was catalyzed by Ru-doped ceria at 500°C for 3 hours (so steady-state was reached). Feed molar composition was 1:1:3 for CH_4:CO_2:Ar. Space time was set to 0.07 seconds flowrate (calculated at the reactor temperature of 500°C). The catalyst was cooled in argon and analyzed immediately. The BE of Ru $3p_{3/2}$ is 464.4eV.

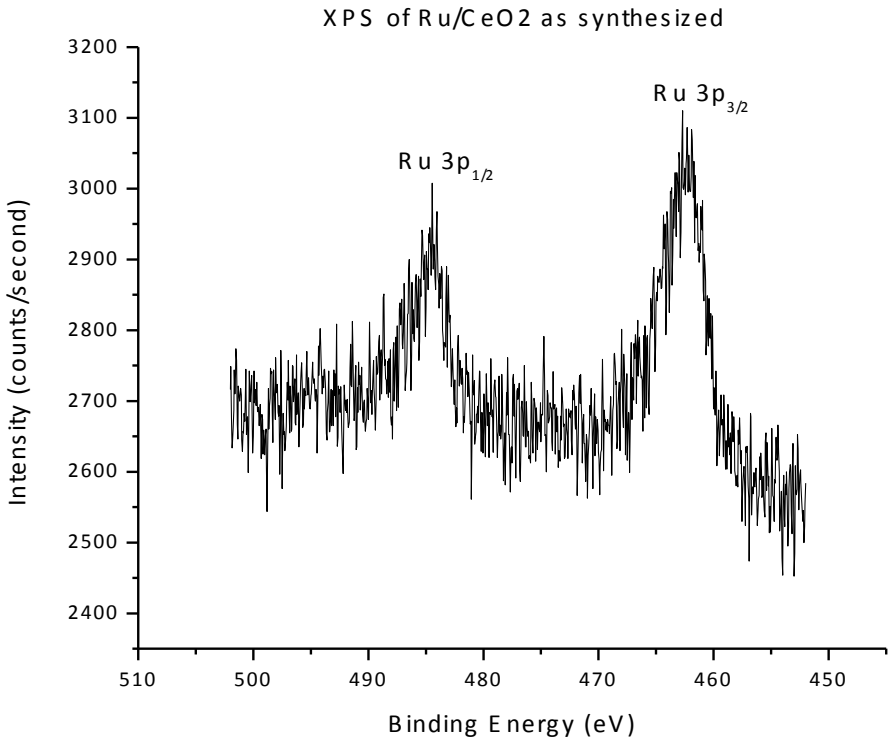

Figure S5.XPS binding energy from Ru $3p_{3/2}$ emission. XPS of Ru/CeO_2 as synthesized shows a Ru $3p_{3/2}$ BE of 462.3eV

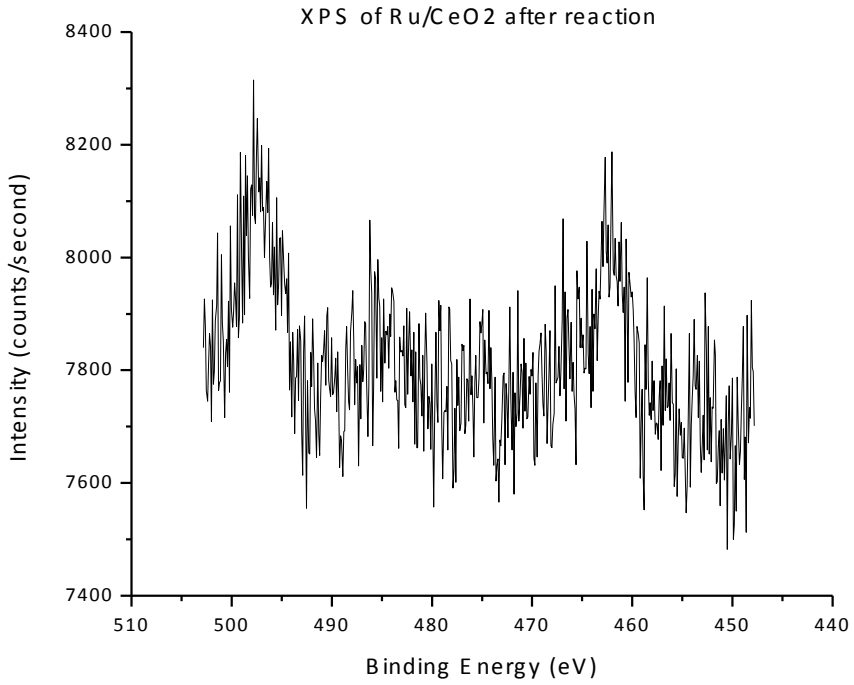

Figure S6. XPS binding energy from Ru $3p_{3/2}$ emission. Dry reforming was catalyzed by Ru/CeO_2 at 500°C for 3 hours (so steady-state was reached). Feed molar composition was 1:1:3 for CH_4:CO_2 :Ar. Space time was set to 0.07 seconds flowrate (calculated at the reactor temperature of 500°C). The catalyst was cooled in argon and analyzed immediately. The BE of Ru $3p_{3/2}$ is 462.0eV.

3.5. References

1. Rostrup-Nielsen J, Christiansen LJ (2011) Concepts in syngas manufacture. Imperial College Press, London

2. Bartolomew CH, Farauto RJ (2006) Fundamentals of industrial catalytic processes. Wiley, New York

3. Bradford M, Vannice M (1999) Catal Rev 41:1–42

4. York APE, Xiao T, Green MLH, Claridge JB (2007) Catal Rev 49:511–560

5. Raudaskoski R, Turpeinen E, Lenkkeri R, Pongra ´cz E, Keiski RL (2009) Catal Today 144:318–323

6. Avetisov AK, Rostrup-Nielsen JR, Kuchaev VL, Bak Hansen J-H, Zyskin AG, Shapatina EN (2010) J Mol Catal A 315:155–162

7. Rostrup-Nielsen JR, Bak Hansen J-H (1993) J Catal 144:38–49

8. Safariamin M, Tidahy LH, Abi-Aad E, Siffert S, Aboukaı¨sA (2009) C R Chimie 12:748–753

9. Nakagawa K, Hideshima S, Akamatsu N, Matsui N, Ikenaga N, Suzuki T (2002) In: Song C et al. (eds) CO_2 conversion and utilization, Chap. 14. ACS symposium series. ACS, Washington DC, pp. 205–233

10. Gallego GS, Batiot-Dupeyrat C, Barrault J, Mondragon F (2008) Ind Eng Chem Res 47:9272–9278

11. Hegde MS, Madras G, Patil KC (2009) Acc Chem Res 42: 704–712

12. Laachir A, Perrichon V, Badri A, Lamotte J, Catherine E, Lavelley JC, El Fallah J, Hilaire L, le Normand F, Quemere E, Sauvion GN, Touret O (1991) J Chem Soc Faraday Trans 87:1601–1609

13. Perrichon V, Laachir A, Bergeret G, Frety R, Turnayan L, Touret O (1994) J Chem Soc Faraday Trans 90:773–781

14. De Leitenburg C, Trovarelli A, Kaspar J (1997) J Catal 166: 98–107

15. Singh P, Hegde MS (2009) Chem Mater 21:3337–3345

16. Bernal S, Calvino JJ, Cifredo GA, Gatica JM, Omil JAP, Pintado JM (1993) J Chem Soc Faraday Trans 89:3499–3505

17. Adachi G, Imanak N, Kang ZC (eds) (2004) Binary rare earth oxides. Kluwer Academic Publishers, Dordrecht

18. Toby BH (2001) J Appl Crystallogr 34:210–213

19. Larson AC, Von Dreele RB (2004) Los Alamos National Labs Report LAUR 86–748: general structure analysis system (GSAS). http://www.ncnr.nist.gov/xtal/software/gsas.html

20. Ernst MA, Sloof WG (2008) Surf Interface Anal 40:334–337 21. Chin SY, Williams CT, Amiridis MD (2006) J Phys Chem B 110:871–882

4. CO_2 Methanation by Ru-doped Ceria: The Role of the Oxidation State on the Surface

4.1. Introduction

The methanation reaction of CO_2

$$CO_2 + 4H_2 \rightarrow CH_4 + 2H_2O_{(gas)} \quad \Delta G_{298K} = -55.8 \text{ kJ mol}^{-1}$$

has been a subject of much interest in recent years.[1–29] Older work has been examined in several reviews.[30,31] Previously[32,33] we examined and discussed ceria doped with several cations and reported that Ru-doped ceria $Ru_{0.05}Ce_{0.95}O_{2-\delta}$, where δ depends on the degree of reduction) is active and selective for CO_2 methanation. Doped oxides, such as $Ru_{0.05}Ce_{0.95}O_{2-\delta}$, are single-phase catalysts[34,35] in which some of the cations have been replaced by other cations (e.g. Ru replaces some of the Ce atoms in the lattice of CeO_2).

When the methanation reaction is performed, the oxide catalyst is exposed to a reductant (H_2) and an oxidant (CO_2). When the reaction is run at the steady state the surface will have a steady state concentration of oxygen vacancies. Here we show that the concentration of these vacancies is an important factor in the activity of the catalyst.

In addition, DFT calculations have shown that in many oxides there is a strong interaction between Lewis bases and Lewis acids.[36] When an oxygen vacancy is created, two unpaired electrons are left behind, which makes the reduced oxide a very strong Lewis base. The more vacancies are created, the stronger the Lewis basicity of the surface. Conceptually, it is possible that an increase in basicity (which is an increase in the ability of the surface to donate electrons – in this case to CO_2) will increase the reactivity of this compound. It is also possible for the surface to be too basic to allow the formation of a hydrogenated product from a carbonate.

Two mechanisms have been proposed for the methanation reaction catalyzed by metals. One assumes that CO_2 is converted to CO which is then converted to methane.[37–41] The other mechanism suggests that CO_2 is methanated directly without the formation of a CO intermediate.[42–45] The direct hydrogenation of CO_2 on Ni(110) has been supported by density functional theory calculations and by experiments.[46,47] In this mechanism CO_2 is converted by reacting with adsorbed H. Previously, we proposed that the direct hydrogenation of a carbonate made from an oxide and CO_2 using a metal that dissociated hydrogen provides an alternate pathway that minimizes the CO by-product.[32] In this case the mechanism is dependent on both the metal and the support used. There is no reason why the mechanism of this reaction catalyzed by an oxide should be the same as one of the mechanisms mentioned above. We propose here that CO_2 forms carbonates and these react with hydrogen to produce methane on a single-phase reducible bi-metallic oxide. The rate-limiting step is carbonate formation. A mechanism that proceeds through the reduction of CO_2 to CO, followed by subsequent CO reduction is unlikely in the case of the $Ru_{0.05}Ce_{0.95}O_{2-\delta}$ catalyst, because exposure of the catalyst to CO + H_2 reduces the catalyst and renders it inactive.

4.2. Experimental

4.2.1. Catalyst Preparation

Ruthenium-doped ceria was prepared by a combustion method described in previous work.[33] The XRD measurements were consistent with Ru atoms substituting the cations in the host oxide but do not prove that the dopants are in the surface layer. However, the fact that a signal from Ru is observed in XPS indicates that Ru is present on the surface or

subsurface. This conclusion is supported by the fact that the chemistry of ceria doped with Ru is very different from that of ceria.

We preconditioned the $Ru_{0.05}Ce_{0.95}O_{2-\delta}$ in three different ways: a "steady-state catalyst" (SSC), a strongly reduced catalyst (SRC), and an oxidized catalyst (OC).

The oxidized catalyst (OC) is preconditioned by exposing the as-prepared catalyst to a flow of 5:1 argon:oxygen for 60 minutes at 450°C, then rapidly cooled to the reaction temperature while purging. The as-prepared catalyst is described in our previous work.

The steady-state catalyst (SSC) is preconditioned by exposing the OC to a mixture of CO_2, H_2, and Ar, at 350°C for one hour at a total flow rate of 10 SCCM, the feed composition $Ar:H_2:CO_2$ = 6.5:4:1. The methanation reaction reaches the steady state under these conditions.

The strongly reduced catalyst (SRC) is preconditioned by exposing the OC to a flow of 30% CH_4 in argon for 2.5 hours at 550°C. The SSC is less reduced than the SRC.

4.2.2. Reactors

Two reactors were used: a packed bed and a commercial reaction cell (the Praying Mantis with a high temperature reaction chamber (HVC), Harrick Scientific Corporation) with windows for Diffuse Reflectance Infrared Fourier Transform Spectroscopy (DRIFTS). Reactivity data were collected using the packed-bed reactor, and DRIFTS data were collected using a separate DRIFTS reactor (unless otherwise noted).

The packed bed was supported with inert quartz wool in a 0.4 cm diameter quartz tube. 25 mg of the catalyst was used with a total flow rate of 10 standard cubic centimeters per minute (SCCM). The feed composition was 6.5:4:1 $Ar:H_2:CO_2$, unless otherwise noted. The

temperature was controlled by a temperature controller (Omega CSC32) using a steel reactor block with heating cartridges that surrounded the reactor tube and pre-heated the gases. A thermocouple in the heating block controlled the temperature and the difference between the steady state bed temperature and the block temperature was less than 5°C at all relevant temperatures. This was determined by measurement in an inert bed. All experiments were carried out at atmospheric pressure.

DRIFTS was performed using an FTIR spectrometer (Thermo Electron Corporation Nicolet 4700) coupled to the reaction cell. The reactor unit incorporates two 6X, 90° off-axis ellipsoid mirrors that are arranged to discriminate against specularly reflected radiation. The total flow rate and feed composition in the DRIFTS reactor were the same as those in the packed-bed reactor. 256 scans of resolution 4 were taken for all sample and background measurements.

Both reactors used mass flow controllers (MKS) for the reactant and carrier gas (argon) flow, and a mass spectrometer (SRS RGA 200) to analyze the product gases. A small stream of product gas was sent to the mass spectrometer, and mass numbers 44, 40, 28, 18, 15, 4, 3, and 2 were assigned to carbon dioxide, argon, carbon monoxide, water, methane, deuterium, HD, and hydrogen, respectively, with appropriate subtractions for overlapping mass numbers. Argon was used as an inert gas and all pressures are normalized to the known argon flow.

4.2.3. Experimental Techniques

We use, unless otherwise stated, a total flow rate of 10 SCCM, the feed composition $Ar:H_2:CO_2 = 6.5:4:1$, and a temperature of 350°C.

To calculate the rate as a function of reactant partial pressures, a given ratio was run for one hour with a flow rate of 10 SCCM and 0.5 mg of the catalyst so that the CO_2 conversion was below 5%. Five replicates were performed, varying the ratios randomly. The dependence of the methanation rate on the partial pressure of hydrogen was determined by changing the partial pressure of hydrogen, keeping the partial pressure of CO_2 constant and adjusting the Ar pressure to keep the total pressure and flow rate constant.

For the isotope experiments, deuterium (and no hydrogen) was used as a feed gas for the entire reaction. The gases were all from Praxair, purity 5.0, with the exception of deuterium, which was 99.7% pure.

When pulses of hydrogen or carbon dioxide were introduced into the system, a Swagelok fitting with a Thermogreen septum was fitted immediately upstream of one of the reactors. One milliliter of gas was injected into the stream using a syringe. The procedure was standardized using an inert bed so that each pulse was reproducible.

When pulses of formic acid were used, a vessel with argon and liquid formic acid was prepared and heated to 50 °C for a suitable vapor pressure. This vapor with formic acid and argon was then injected, using a warm syringe, directly upstream of the catalyst bed in a stream of argon flowing at 10 SCCM.

4.3. Results and Discussion

4.3.1. Three states of the $Ru_{0.05}Ce_{0.95}O_2$ Catalyst

In the methanation reaction, the catalyst is exposed to H_2, which is a reductant, and to CO_2, which is a mild oxidant. As the gases pass through the reactor, the amount of H_2 and CO_2 in the gas is diminished and CH_4 and H_2O are formed. CH_4 is a reductant and water is able to oxidize the reduced oxide. Therefore, all sections of the reactor are exposed

simultaneously to a reducing agent and an oxidizing agent. The reductant creates oxygen vacancies and the oxygen annihilates them. At the steady state the surface of the catalyst will have some oxygen vacancies; we know this because a mass balance shows more oxygen leaving the reactor than entering. The oxygen-vacancy concentration depends on the competition between reduction and oxidation.

Previous work[33] suggested that the $Ru_{0.05}Ce_{0.95}O_{2-\delta}$ catalyst surface is reduced (i.e. it has oxygen vacancies) when the methanation reaction is run under steady-state conditions at 350°C and a 4:1 H_2/CO_2 feed composition. Here we investigate further how the presence of oxygen vacancies on the surface of the catalysts affects their activity for CO_2 methanation. To do this we preconditioned the $Ru_{0.05}Ce_{0.95}O_{2-\delta}$ catalyst to obtain a "steady-state catalyst" (SSC), a strongly reduced catalyst (SRC), and an oxidized catalyst (OC) as described earlier in the experimental section.

4.3.2. The Mechanism of Steady-state Methanation Reaction on the SSC

At the steady state, under the conditions specified above, CO_2 conversion is 40% and the selectivity to methane is 99%.[33] This subsection describes transient chemical experiments and in situ IR spectroscopy used to study the SSC $Ru_{0.05}Ce_{0.95}O_{2-\delta}$ catalyst.

The transient response of the catalyst was determined by using pulse experiments. The surface of the catalyst, when the methanation reaction reached the steady state, has carbon-containing compounds that stay on the surface after the reactants are purged. Their reactivity is observed by first preparing the SSC as described in the experimental section. After that, we turned off the flow of the CO_2 and H_2 mixture, and then purged the reactor with Ar until there was no CO_2, CH_4, or H_2 in the effluent. Throughout these procedures, the temperature

was maintained at 350 °C. After purging was completed, we sent seven H_2 pulses through the reactor. Fig. 1 shows that the SSC catalyst produces methane, when exposed to the hydrogen pulses, even in the absence of CO_2 in the gas. Evidently, when H_2 and CO_2 react at the steady state, they generate carbon-containing compounds on the surface of the SSC, and these react with hydrogen. There is no methane production when the eighth H_2 pulse goes through the reactor.

After the catalyst is exposed to seven H_2 pulses, we pass through the reactor CO_2 pulses and find that they produce CO and no methane. The same is true if the reaction is run at the steady state, purged, and then only CO_2 is added. This indicates two things. (1) Exposure to the H_2 pulses did not create surface hydrogen species that react with CO_2 to form methane. (2) After exposure to the hydrogen pulses, the surface is reduced and CO_2 oxidizes it and produces CO.

Finally, after exposure to the CO_2 pulses, we sent H_2 pulses through the reactor and found that methane is produced again. This indicates that the exposure to CO_2 has reoxidized the surface (since CO was formed) and created carbonaceous species that react with H_2 to produce methane.

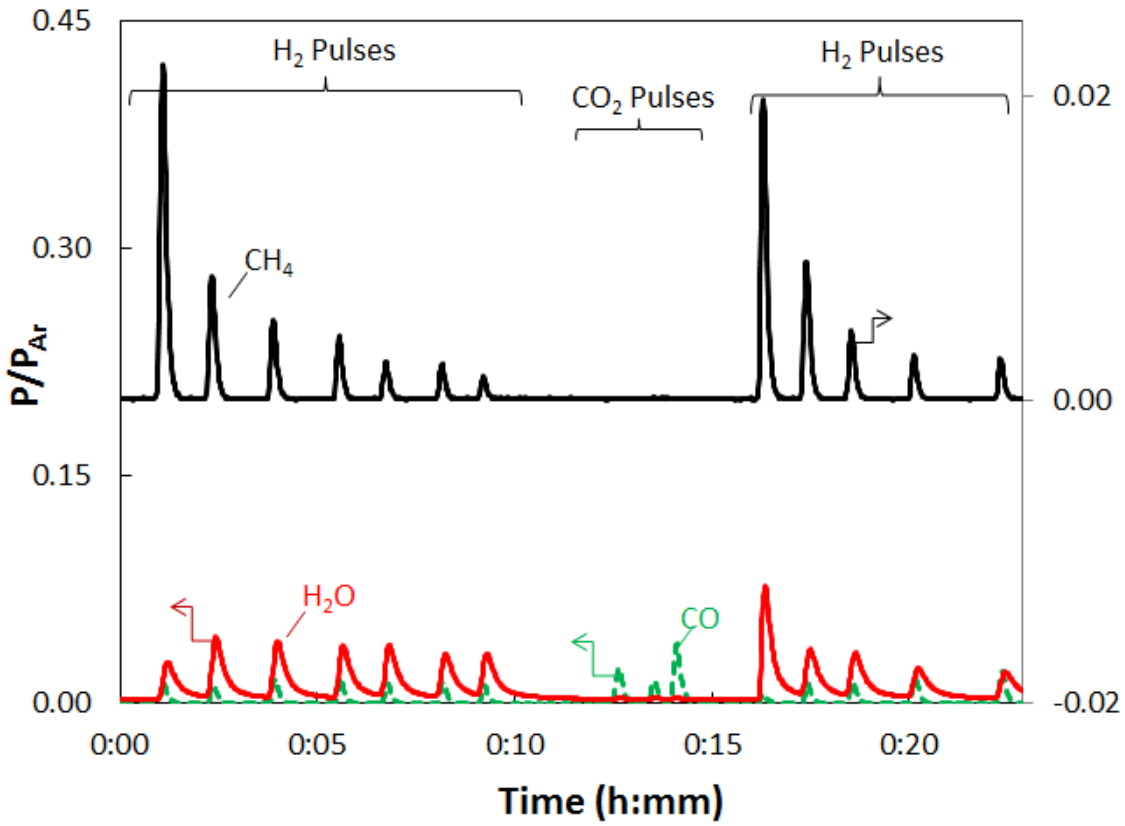

Figure 1. Composition of the effluent produced by the exposure of SSC to seven H_2 pulses, followed by exposure to three CO_2 pulses, followed in turn by exposure to five H_2 pulses, all at 350 °C. Prior to exposure to the pulses, the catalyst was exposed to CO_2 + H_2 at 350 °C until the methanation reaction reached the steady state and then it was purged with Ar until no other gases were detected in the effluent. The arrows indicate whether the ordinate scale for a graph is at the left or at the right.

In the hope of gaining some insight into the mechanism of the hydrogenation reaction, we performed CO_2 methanation with D_2 instead of H_2 . A clear isotope effect was observed (Fig. 2). The rate of methane production was measured in a differential reactor as described in the experimental section. Methanation with deuterium is faster than methanation with hydrogen, at all temperatures between 200 °C and 350 °C (Fig. 2 inset). Such a "negative

isotope effect" has been observed before on metallic catalysts for carbon oxide hydrogenation.[48] Since at least ten elementary reaction steps are needed for methane and water formation and eight of them involve hydrogen, we did not attempt a detailed analysis of these observations.

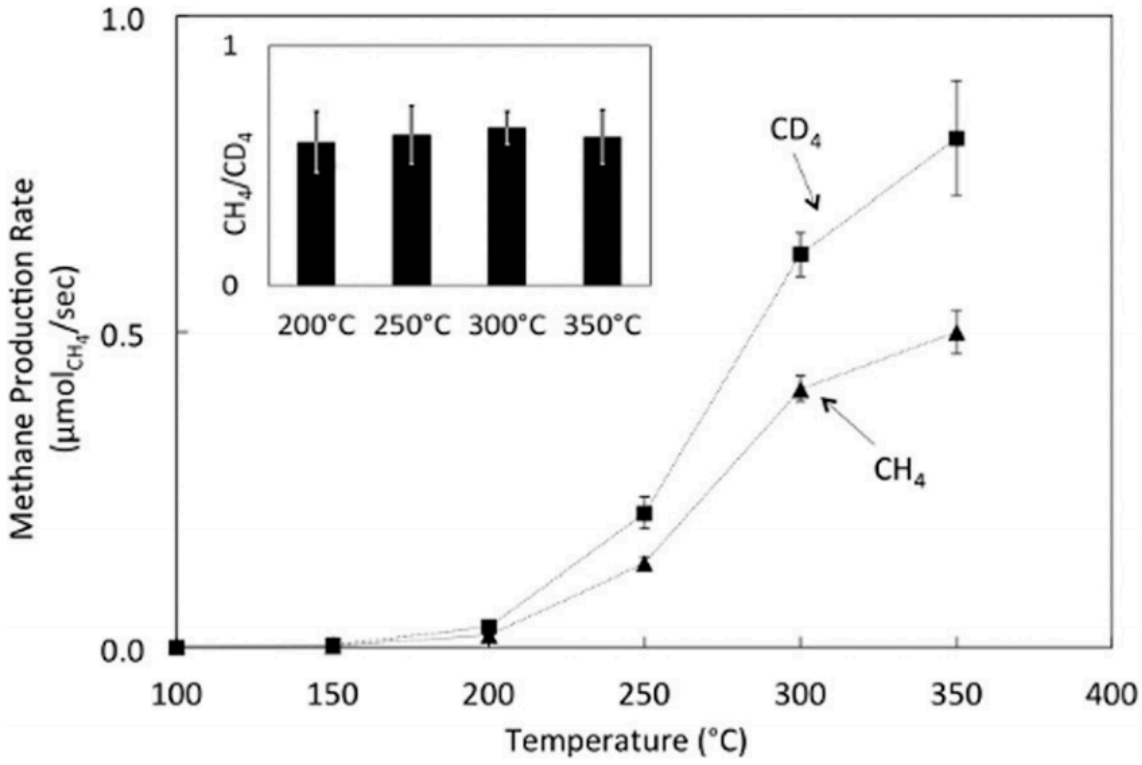

Figure 2. Deuterium isotope effect during CO_2 methanation on SSC. The rate of CH_4 and CD_4 formation for two experiments, one with 4:1 moles CO_2:H_2, and the other with 4 : 1 moles CO_2 : D_2. The rates were determined after waiting one hour to make sure that the steady state was established. The error bars represent 95% confidence interval using four replicates. The inset shows the CH4/CD4 ratio at different temperatures.

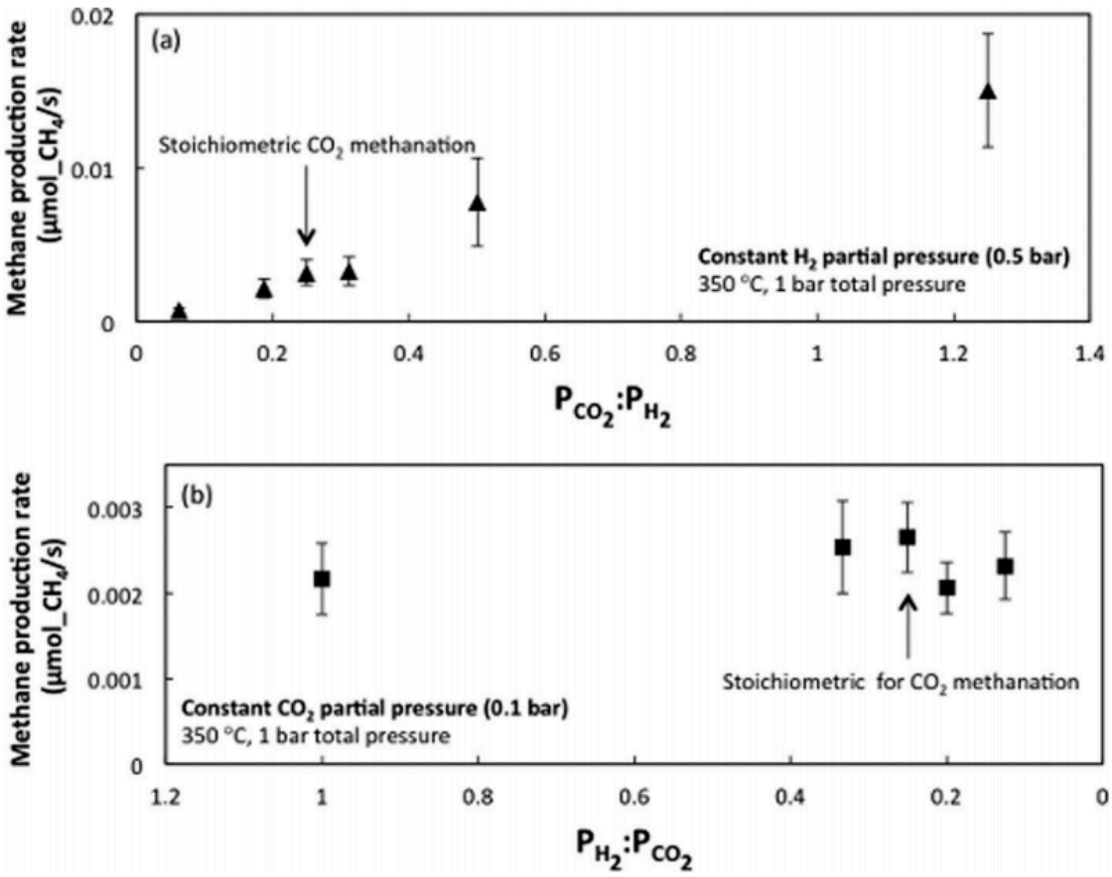

Figure 3. Methanation rate as a function of reactant partial pressures. The rates were determined after the reaction ran for one hour to reach the steady state. The conversion of CO_2 was below 5%. Error bars represent one standard deviation of five replicates. The reactant ratio was varied randomly.

To find whether the rate determining step involved hydrogen and/or carbon dioxide, the dependence of the methanation rate on the partial pressure of hydrogen was determined. A similar experiment was performed to find the rate dependence on the partial pressure of CO_2 (at constant H_2 partial pressure and constant total pressure). The results are shown in Fig. 3. For the conditions used here, the methanation rate changes with the partial pressure of CO_2, but not with the partial pressure of H_2 . Of course the methanation rate would go to zero if

the partial pressure of hydrogen goes to zero, but over the pressure range we report, the rate was independent of hydrogen pressure. The independence of the rate on the pressure of hydrogen, seen under the conditions used here, indicates that hydrogen adsorption is very rapid and changing it (by changing the hydrogen pressure) has no effect on the rate of methane formation. This is not the case for CO_2 adsorption. These observations suggest that the methanation rate is controlled by the formation of the carbon containing intermediates that are subsequently hydrogenated.

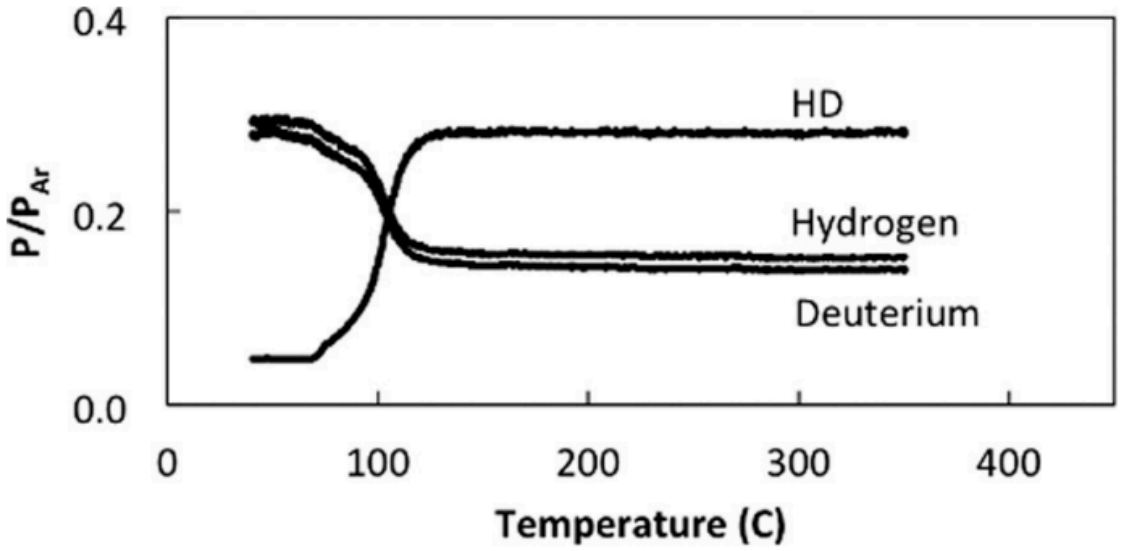

Figure 4. Temperature programmed H_2 -D_2 exchange reaction on the SRC.

To further understand the chemistry of H_2, we studied how the SSC catalyst performs the exchange reaction $H_2 + D_2 \rightarrow 2HD$. Fig. 4 shows the results of temperature-programmed isotope exchange reaction (TPR) performed on the SRC catalyst. The TPR results for the other versions of the $Ru_{0.05}Ce_{0.95}O_{2-\delta}$ catalyst (i.e. strongly reduced or oxidized) look similar; however, there are differences in the light-off temperature and the temperature at which the TPR curves level off. The magnitudes of these temperatures are given in Table 1. We see that the SSC catalyzes the exchange reaction at low temperature. The exchange

starts below 25 °C (which is the lowest temperature to which the reactor can be cooled), while the oxidized, undoped ceria (made by the same combustion method as was $Ru_{0.05}Ce_{0.95}O_{2-\delta}$ and exposed to oxygen for one hour at 450 °C) starts to perform the exchange reaction at 325 °C. There is a substantial difference between oxidized CeO_2 (which we take to be CeO_2 with very few oxygen vacancies) and Ru-doped ceria. Doping with Ru changes substantially how ceria affects the exchange reaction. It is customary to assume that the rate of H–D exchange is limited by the dissociation of H_2. This implies that the SSC dissociates H_2 readily. Note, however, that oxidized $Ru_{0.05}Ce_{0.95}O_{2-\delta}$ behaves, for the exchange reaction, like the steady-state $Ru_{0.05}Ce_{0.95}O_{2-\delta}$ and also like metallic Ru. However, these three catalysts have different performance for methanation. This indicates that these differences do not come from the ability to adsorb and dissociate hydrogen.

Table 1. Results from temperature programmed H_2 –D_2 exchange reaction for various $Ru_{0.05}Ce_{0.95}O_{2-\delta}$ catalysts

Catalyst	H_2/D_2 exchange lightoff temperature (^oC)	Temperature at which HD reaches gas-phase equilibrium (^oC)
Oxidized $Ru_{0.05}Ce_{0.95}O_{2-\delta}$	**<25**	**45**
Reduced $Ru_{0.05}Ce_{0.95}O_{2-\delta}$ (with CH_4)	**75**	**125**
Steady State $Ru_{0.05}Ce_{0.95}O_{2-\delta}$	**<25**	**45**
Oxidized CeO_2	**325**	**N/A**
Ru Metal	**<25**	**43**

4.3.3. IR Detection of Surface Carbonates

The IR spectrum in the wavenumber range 1700–1200 cm^{-1} has a wide band, and many attempts have been made to deconstruct the spectrum into a sum of various peaks, which were assigned to a variety of carbonate-like species.[49–51] These assignments were made for undoped ceria and it is not clear whether they are applicable to ruthenium-doped ceria. Because of this they are not used here. Instead, we generally ascribe the carbon containing surface species that absorb between 1700 and 1200 cm^{-1} as carbonates with multiple structures.

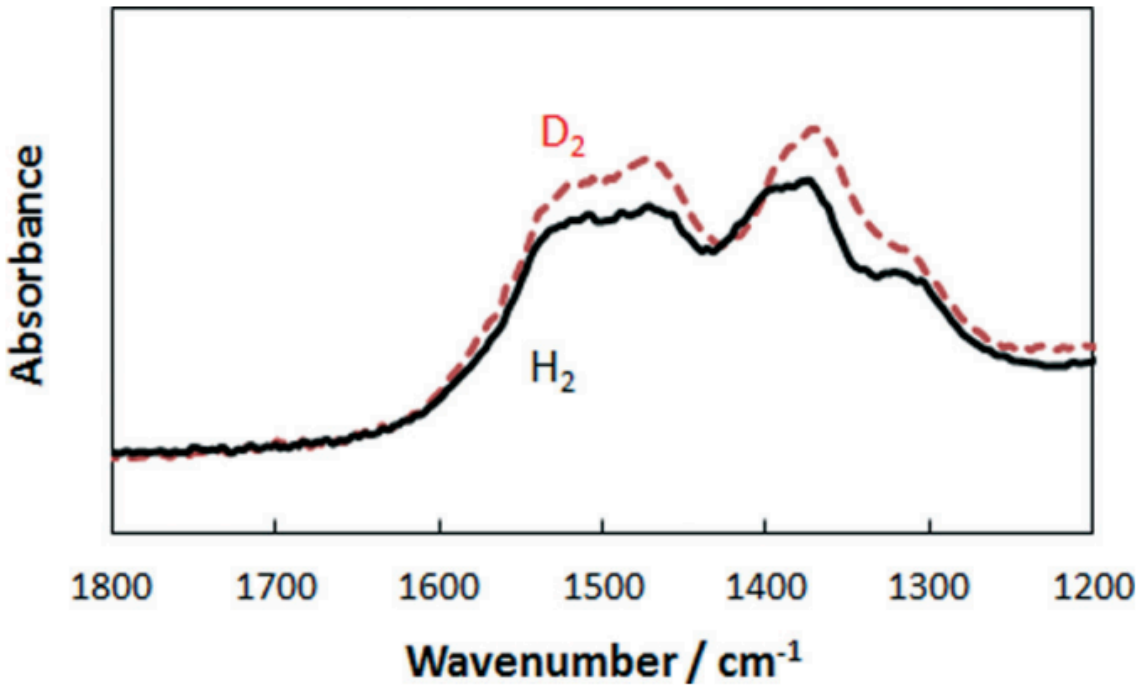

Figure 5. DRIFTS of carbonate-like species taken while flowing H_2 and CO_2 or D_2 and CO_2 through the reactor at 350°C

We used DRIFTS measurements to identify the species present on the surface during steady-state methanation of CO_2. In Fig. 5 we show the IR absorption spectra of the system

after it reached the steady state for the methanation reaction with H_2 or with D_2. There is a shift observed in some of the features in the spectrum when D_2 is used as a methanation reactant instead of H_2. This indicates that there must be hydrogen containing species absorbing in the region, possibly bicarbonates.

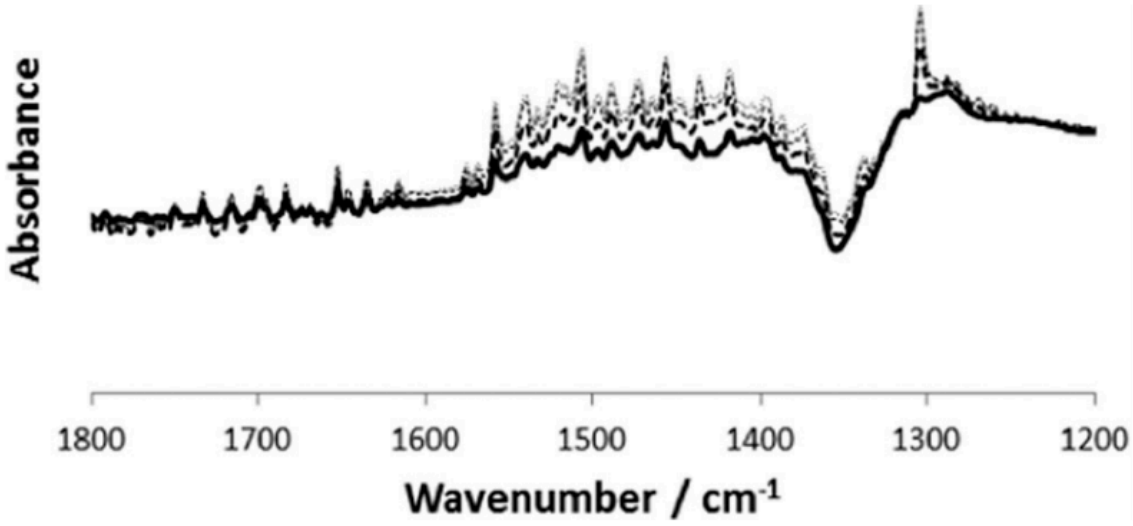

Figure 6. DRIFTS of CO_2 methanation at 350 °C taken at different times after the introduction of H_2 /CO_2 gas into the reactor. The solid line is the spectrum taken at 1 minute, and the spectra above the solid line were taken at 5, 20, and 50 minutes after H_2 /CO_2 introduction. The amount of carbonate increases with time on stream. Background for all spectra was taken after 30 seconds of feed introduction.

The evolution of the IR absorption spectra after stoichiometric carbon dioxide and methane are added is shown in Fig. 6. These data were taken as follows: the OC was prepared and the reactor was completely purged at 350 °C in argon, and IR spectra were taken at 1, 5, 10, 20, and 50 minutes after a mixture of CO_2 and H_2 was introduced in the reactor. When the feed is switched to CO_2 + H_2, it takes 2 minutes for CH_4 production to

reach the steady state. The carbonate build up is very rapid initially and the spectrum is almost complete after 1 minute. However, additional carbonates are slowly formed (as seen by the increased IR absorption) and it takes 50 minutes, after the reaction has reached the steady state, for the IR spectrum to stop changing. We conclude that the additional carbonates, produced after the first minute, do not affect the methanation reaction: they are spectators rather than reaction intermediates.

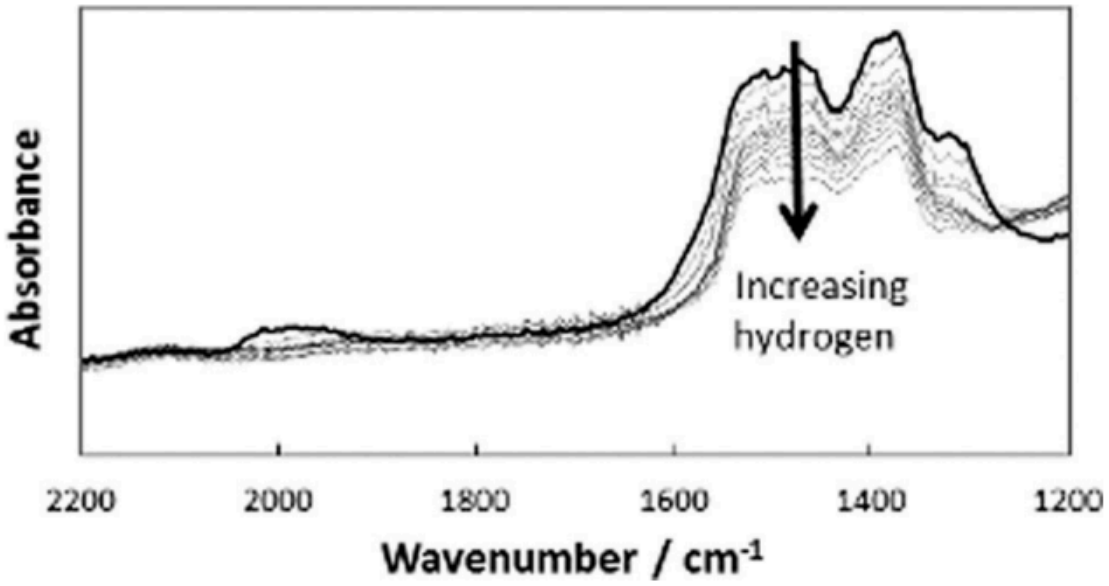

Figure 7. Successive DRIFT spectra taken after each hydrogen pulse passed through the reactor containing SSC. Prior to H_2 introduction, the catalyst performed CO_2 methanation at the steady state for 1 hour at 350 °C.

Fig. 7 shows the IR spectra taken as follows: we ran the reaction of CO_2 and H_2 at 350 °C for one hour and then we shut off the supply of CO_2 and H_2, injected eight H_2 pulses, followed by a steady stream of hydrogen gas in argon. The system produces methane when the first seven pulses pass through the reactor, after which methane production stops. The further introduction of a steady stream of hydrogen does not produce any more methane; however, the intensity of the carbonate spectrum continues to decrease during this time as

indicated by the dotted lines in Fig. 7. If all carbonates on the surface reacted with H_2 to produce methane there should be no IR absorption at the frequencies assigned to carbonates. However, the IR spectrum shows that at the time when pulsing H_2 through the system yields no methane, there is a substantial amount of carbonate left on the surface. This experiment shows that most surface carbonates are spectators and that the methane is formed by the reaction of H_2 with a minority carbonate species.

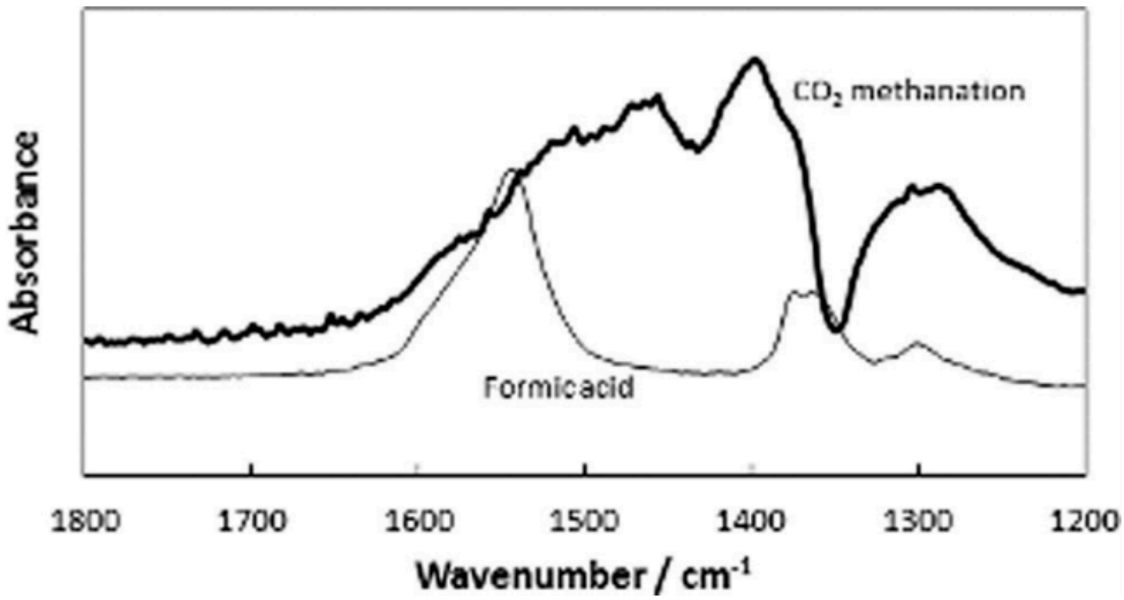

Figure 8. DRIFT spectrum of oxidized $Ru_{0.05}Ce_{0.95}O_{2-\delta}$ in Ar at 110 °C after injection of formic acid in the reactor, compared to the DRIFT spectrum of the carbonaceous compounds on the SSC performing CO_2 methanation at 350 °C.

It is also interesting to note that upon introduction of H_2 to the SSC, the intensity of the carbonate peaks between 1600 cm^{-1} and 1300 cm^{-1} decreases uniformly. The peaks below 1300 cm^{-1} behave in an opposite manner: they absorb more light as the hydrogen reacts with

the surface. We do not have a reliable explanation for this; a possibility is that some carbonates are converted to bicarbonates.

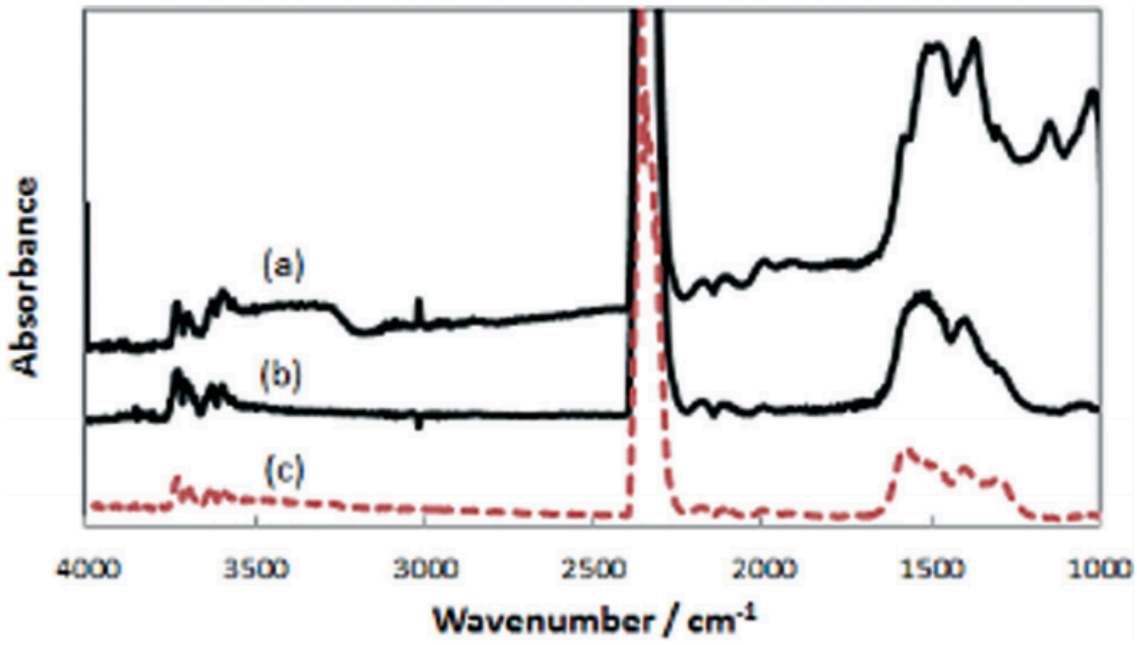

Figure 9. DRIFT spectra during CO_2 methanation at 350 °C of $Ru_{0.05}Ce_{0.95}O_{2-\delta}$ catalysts having different degrees of reduction. Initially, the catalyst was reduced in CH_4 at 550 °C for 2.5 hours (to prepare SRC) and cooled to 350 °C before H_2 + CO_2 was introduced and the spectrum was taken (c). In the second experiment SRC was exposed to CO_2 , at 350 °C for 30 minutes and then the catalyst was exposed to H_2 + CO_2 and the spectrum was taken (b). In the third experiment SRC was exposed to CO_2 at 550 °C for 60 minutes and then H_2 + CO_2 was introduced at 350 °C and the IR spectrum was taken (a). We subtracted the absorbance spectrum of SRC from all three spectra.

When the reaction is run at the steady state and then the reactor is purged, the concentration of carbonaceous surface intermediates must be equal to or greater than the amount of methane subsequently produced by hydrogen pulses. Using the data from the

experiment in Fig. 1, the amount of methane produced from seven hydrogen pulses is 1.9×10^{-6} mol. This corresponds to 5.7×10^{-6} moles of carbonaceous surface intermediates per square meter of catalyst if the intermediates are not stacked. This would be equivalent to a cross section of 0.29 nm^2 per molecule. This high carbonate surface density may be due to more than one adsorption layer and suggests that the late-forming "spectator" carbonates (above) can be mobilized into the reaction pathway.

Table 2. Methane yield for the CO_2 + H_2 reaction over the SSC and SRC as well as the yield over the SRC exposed to CO_2 prior to running the methanation reaction.

* 30% CH4 in argon at 550°C for 2.5 hours.

Conditions	Methane yield
Steady state CO_2 methanation	40%
SRC (i.e. after reduction treatment*)	3%
SRC (i.e. after reduction treatment*) + 60 minutes in 10% CO_2 at 350 C	10%
SRC (i.e. after reduction treatment*) + 60 minutes in 10% CO_2 at 550 C	35%

Discussion of CO_2 methanation on other catalytic systems often invokes a mechanism that has a formate intermediate. To test whether such an intermediate is present on our catalyst, we exposed the oxidized catalyst (OC) to formic acid at 25 °C. When the surface is heated, the compound formed by formic acid adsorption decomposes, at 150 °C, into CO_2

and water (observed downstream in the mass spectrometer). This suggests that a formate would not be stable at the methanation temperature. If we pass formic acid through the reactor at 350 °C, the formic acid decomposes into CO_2 and water, and the IR spectrum shows the presence of carbonates but not of a formate. We assume that the carbonate is formed by the CO_2 produced by the decomposition of the formic acid. Running formic acid and hydrogen through the SSC bed at 350 °C produces methane. We assume, given the fact that the formic acid decomposes at 150 °C, that the methane is formed by the reaction of H_2 with the CO_2 produced by formic acid decomposition.

The IR spectrum of the compound formed by exposing the oxidized catalyst (OC) to formic acid at 115 °C (before decomposition) is shown in Fig. 8 together with the IR spectrum of the catalyst during steady-state methanation reaction. The compound formed by exposing the oxidized catalyst to formic acid has peaks at 1544, 1369, 1355, and 1292 cm^{-1}. When heated to desorb the carbonates, no formate peaks were observed, and the initial surface species – formed with very small doses of reactants – were not characteristic of formate. When the spectra before and after addition of hydrogen to the surface species to produce methane are subtracted, the result did contain absorbance peaks at the values we observed for formate. While the IR spectra do not rule out the presence of the formate, the fact that the formate decomposes at temperatures much lower than the steady state methanation temperature suggests to us that the compounds formed by exposing the surface to formic acid are not likely to be methanation intermediates.

4.3.4. The Chemistry of the Oxidized Catalyst (OC)

The oxidized catalyst exposed to a mixture of H_2 and CO_2 produces very little methane initially at 350 °C. However, in time the hydrogen reduces the surface and the performance

of the system drifts towards that of the steady-state catalyst. This is of course expected. The OC surface does not adsorb CO_2 at 350 °C and no carbonates are formed by exposure to CO_2. Pulsing carbon dioxide over the OC while measuring the IR spectrum showed no carbonates.

However, if the OC is exposed to CO (to reduce it), carbonates appear. We think that this takes place in two stages. Initially CO reduces the surface to form CO_2 and oxygen vacancies. Once oxygen vacancies are present, the CO_2 produced by the oxidation of CO is able to form carbonates. The IR spectrum of these carbonates is very similar to that observed when the methanation is carried out at the steady state. The main conclusion drawn from these experiments is that the fully oxidized $Ru_{0.05}Ce_{0.95}O_{2-\delta}$ surface does not act as a methanation catalyst unless the surface is sufficiently reduced.

4.3.5. The Chemistry of the SRC Surface

We have shown that the surface of $Ru_{0.05}Ce_{0.95}O_{2-\delta}$ is reduced when the methanation reaction is performed at the steady state and that if it is not reduced it is not active – i.e. the OC is not active. Next we show that the degree of reduction matters: if the catalyst is too reduced (i.e. it has too many oxygen vacancies), its performance is poor.

Table 2 shows the performance of the $Ru_{0.05}Ce_{0.95}O_{2-\delta}$ catalyst having different degrees of reduction. When a mixture of H_2 and CO_2 is run through the reactor with a SRC catalyst, CO_2 is converted to CO, hydrogen is converted to water, and the methane yield is 3% (Table 2). If the SRC is exposed to a flow of 10% CO_2 in argon at 350 °C for one hour, CO is produced and the surface is partially reoxidized. The catalyst obtained in this way was used for methanation, and the methane yield was 10% (Table 2). The SRC exposed to 10% CO_2 in argon at 550 °C for one hour (Table 2) has a methane yield of 35%; this is better than the

SRC but not as good as the SSC. These experiments show that over-reducing the Ru-doped oxide diminishes its catalytic activity severely, but the reduced catalyst can be reactivated by oxidation with CO_2. However, if we run through the SRC bed a mixture of $CO_2 : H_2 = 1 : 4$ at 350 °C for one hour, only very small amounts of methane are produced. This indicates that in the presence of H_2, carbon dioxide is very slow to reoxidize the surface. This is not surprising since H_2 acts as a reductant.

The variation of methane yield with the degree of reduction might be related to a change in the structure of surface intermediates. To investigate this we have taken a DRIFTS spectrum of the SRC exposed to $CO_2 + H_2$. This is shown as a red dotted line in Fig. 9. The double peak at ~2100 cm^{-1} is typical of gas-phase CO and consistent with the fact that the reduced catalyst converts CO_2 to CO. If the reactor is purged, this double peak decreases with the same rate as the other gas-phase peaks due to methane. As discussed above, this double peak is not present on the SSC. For these reasons, we conclude that these peaks are mainly gas-phase CO. The carbonate band is visible and the spectrum has peaks at 1523 cm^{-1}, 1373 cm^{-1}, and 1267 cm^{-1}. In all spectra shown in Fig. 9, we have subtracted the spectrum of the SRC that has not been exposed to CO_2.

Next we oxidized partially the SRC by exposing it to CO_2 for 30 minutes at 350 °C. This limited exposure to CO_2 does not oxidize the catalyst to completely recover its activity towards CO_2 methanation (see Table 2). After having exposed the SRC to CO_2 (as described above), we ran $CO_2 + H_2$ through the reactor at 350 °C, and took the spectrum shown in the middle of Fig. 9. The intensity of the carbonate band is increased and its peaks shift to 1485 cm^{-1}, 1373 cm^{-1}, and 1018 cm^{-1}. Therefore this partially reoxidized catalyst, which is more

active for methanation than the SRC (see Table 2), produces different carbonates on its surface.

In the third experiment we exposed the SRC to CO_2 (10% CO_2 and 90% Ar) at 350 °C for one hour. After that we introduced CO_2 and H_2 into the reactor at 350 °C, and took the IR spectrum shown in the top of Fig. 9. The catalyst oxidized with CO_2 for one hour is practically as active as the SSC. The absorption band of the carbonates on this surface is the most intense and its peaks shift again (as compared to the other two spectra). The peaks are at 1454 cm^{-1}, 1467 cm^{-1}, 1126 cm^{-1}, and 1009 cm^{-1}.

Although it is difficult to assign these peaks to specific structures on the surface, it is clear that different carbonates are present on the surface depending on the degree of reduction of the surface. This suggests that the carbonates present in the bottom spectrum cannot be hydrogenated to methane, those in the middle spectrum are hydrogenated slowly, and those in the top spectrum are more readily hydrogenated (see Table 2 and Fig. 9).

The hydroxyl peaks in the 3600–3700 cm^{-1} region indicate that running the methanation reaction on the SRC produces fewer hydroxyls than on the more oxidized surfaces. In particular, in the top spectrum in Fig. 9, the hydroxyl band is much larger and it extends to a lower wavenumber than in the other two spectra. This is natural since there is less oxygen on the reduced surface and the oxygen that is present is likely to make strong bonds with the reduced oxide and be less reactive towards hydrogen. Although the hydroxyls are present, they do not react with CO_2 (according to the experiments described above, in which turning off the H_2 flow during methanation reaction stops the production of methane).

In summary, too much reduction of the $Ru_{0.05}Ce_{0.95}O_{2-\delta}$ catalyst diminishes its activity. It is likely that this happens because on this system CO_2 forms different, less reactive

carbonates. The reduced catalyst is also less active for H_2/D_2 exchange but this is not likely to limit its methanation activity because the exchange does occur at 75 °C (see Table 1).

4.4. Conclusion

We have investigated methanation on the same combustion synthesized Ru-doped ceria catalyst preconditioned in three distinct ways. One (OC) was exposed to oxygen for a long time before being used as a catalyst. Another (SSC) was exposed to H_2 and CO_2 until the methanation reaction reached the steady state. A third (SRC) was prepared by exposure to methane at 550 °C for 2.5 hours. We performed serial pulse experiments using H_2, CO_2, and CO and found that the OC is inactive when exposed to H_2 and CO_2 until it is reduced (by H_2 or CO); the surface is continually reduced until the surface reaches the suitable state of reduction, at which point the methanation reaction reaches a steady state where only methane and water are produced. This means that OC exposed to H_2 and CO_2 evolves to become the SSC. The OC surface reacts readily with H_2 and CO and catalyzes the H_2/D_2 exchange reaction at temperatures below 25 °C. This is a reactive surface but it is not a good methanation catalyst until the surface is properly reduced.

The SRC catalyst does not methanate a mixture of CO_2 and H_2. It is also less active in catalyzing the H_2/D_2 exchange. Prolonged exposure of the SRC to CO_2 will oxidize the surface until it is as good as a methanation catalyst as the SSC. However, exposure to H_2 and CO_2 does not oxidize the surface to an active methanation state; CO_2 alone can reoxidize the SRC but not when H_2 is present. When the SRC is exposed to CO_2 and H_2 , carbonates are formed on the surface but they are not active towards methanation. The IR spectra of these

carbonates differ from that of the carbonates formed when the reaction is run under steady-state conditions (reached when starting from the oxidized catalyst).

The SSC catalyst is a partially reduced $Ru_{0.05}Ce_{0.95}O_{2-\delta}$ surface and the degree of reduction is important for determining its performance. We observed a similar situation for the dry reforming of methane over the same catalyst.[52] If the reaction is carried out at the steady state, then purged, and then exposed to only hydrogen, methane is produced. Methane is not produced if the surface is first exposed to only H_2, and then to only CO_2. We conclude that methane is formed by the reaction of hydrogen with a carbon-containing intermediate formed by the adsorption of CO_2. IR spectroscopy, when the reaction is run at the steady state, shows a band in a wave-vector region previously attributed to carbonates. We found that most of these carbonates are not intermediates in the methanation reaction. Spectra taken at various times after the methanation reaction was initiated show that methane production reaches the steady state in less than a minute and most (but not all) carbonate spectrum is established in the first minute. However, a slight build-up of carbonates continues long after methane production reaches the steady state. If the reaction is run at the steady state and then the CO_2 supply is turned off and IR spectra are taken, we find that the hydrogen continues to produce methane for a while, and the intensity of the carbonate band changes: for most wavelengths the absorption decreases but for some wavelengths (corresponding perhaps to bicarbonates) it increases. A strong absorption in the carbonate region is present even after prolong exposure to hydrogen no longer produces methane. These combined experiments suggest that a carbonate is a reaction intermediate, but most surface carbonates are not involved in methane production. The methanation rate depends on CO_2 partial pressure and is independent of the partial pressure of H_2. The lack of H_2 -

pressure dependence, together with the low temperature at which the D_2 –H_2 exchange takes place, indicates that the rate of supplying hydrogen is not a limiting step.

The mechanism of the methanation reaction is very complicated because one must add eight hydrogen atoms to the CO_2 and remove two water molecules from the surface. Experiments using formic acid or CO instead of CO_2 suggest that the formate created by formic acid adsorption is not an intermediate. During the hydrogenation process it is very likely that a species containing carbon and one oxygen atom and some hydrogen is an intermediate. However this intermediate is not what one forms by exposing the surface to hydrogen and CO. Such a feed contains two strong reductants and reduces the oxide without producing any methane.

It is possible that an increase in basicity (which is an increase in the ability of the surface to donate electrons) may have something to do with the fact that the catalyst is a reduced (but not too reduced) surface. In particular, it is possible that electron donation to CO_2 to produce a negatively charged CO_2 will increase the reactivity of this compound.

4.5. References

1 S. Abello, C. Berrueco and D. Montane, Fuel, 2013, 113, 598–609.

2 P. A. U. Aldana, F. Ocampo, K. Kobl, B. Louis, F. Thibault-Starzyk, M. Daturi, P. Bazin, S. Thomas and A. C. Roger, Catal. Today, 2013, 215, 201–207.

3 A. Beuls, C. Swalus, M. Jacquemin, G. Heyen, A. Karelovic and P. Ruiz, Appl. Catal., B, 2012, 113, 2–10.

4 A. Borgschulte, N. Gallandat, B. Probst, R. Suter, E. Callini, D. Ferri, Y. Arroyo, R. Erni, H. Geerlings and A. Zuttel, Phys. Chem. Chem. Phys., 2013, 15, 9620–9625.

5 D. C. D. da Silva, S. Letichevsky, L. E. P. Borges and L. G. Appel, Int. J. Hydrogen Energy, 2012, 37, 8923–8928.

6 R. Guttel, Chem. Eng. Technol., 2013, 36, 1675–1682. Catal. Sci. Technol.

7 Y. H. Huang, J. J. Wang, Z. M. Liu, G. D. Lin and H. B. Zhang, Appl. Catal., A, 2013, 466, 300–306.

8 S. Hwang, U. G. Hong, J. Lee, J. H. Baik, D. J. Koh, H. Lim and I. K. Song, Catal. Lett., 2012, 142, 860–868.

9 S. Hwang, U. G. Hong, J. Lee, J. G. Seo, J. H. Baik, D. J. Koh, H. Lim and I. K. Song, J. Ind. Eng. Chem., 2013, 19, 2016–2021.

10 S. Hwang, J. Lee, U. G. Hong, J. H. Baik, D. J. Koh, H. Lim and I. K. Song, J. Ind. Eng. Chem., 2013, 19, 698–703.

11 J. Janlamool, P. Praserthdam and B. Jongsomjit, J. Nat. Gas Chem., 2011, 20, 558–564.

12 W. R. Kang and K. B. Lee, Korean J. Chem. Eng., 2013, 30, 1386–1394.

13 A. Karelovic and P. Ruiz, Appl. Catal., B, 2012, 113, 237–249.

14 A. Karelovic and P. Ruiz, J. Catal., 2013, 301, 141–153.

15 S. Kato, A. Borgschulte, D. Ferri, M. Bielmann, J. C. Crivello, D. Wiedenmann, M. Parlinska-Wojtan, P. Rossbach, Y. Lu, A. Remhof and A. Zuttel, Phys. Chem. Chem. Phys., 2012, 14, 5518–5526.

16 J. H. Kwak, L. Kovarik and J. Szanyi, ACS Catal., 2013, 3, 2449–2455.

17 H. Z. Liu, X. J. Zou, X. G. Wang, X. G. Lu and W. Z. Ding, J. Nat. Gas Chem., 2012, 21, 703–707.

18 J. Liu, C. M. Li, F. Wang, S. He, H. Chen, Y. F. Zhao, M. Wei, D. G. Evans and X. Duan, Catal. Sci. Technol., 2013, 3, 2627–2633.

19 K. Muller, M. Stadter, F. Rachow, D. Hoffmannbeck and D. Schmeisser, Environ. Earth Sci., 2013, 70, 3771–3778.

20 M. D. Porosoff and J. G. G. Chen, J. Catal., 2013, 301, 30–37.

21 R. Razzaq, C. S. Li, N. Amin, S. J. Zhang and K. Suzuki, Energy Fuels, 2013, 27, 6955–6961.

22 N. Srisawad, W. Chaitree, O. Mekasuwandumrong, A. Shotipruk, B. Jongsomjit and J. Panpranot, React. Kinet., Mech. Catal., 2012, 107, 179–188.

23 C. Swalus, M. Jacquemin, C. Poleunis, P. Bertrand and P. Ruiz, Appl. Catal., B, 2012, 125, 41–50.

24 S. Tada, T. Shimizu, H. Kameyama, T. Haneda and R. Kikuchi, Int. J. Hydrogen Energy, 2012, 37, 5527–5531.

25 R. B. Zhang, L. Liang, X. R. Zeng, J. Y. Shang, T. Wang and J. X. Cai, Acta Phys.-Chim. Sin., 2012, 28, 1951–1956.

26 G. L. Zhou, T. Wu, H. M. Xie and X. X. Zheng, Int. J. Hydrogen Energy, 2013, 38, 10012–10018.

27 G. L. Zhou, T. Wu, H. B. Zhang, H. M. Xie and Y. C. Feng, Chem. Eng. Commun., 2014, 201, 233–240.

28 H. W. Zhu, R. Razzaq, C. S. Li, Y. Muhmmad and S. J. Zhang, AIChE J., 2013, 59, 2567–2576.

29 Y. Zhu, S. R. Zhang, Y. C. Ye, X. Q. Zhang, L. Wang, W. Zhu, F. Cheng and F. Tao, ACS Catal., 2012, 2, 2403–2408.

30 W. Wang, S. P. Wang, X. B. Ma and J. L. Gong, Chem. Soc. Rev., 2011, 40, 3703–3727.

31 G. Centi and S. Perathoner, in Studies in Surface Science and Catalysis, ed. S.-E. Park, J.-S. Chang and K.-W. Lee, Elsevier, 2004, vol. 153, pp. 1–8.

32 J.-N. Park and E. W. McFarland, J. Catal., 2009, 266, 92–97.

33 S. Sharma, Z. P. Hu, P. Zhang, E. W. McFarland and H. Metiu, J. Catal., 2011, 278, 297–309.

34 M. S. Hegde, G. Madras and K. C. Patil, Acc. Chem. Res., 2009, 42, 704–712.

35 E. W. McFarland and H. Metiu, Chem. Rev., 2013, 113, 4391–4427.

36 H. Metiu, S. Chrétien, Z. Hu, B. Li and X. Sun, J. Phys. Chem. C, 2012, 116, 10439–10450.

37 M. Marwood, R. Doepper and A. Renken, Appl. Catal., A, 1997, 151, 223–246.

38 J. L. Falconer and A. E. Zağli, J. Catal., 1980, 62, 280–285.

39 G. D. Weatherbee and C. H. Bartholomew, J. Catal., 1982, 77, 460–472.

40 A. L. Lapidus, N. A. Gaidai, N. V. Nekrasov, L. A. Tishkova, Y. A. Agafonov and T. N. Myshenkova, Pet. Chem., 2007, 47, 75–82.

41 D. E. Peebles, D. W. Goodman and J. M. White, J. Phys. Chem., 1983, 87, 4378–4387.

42 C. Schild, A. Wokaun and A. Baiker, J. Mol. Catal., 1990, 63, 243–254.

43 C. Schild, A. Wokaun, R. A. Koeppel and A. Baiker, J. Phys. Chem., 1991, 95, 6341–6346.

44 S. Fujita, H. Terunuma, H. Kobayashi and N. Takezawa, React. Kinet. Catal. Lett., 1987, 33, 179–184.

45 S. Fujita, H. Terunuma, M. Nakamura and N. Takezawa, Ind. Eng. Chem. Res., 2002, 30, 1146–1151.

46 E. Vesselli, L. D. R. X. Ding, A. Baraldi, L. Savio, L. Vattuone, M. Rocca, P. Fornasiero, M. Peressi, A. Baldereschi, R. Rosei and G. Comelli, J. Am. Chem. Soc., 2008, 130, 11417–11422.

47 H.-J. Freund and M. W. Roberts, Surf. Sci. Rep., 1996, 25, 225–273.

48 P. F. M. T. van Nisselrooij, J. A. M. Luttikholt, R. Z. C. van Meerten, M. H. J. M. de Croon and J. W. E. Coenen, Appl. Catal., 1983, 6, 271–281.

49 M. Marwood, F. Van Vyve, R. Doepper and A. Renken, Catal. Today, 1994, 20, 437–448.

50 C. Li, Y. Sakata, T. Arai, K. Domen, K.-I. Maruya and T. Onishi, J. Chem. Soc., Faraday Trans. 1, 1989, 85, 929–943.

51 C. Binet, A. Badri, M. Boutonnet-Kizling and J.-C. Lavalley, J. Chem. Soc., Faraday Trans., 1994, 90, 1023–1028.

52 A. R. Derk, G. M. Moore, S. Sharma, E. W. McFarland and H. Metiu, Top. Catal., 2013, 57, 118–124.

5. Methane Oxidation by Lanthanum Oxide Doped with Cu, Zn, Mg, Fe, Nb, Ti, Zr, or Ta: The Connection Between the Activation Energy and the Energy of Oxygen-vacancy Formation

5.1. Introduction

Oxides catalyze many interesting alkane-activation reactions, but often their performance is poor. One of the strategies for improving an oxide's catalytic activity is to replace a fraction of the cations in its surface layer with other cations. For example, to improve a La_2O_3 catalyst we might replace some of the La ions with Mg. In this case we call Mg a substitutional dopant (or dopant) and La_2O_3 the host oxide.

It has been frequently assumed that the energy of oxygen-vacancy formation, ΔE_v, is an indicator of the reactivity of surface oxygen atoms: smaller ΔE_v means a more reactive surface oxygen. This is relevant to oxidation reactions, catalyzed by oxides, which take place through a Mars–van Krevelen mechanism. In this mechanism the reductant (e.g., an alkane) reacts with one or more oxygen atoms in the surface layer, is converted to the oxidation product, and causes the formation of one or more oxygen vacancies in the surface. The reduced oxide made in this way is reoxidized by gas-phase O_2. In most cases the reoxidation step is fast (at least at the oxygen concentrations used in most experiments) and therefore the overall oxidation rate is controlled by the reaction of the reductant with the oxygen atoms in the surface layer. In the case of alkane oxidation the rate-limiting reaction is the dissociative adsorption that converts the gas-phase R-H into an alkoxide ($R–O_s$, where O_s is an oxygen atom in the surface layer) and a hydroxyl ($H–O_s$). If the surface oxygen atoms are made more reactive (by some chemical modification such as doping), the $R–O_s$

and the $H–O_s$ bonds are stronger, and the energy of the dissociative adsorption reaction, ΔE_{dis}, is higher (more exothermic). According to the Brønsted-Evans-Polanyi rule there is a linear relationship between the activation energy $E_{a,dis}$ for the dissociative adsorption and the reaction energy ΔE_{dis}: the more exothermic the reaction, the lower the activation energy. This chain of assumptions leads us to state the following rule: the smaller the energy ΔE_v of oxygen vacancy formation, the smaller the activation energy $E_{a,dis}$ for the dissociative adsorption of an alkane. Since dissociation is the rate limiting step in alkane activation, $E_{a,dis}$ dominates the measured effective activation energy, E_a, of the alkane oxidation reaction. In summary, we expect that the effective activation energy Ea for methane oxidation by various doped-lanthana catalysts should be an increasing function of the energy of oxygen vacancy formation ΔE_v in the surface of the doped oxide.

In this article we test this qualitative rule suggested by the calculations, by preparing La_2O_3 doped with Cu, Zn, Mg, Fe, Nb, Ti, Zr, or Ta. We use density functional theory (DFT) to calculate ΔE_v for these systems and experiments to measure the effective activation energy E_a for catalytic oxidation of methane. Our results confirm the rule. Moreover, we find that the measured E_a is linearly related to the calculated ΔE_v. The graph of E_a versus ΔE_v consists of two straight lines: one valid for La_2O_3 doped with lower-valence dopants and the other for La_2O_3 doped with higher-valence dopants.

We emphasize that it is practically impossible to prepare a doped oxide surface that is guaranteed to have the same morphology and composition as the models used in calculations. Because of this, we expect the correlations suggested (and tested) here to be qualitative only. If deviations occur, we do not know whether they are due to errors in DFT or to our inability to prepare the intended material.

5.2. DFT Calculation Methodology

The details of the calculations were explained in previous work [1]. Briefly, spin-polarized DFT calculations were performed using the VASP [2] program, with the rPBE functional [3] and PAW basis [4]. We used a La_2O_3 (001) slab 15 atomic layers thick, with a 2 x 2 supercell. The size of the vacuum layer was 15 Å and we tested that the results did not change when the size was increased. All ionic positions were optimized until the forces acted on them were < 0.02 eV/Å. Applying Hubbard's correction does not qualitatively affect the results [1] and therefore we did not use DFT+U. One should keep in mind that DFT calculations are not accurate and that our goal is to verify a qualitative rule.

5.3. Experimental Methodology

It is difficult to determine for certain whether a catalyst is substitutionally doped. The possibility that the dopant forms very small oxide clusters on the surface of the host oxide is very difficult to rule out because such clusters will not be detectable by XRD and will have an XPS signature different from the bulk oxide of the dopant. Nevertheless, we considered our La_2O_3 catalyst to be doped when (1) lanthanum oxide (or oxy-carbonate) is the only phase present in XRD and (2) the dopant is detectable by XPS. The latter condition indicates that the dopant is present at or near the surface. For each synthesis of the doped oxides, the dopant concentration was varied so that the material met the conditions (1) and (2). These precautions do not guarantee that we have prepared a doped oxide since the dopants might make oxide clusters that are not crystalline or large enough to be detected by XRD.

All catalysts were prepared by combustion synthesis, a method employed extensively by Hegde [5]. The precursors were lanthanum(III) nitrate, titanium(IV) oxyacetylacetonate, niobium(V) ammonium oxalate, tantalum(V) chloride, zirconyl nitrate, zinc(II) nitrate,

magnesium nitrate, copper(II) nitrate, iron(III) nitrate. Oxalic dihydrazide (ODH) was used as fuel. Typically, 2.50 g of lanthanum(III) nitrate hexahydrate, and the appropriate amount of dopant precursor (e.g., 80 mg of titanium oxyacetylacetate to make 5% titanium-doped La_2O_3) and of ODH (0.85 g for previous example) are dissolved in a minimal amount of water (Millipore). This mixture is put in a Pyrex^{TM} dish and placed into a furnace, which is heated to 450 ^{o}C to induce spontaneous combustion. The combustion takes place very rapidly and produces an oxide powder. The combustion method for doped-oxide synthesis starts with a solution in which the cations of the dopant and those of the host oxide are uniformly mixed and the formation of the oxide is very rapid, which minimizes the opportunity for phase separation into segregated oxides.

X-ray Diffraction (XRD, Philips X'PERT diffractometer) and X-ray photoelectron spectroscopy (XPS, Kratos Axis Ultra X-ray Photoelectron Spectrometer) measurements were performed on all catalysts to confirm that the material has the structure of lanthanum oxide and that the dopant is present near the surface.

Catalytic characterization was performed with a packed bed reactor with a very short residence time (differential reactor). 25 mg of catalyst was mixed with 50 mg of 200 mesh GC-grade alumina and supported in the center of a quartz tube (4 mm inner diameter) with quartz wool. Gases were delivered using mass-flow controllers (MFCs, supplied by MKS). The mole ratio of methane:oxygen:argon was maintained at 1:1:3. Catalyst void fraction was measured volumetrically with methanol and the gas flowrate was set such that the space time was 0.18 s calculated at 20 ^{o}C, unless otherwise noted. The reactor effluent was measured by differentially pumped mass spectrometry (SRS). All gases had a purity of at least 99.99 %. The temperature was controlled and varied using a programmable controller

(OMEGA CSC32). Software for the control and logging of the reactor studies was written using LabView™. Effective activation energies were calculated by performing linear regressions on Arrhenius plots. The data chosen to be regressed had small, but non-zero, methane conversion in order to determine an accurate conversion rate.

5.4. Results and Discussion

To avoid the formation of separate dopant oxide-phases, we kept the molar concentration of tantalum and niobium at 1 %. Titanium, magnesium, and zinc allowed a doping level of 2.5 % without showing separate dopant-oxide phases in XRD. Finally, the concentration of zirconium, copper, and iron dopants had to be 5 % to be observable in XPS. Even at this high concentration no phase separation was observed in XRD.

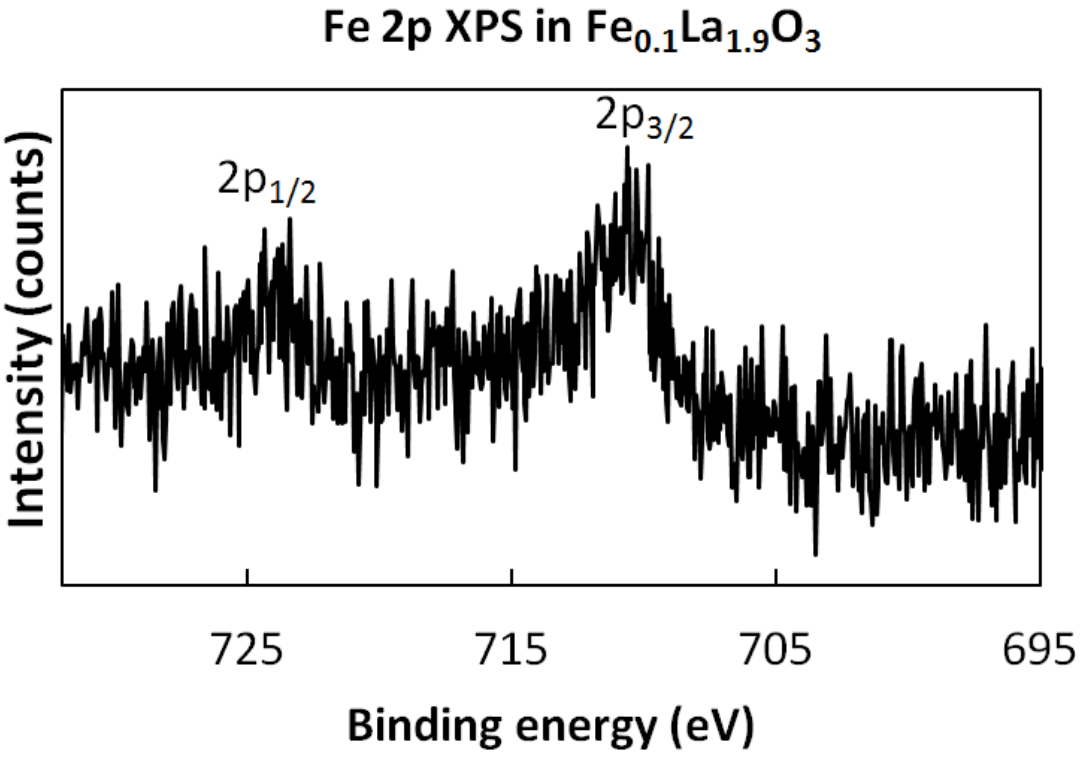

Figure 1. XPS of the Fe 2p orbital of iron in $Fe_{0.1}La_{1.9}O_3$. XPS shows Fe is present on the surface of the $Fe_{0.1}La_{1.9}O_3$ particles. Furthermore, iron is likely to be in the +3 state based on a $2p_{3/2}$ binding energy of 710.7 eV.

As an example, we show in Fig. 1 the XPS spectrum of 5 % iron-doped lanthanum oxide. XPS shows the presence of iron on the catalyst surface and suggests that the iron is in the +3 oxidation state. XRD of 5 % iron-doped lanthanum oxide is shown in Fig. 2 and is representative of all the catalysts discussed herein. La_2O_3 is the predominant phase with some lanthanum oxy-carbonate present. The presence of an oxy-carbonate at the surface of La_2O_3 has been reported previously [6].

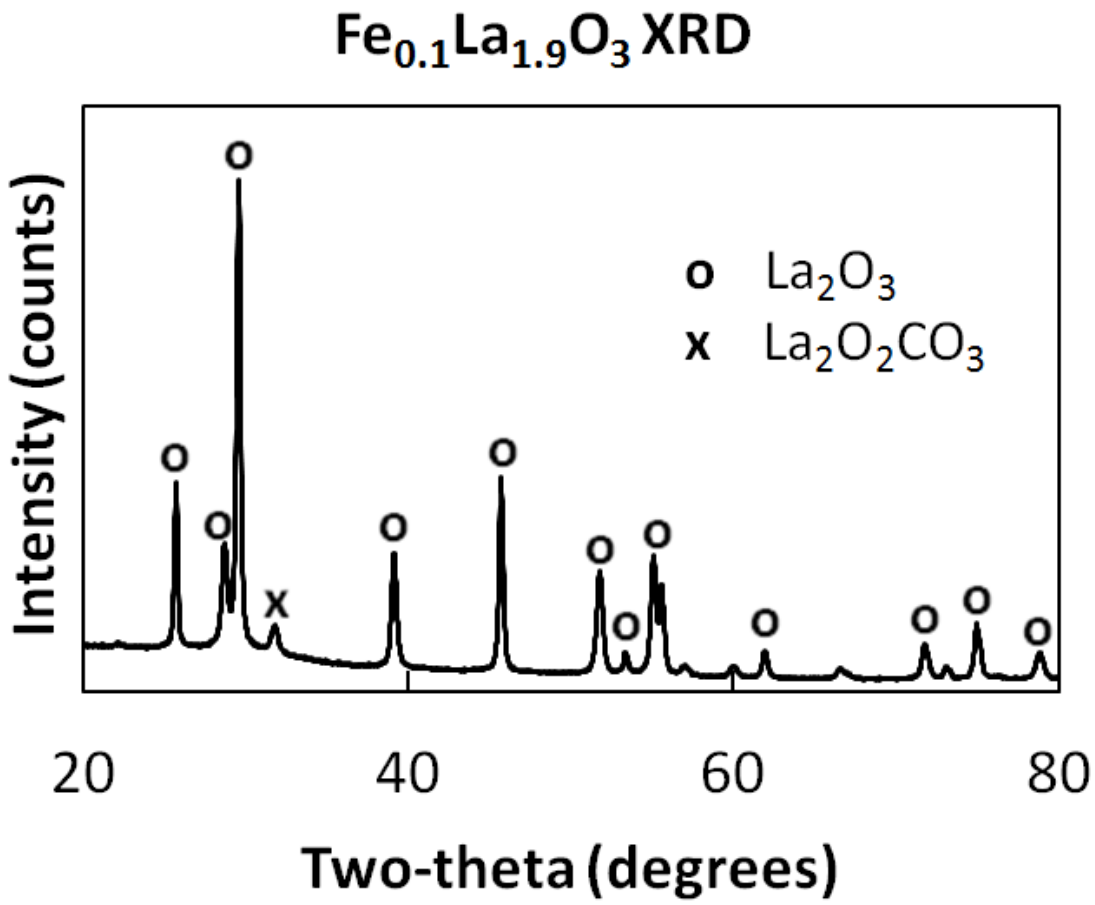

Figure 2. X-ray diffraction of 5 % iron-doped lanthanum oxide, $Fe_{0.1}La_{1.9}O_3$. XRD shows predominantly La_2O_3 with one peak corresponding to lanthanum oxy-carbonate (which forms when the sample is exposed to the atmosphere). No iron-containing phase is observed

Temperature-programmed reaction measurements for doped lanthanum oxide catalysts show that methane is oxidized to synthesis gas, carbon dioxide, and water, with (1 %) conversion usually starting at 450 ^{o}C. The exceptions were zirconium-doped and tantalum-doped La_2O_3 , which showed no activity below 500 ^{o}C. A typical conversion-temperature graph is shown in Fig. 3, for 2.5 % titanium-doped lanthanum oxide catalyst. The TPR data were used to determine activation energies (Fig. 4). We used low-conversion data for rate measurements to ensure that we have a differential reactor.

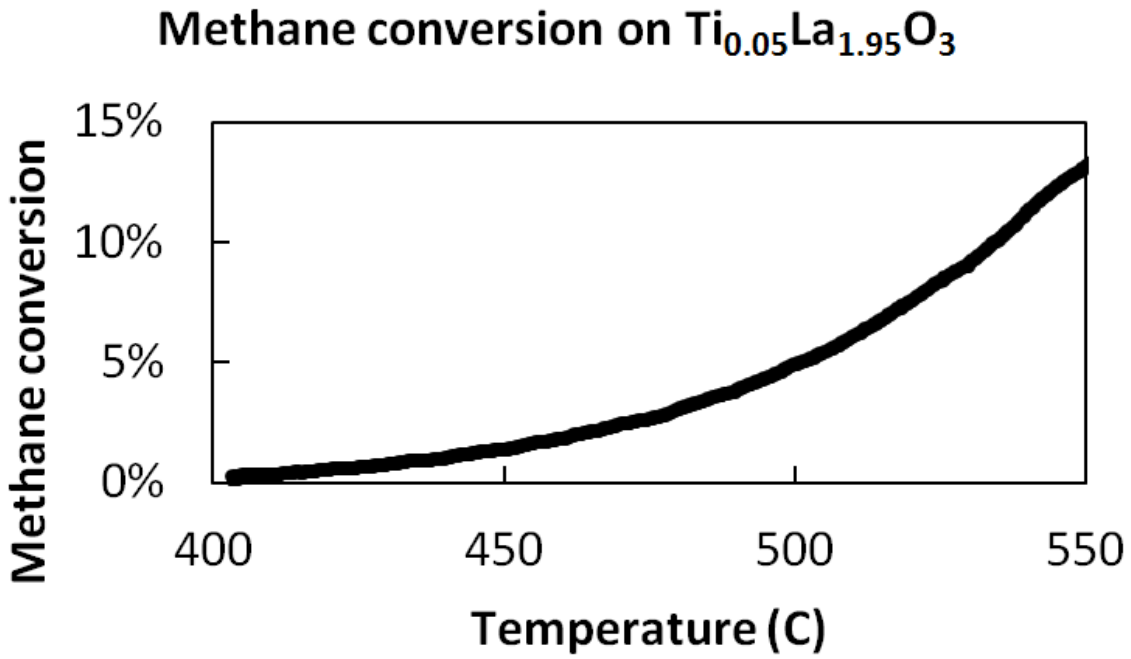

Figure 3. Temperature-programmed reaction of methane with oxygen catalyzed by 2.5 % titanium-doped lanthanum oxide. Methane conversion was calculated from carbon

monoxide and dioxide concentrations measured by mass spectrometry. Temperature was ramped linearly while the feed composition was held constant at a ratio of CH_4:O_2:Ar 1:1:3, with a space time of ~0.2 s

Figure 5 and Table 1 compare the effective activation energy (derived from the slope of a Arrhenius plot of ln(r) vs 1/T (see Fig. 4) where r is the rate of methane consumption) to the oxygen-vacancy formation energy calculated by DFT. The dependence of E_a on ΔE_v can be fitted by two straight lines: one for Cu-, Zn-, Mg- and Fe-doped La_2O_3 and the other for Nb-, Zr-, Ti-, and Ta-doped La_2O_3 and the undoped La_2O_3 .

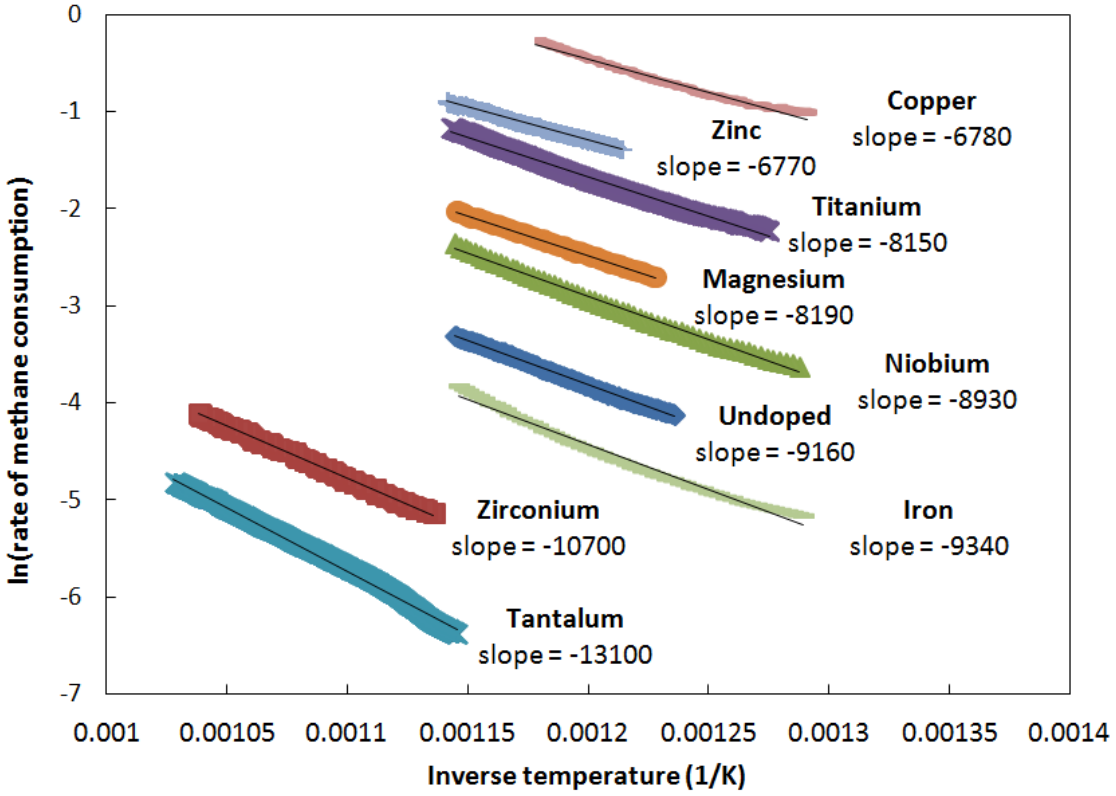

Figure 4. Arrhenius plots for methane oxidation catalyzed by La_2O_3 and doped La_2O_3

We suggest that the reason for the existence of two curves can be understood based on the difference between the valence of the dopant and that of La. The valence of a dopant is,

by definition, the valence the dopant has in its own oxide. For example, an Mg dopant is divalent because its only oxide is MgO. This definition cannot be used a priori for atoms that form multiple stable oxides. For example, NbO, NbO_2, and Nb_2O_5 are all stable so it is difficult to decide a priori what valence Nb has when it is a substitutional dopant in La_2O_3. We use the term 'lower valence' (or 'higher-valence') dopant when the valence of the dopant is lower (respectively, higher) than the valence of the cation of the host oxide. For example, Mg is a lower-valence dopant in La_2O_3, and Zr is a higher-valence dopant in La_2O_3.

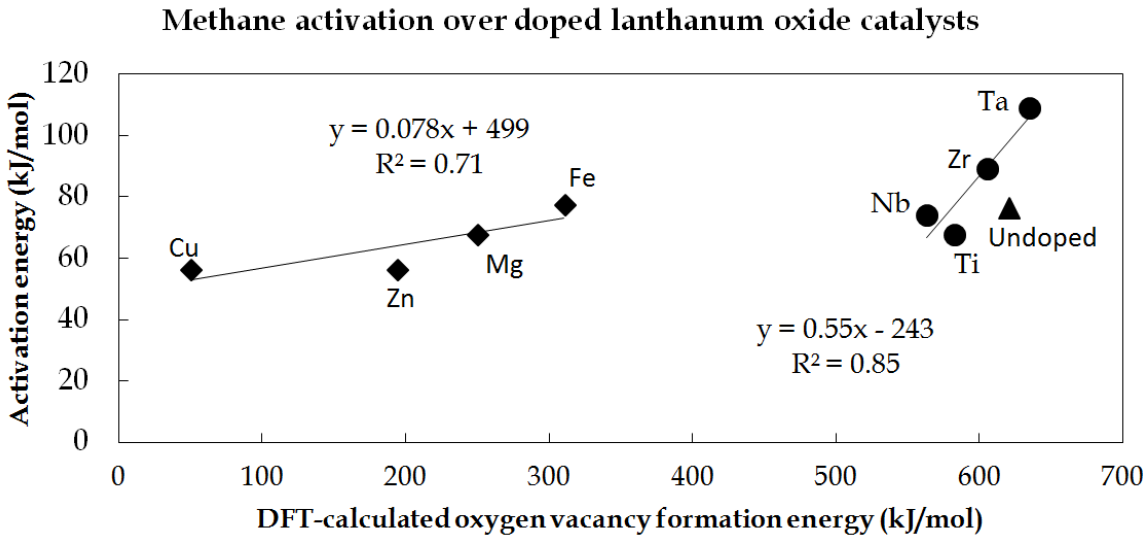

Figure 5. The dependence of the measured effective activation energy for methane oxidation on the energy of oxygen-vacancy formation calculated by DFT. Diamonds indicate lower-valence dopants. Circles indicate higher-valence dopants

The DFT calculations have shown that the presence of a lower-valence dopant (e.g., Fe, Cu, Mg, Zn) in the surface of La_2O_3 lowers the energy of oxygen-vacancy formation (Table 1) very substantially. Previous calculations [7] have shown that lower-valence dopants, such as Cu, Mg, Zn, lower the activation energy for methane dissociation. The higher-valence

dopants have a very small effect on ΔE_v. In previous work [8], we suggested that a higher valence dopant in the surface layer of an oxide adsorbs O_2 from gas-phase and activates it. This adsorbed O_2 can react with methane and oxidize it. In this mechanism the oxygen in the oxidation product originates from the gas, not from the oxide surface. Another possibility [9] is that, because the gas-phase O_2 adsorbs on the higher-valence dopant, one should consider that the dopant is the MeO_2 group, where Me is the doping cation. Since the O_2 ties down (by making bonds) some of the electrons of M, the MO_2 dopant is a lower-valence dopant that activates the surface oxygen atoms near it. Thus a higher-valence dopant has a double role: it activates the oxygen adsorbed from the gas and also the oxygen next to it (when it adsorbs O_2 to form MeO_2).

Table 1. The measured effective activation energy and the calculated energy of oxygen-vacancy formation

Dopant	E_a(kJ/mol)	E_{vac} (kJ/mol)
Undoped	76	621.1
Zr	89	605.7
Ti	68	582.6
Ta	109	634.6
Nb	74	563.3
Fe	78	310.6
Cu	56	50.2
Mg	68	249.8
Zn	56	193.9

This possible difference in oxidation mechanism may explain why we obtain two straight lines for the dependence of E_a on ΔE_v: one for lanthana doped with LVDs and another for lanthana doped with HVDs.

We conclude by summarizing for the reader some of the uncertainties in this work. First, one is never sure that a doped oxide has been prepared with the dopant atoms isolated and contained in the surface layer. Second, the calculations of ΔE_v contain errors inherent to DFT and the flat-slab model we use is not a faithful model of the surface of a laboratory catalyst. Finally, the effect of the lower valence dopants in the experiments may be chemically compensated [9] by co-adsorption of Lewis bases such as H or CH_3. One hopes that in spite of these uncertainties the trend (obtained by performing the same reaction, catalyzed by the same host oxide, doped with a variety of dopants) is robust and can serve as a guide for designing new doped oxide catalysts.

5.5. References

1. Li B, Metiu H (2010) J Phys Chem C 114:12234

2. Kresse G, Hafner J (1994) Phys Rev B 49:14251

3. Hammer B, Hansen L, Nørskov J (1999) Phys Rev B 59:7413

4. Blochl PE (1994) Phys Rev B 50:17953

5. Hegde MS, Madras G, Patil KC (2009) Acc Chem Res 42:704

6. Adachi G, Imanak N, Kang ZC (2004) Binary Rare Earth Oxides. Kluwer Academic Publishers, Dordrecht

7. Li B, Metiu H (2011) J Phys Chem C 115:18239

8. Pala RGS, Tang W, Sushchikh MM, Park J-N, Forman AJ, Wu G, Kleiman-Shwarsctein A, Zhang J, McFarland EW, Metiu H (2009) J Catal 266:50

9. Hu Z, Li B, Sun X, Metiu H (2011) J Phys Chem C 115:3065

6. Catalyst and Oxygen Carrier Compatibility Oxidative Dehydrogenation of Alkanes

6.1. Introduction: Benefits and goals of a SHC Solid Reactant

The use of selective hydrogen combustion materials in catalytic dehydrogenation may provide a more effective production process for alkenes by shifting the equilibrium to the product side. Ethylene, propylene, butadiene, and styrene are the building blocks for numerous polymers and are used in various commercial processes. As a result, commercial supply and demand for these alkenes is large, making high production efficiency of large economic interest. At present, there are two main routes to produce propylene at scale: cracking of alkanes and naphthas and the catalytic dehydrogenation of alkanes, usually employing a platinum-tin or chromium oxide catalyst on alumina. The dehydrogenation equilibrium favors propylene only at high temperature or low pressure, adding costly utilities and compression overhead. Furthermore, cryogenic separation of the hydrogen from the unconverted propane increases capital costs. Improvements of the dehydrogenation process usually focus on increasing the yield by shifting the equilibrium through removal of one of the reaction products. This can be done either physically with the use of a membrane[2] or by chemically reacting the hydrogen to form water, while avoiding the reaction of propane or propylene. The latter approach can be accomplished using any suitable oxidant, typically gaseous oxygen[3] or metal oxides.[1,4] Depending on the oxidant, the thermodynamics of hydrogen combustion can greatly offset the endothermicity of the reaction of propane dehydrogenation. This is a great advantage because the two most common industrial processes (OLEFLEX and CATOFIN) are heat transfer limited[5].

To our knowledge, only one report exists of a selective hydrogen combustion oxygen carrier successfully combined with a propane dehydrogenation catalyst for ODH.[1] Grasselli and co-workers used PtSn/ZSM-5 as a dehydrogenation catalyst and bismuth oxide on silica (prepared using Ludox AS-40) as an oxygen carrier[4]. When the Bi_2O_3/SiO_2 oxygen carrier was initially cycled at 550^oC with air and a simulated propane dehydrogenation stream (propane, propylene, and hydrogen), it cycled very well: there was no decrease in selectivity and the carrier maintained 80% of its activity after 120 cycles (losing less than 0.2% of activity per cycle).[4] When the same oxygen carrier was added to a dehydrogenation catalyst based on platinum, tin, and ZSM-5, it had excellent initial yields of 48 % (whereas, non-oxidative dehydrogenation has a yield of 20 % and an equilibrium limitation of 28 %). When the catalyst and oxygen carrier composite system were cycled, the yield dropped by about 5% per cycle compared to its original performance.[1] In other words, the hydrogen-combusting oxygen carrier lost 0.2% of its performance per cycle, whereas the ODH system (catalyst and oxygen carrier) lost 5% of its performance per cycle. Thus, the loss of hydrogen combustion activity can not explain all, or even a majority, of the ODH system's degredation. Nevertheless, Grasselli and coworkers conclude, "The decline, ascribed to the loss of Bi_2O_3 dispersion on the SiO_2 support caused by the deep reduction cycling, is too large for the process to be practical as it stands, using the catalysts employed. Therefore, a more rugged SHC catalyst composition must be identified to make the process practical."[1] This analysis, finding a more cyclable oxygen carrier, has guided research in the area since.

Numerous oxygen carriers for selective hydrogen combustion for use in propane dehydrogenation have been proposed that try to address the design criteria of activity, selectivity, and cyclability, but omit compatibility criteria between the catalyst and oxygen

carrier. These oxygen carriers include metal oxide doped ceria,[6,7,8, 9, 10, 11, 12] $PbCrO_4$,[13] perovskites,[14] and mixed oxides with ceria.[8] Many (11 of 14) of the oxygen carriers propose their combination with chromia-based catalysts or the CATOFIN process (which uses a chromia-based catalyst). Despite the commonality of this proposed scheme, no reports exist of investigating the combination of selective hydrogen combustion with a chromium-based dehydrogenation catalyst. Besides the aforementioned report by Grasselli and coworkers, none of the proposed oxygen carriers were combined with a dehydrogenation catalyst; rather, their performance was measured in a simulated dehydrogenation stream of hydrogen and hydrocarbons.

In this work, we employ a new bismuth oxide oxygen carrier, showing it is active for hydrogen combustion and selective against hydrocarbon combustion. Previous work has focused on silica-supported bismuth(III) oxide, but ascribed deactivation to sintering. In an attempt to keep the bismuth oxide well-dispersed, we employ a high surface area, mesoporous silica support (SBA-15)[15]. Moreover, we assess it is stable with respect to oxidizing and reducing cycles of hydrogen and oxygen. We then combine this oxygen carrier with a typical platinum-based dehydrogenation catalyst (5 wt% Pt and 5 wt% Sn on silica) and show propylene yields above those achievable without hydrogen combustion. We confirm cycle degradation results in the literature, but ascribed the deactivation method to Bi_2O_3/SBA-15 deactivating the catalyst, likely due to poisoning (as determined by reaction data and XPS), in contrast to prevailing assumptions in the literature. In hopes of finding a more robust catalyst to pair with Bi_2O_3/SBA-15, we subsequently combine the oxygen carrier with a commonly proposed and studied catalyst based on chromium (13 wt% Cr_2O_3, 3 wt% K_2O supported on alumina). Surprisingly, we show that this catalyst is fundamentally

incompatible with any water, either produced by hydrogen combustion or being directly fed into the reactor. With this new insight, we propose that future work on ODH via selective hydrogen combustion must include compatibility studies between catalyst and oxygen carrier, as both can be individually promising, but fail when coupled. Furthermore, chromium-based catalysts may be fundamentally incompatible with selective hydrogen combustion regimes, unless promoters or other protective means can be found to prevent deactivation by water.

6.2. Experimental

6.2.1. Synthesis

The platinum-tin on silica catalyst was prepared using the following procedure adapted from previous work[16]. Davidson Davicat SI 1254 silica granules were used as a support for the platinum-tin catalyst. First, 5 wt% platinum was added by impregnating the support with aqueous solution of H_2PtCl_6 (Sigma Aldrich, ACS reagent grade). The solution was then dried in vacuum at room temperature, heated at 100 °C for 0.5 hours, then heated to 350 °C for 2 hours in air. After cooling, 5 wt% tin was added by impregnating the resulting solid with $SnCl_2$ (Sigma Aldrich, ACS reagent grade). After drying at room temperature in vacuum, the catalyst was calcined at 100 °C for 0.5 hours, followed by heating to 700 °C in air for 1.5 hours. Finally, the catalyst was pre-treated with hydrogen (10% hydrogen for 1 hour at 550^{o}C) and used for reaction studies.

The chromium based catalyst was prepared using procedures common in the review literature.[17] Briefly, incipient wetness impregnation of $Cr(NO_3)_3$ and KNO_3 (Sigma Aldrich, ACS reagent grade) on gamma-Al_2O_3 (Alpha Aesar) was employed to impregnate precursors for a final composition of 13 wt% Cr_2O_3 and 3 wt% K_2O on gamma-Al_2O_3. This

slurry was calcined at 10 ^{o}C/min to 600^{o}C for 6 hours and allowed to cool slowly. Finally, the catalyst was pre-treated with hydrogen (10% hydrogen for 1 hour at 550^{o}C) and used for reaction studies.

We prepared 50 wt% Bi_2O_3 on SBA-15 as an oxygen carrier using wet impregnation. A solution of $Bi(NO_3)_3$ (Sigma Aldrich, ACS reagent grade) was added to SBA-15 (Sigma Aldrich). This mixture was then calcined at 10 ^{o}C/min to 600^{o}C for 6 hours and allowed to cool slowly.

6.2.2. Reactor studies

To chemically asses the interactions between reactants, catalysts, and oxygen carriers, all reaction studies took place in a packed-bed reactor. The packed bed was supported with inert quartz wool in a 0.4 cm diameter quartz tube. The temperature was controlled by a temperature controller (Omega CSC32) using a steel reactor block with heating cartridges that surrounded the reactor tube and pre-heated the gases. All reactions were performed isothermally at 550^{o}C and at atmospheric pressure. A thermocouple in the heating block controlled the temperature. The gas flowrates were controlled by mass flow controllers (MKS) and two-position valves (VICI). The reactor effluent was measured by an online mass spectrometer (Stanford Research Systems RGA) operating at a pressure of 1 x 10^{-5} Torr. Argon was used as an inert carrier. All reported effluent concentrations are normalized to argon. The carbon and hydrogen balances were generally within 2%.

For selective hydrogen combustion studies, 200mg of Bi_2O_3/SBA-15 was loaded into a quartz tube and heated to 500^{o}C in flowing argon. At temperature, reactant gases were simultaneously turned on using VICI valves in addition to the 10 standard cubic centimeters per minute (SCCM) argon: 0.5 SCCM propane, 0.5 SCCM propylene, and 0.5 SCCM

hydrogen. For Bi_2O_3/SBA-15 cycling studies, alternatingly oxidative and reducing cycles of 600 seconds were employed with 10 SCCM purges of argon for 60 seconds. Both cycles were performed at 550^{o}C. The oxidizing cycle was 3 SCCM of oxygen and 10 SCCM of argon. The reducing cycle was 2.8 SCCM of hydrogen and 10 SCCM of argon.

During measurements of oxidative dehydrogenation of propane, the reactor bed was composed of a mixture of 100mg of Bi_2O_3/SBA-15 and either 100mg of the platinum-based catalyst or 300mg of the chromium-based catalyst. For experiments in which the effect of the addition of steam was investigated, the same conditions were used with an addition of 0.4 SCCM of water to the feed (40% of argon). For oxidative regeneration cycles to replenish oxygen in the oxygen carrier and/or decoke the dehydrogenation catalyst, 8 % oxygen in argon was used, by slowly stepping up the oxygen concentration by 1 %/minute from 0 to 8 % to avoid any exotherm.

6.2.3. X-Ray Photoelectron Spectroscopy

X-ray photoelectron spectra were obtained on a Kratos Axis Ultra Spectrometer with a monochromatic Al−Kα source. Powder samples were mounted on a stainless steel sample holder using double-sided tape. The residual pressure inside the analysis chamber was below 7 x 10^{-9} torr. Spectra of Pt and Bi 5f levels were acquired at a pass energy of 40 eV with a dwell time of 1.2 seconds per point. Spectra were calibrated to the C 1s peak from adventitious hydrocarbons, expected at a binding energy of 285.0 eV. For peak fitting of the spin−orbit doublets, the $f_{7/2}$ to $f_{5/2}$ peak area was constrained to a ratio of 4/3.

6.3. Results and discussion

6.3.1. Selective Hydrogen Combustion by Bi_2O_3/SBA-15

These experiments serve to determine how much hydrogen, relative to propane and propylene, are combusted by the solid oxygen carrier, Bi_2O_3/SBA-15. A gaseous composition composed of 5% propane, 5% propylene, and 5% hydrogen in argon was chosen to simulate the composition within a propane dehydrogenation reactor. Ideally, the Bi_2O_3/SBA-15 would combust all (or nearly all) of the hydrogen to water and not combust or coke any of the propane or propylene. In addition to selectively combusting hydrogen over propane and propylene, the oxygen carrier needs to be regenerable with oxygen.

The results are shown in Figure 1. Propane is unreacted, while 98 % of the propylene is unreacted. On the contrary, 52% of the total hydrogen is converted to water with peak conversion of ca. 80%. When presented in an equal molar ratio (as in this case), Bi_2O_3/SBA-15 combusts 50 times the hydrogen as propane and propylene. By integrating the water peak and comparing it to the amount of oxygen present in Bi_2O_3/SBA-15, we calculate 80% of solid oxygen is converted to water. These results compare well to other Bi_2O_3-based selective hydrogen combustion oxygen carriers in the literature, such as Bi_2O_3/SiO_2,[1] with high hydrogen conversion and low reactivity towards propylene and propane.

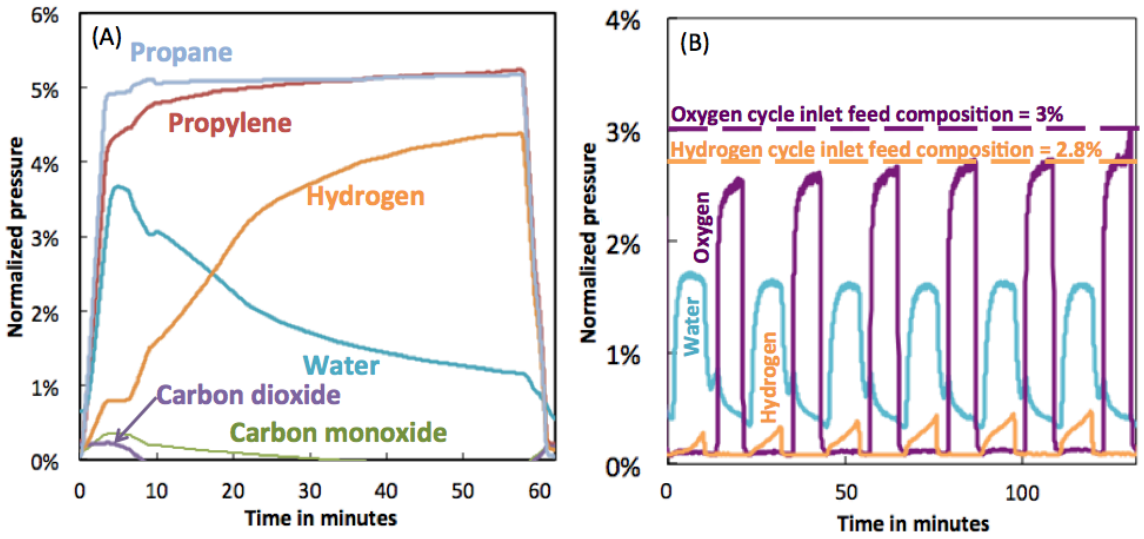

Figure 1. (A) Selective hydrogen combustion performed by Bi_2O_3/SBA-15 in the presence of propane and propylene at 500°C. Hydrogen, propane, and propylene were fed at 5%. Bi_2O_3/SBA-15 combusts >50 fold more moles of hydrogen than propane and propylene. (B) Alternating cycles of hydrogen and oxygen over Bi_2O_3/SBA-15 at 550°C. The alternatingly reducing and oxidizing environments show Bi_2O_3/SBA-15 is capable of reversibly releasing lattice oxygen (to produce water from hydrogen) and absorbing oxygen (to regenerate the bismuth oxide) over several cycles.

To test the cyclability of Bi_2O_3/SBA-15, we subjected the sample to alternatingly oxidizing and reducing conditions (10 minutes each) to investigate if activity was maintained. These results are shown in Figure 1(B). Initially, 2.8% hydrogen in argon is flowed over the oxidized bed producing water. During the first hydrogen cycle, there is some hydrogen breakthrough near the end of the cycle. Due to water adsorbing more strongly than other analytes in the mass spec, the water trace behaves with a lag-time and appreciable response time. As a consequence, one can see water exiting the reactor during argon purges and oxidative cycles as well. After the reduction cycle, oxygen is fed into the

reactor to regenerate the bismuth metal to bismuth sesquioxide. Oxygen conversion is ca. 20 % for all the oxidizing cycles. As the number of cycles increases, hydrogen conversion decreases a marginal amount from ca. 95% to 90%, showing that Bi_2O_3/SBA-15 is a selective and cyclable oxygen carrier for hydrogen combustion. These results agree well with the work of Grasselli and co-workers[1] on Bi_2O_3/SiO_2. In their work, hydrogen conversion was 90 % during the first cycle and 70% by the 120th cycle. Hydrogen conversion of 70 % is more than sufficient to perform ODH with thermodynamic equilibrium yields above 90 % at the temperature and pressures of interest (550^{o}C and 0.5 to 1.0 bar). Despite this excellent cyclability, many ascribe rapid degradation over ten or less cycles to lack of stability of oxygen carriers, Bi_2O_3-based carriers especially.[1,10,11,13,18]

6.3.2. Oxidative dehydrogenation of propane using a platinum-based dehydrogenation catalyst and Bi_2O_3/SBA-15 for selective hydrogen combustion

The platinum-based catalyst's performance is significantly improved with the addition of the oxygen carrier (see Figure 2). Without Bi_2O_3/SBA-15, the catalyst performed near equilibrium and with high selectivity with a conversion of 36 %, selectivity of 95 %, propylene yield of 34 %, which corresponds to 89% of equilibrium propylene yield. These performance metrics are similar to those in literature[19] for this type of catalyst. With the addition of Bi_2O_3/SBA-15 to the platinum-based propane dehydrogenation catalyst to form a physical mixture, both propane dehydrogenation and selective hydrogen combustion occurred within the reactor (see Figure 2 and Table 1). For the first 10 minutes, the propane conversion is very high (even above 50%), although a relatively large fraction of that conversion is converted to byproducts of carbon oxides and cracking products (methane). At the ten-minute mark, the conversion is 47 %, with 93 % selectivity, and 44 % yield, which

corresponds to 115 % of the equilibrium yield of propylene from dehydrogenation (without the oxygen carrier). Some carbon dioxide is produced initially, but overall, side reactions are minimal. After c. 30 minutes, Bi_2O_3/SBA-15 is depleted of lattice oxygen and hydrogen combustion activity stops (shown in supplementary information, Figure S1). This is indicated by falling water concentration and increasing hydrogen concentration, as less and less hydrogen is combusted to water. Once the oxygen is finally depleted, the propylene yield approaches the thermodynamic equilibrium values (in other words, the bismuth metal is inert towards the reaction stream).

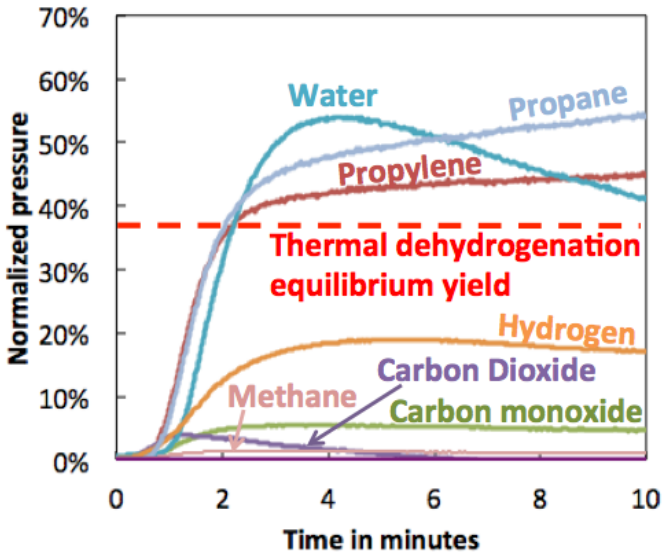

Figure 2. Oxidative dehydrogenation of propane to propylene using Bi_2O_3/SBA-15 as an oxygen source physically mixed with a platinum-based dehydrogenation catalyst. The dashed line indicates the equilibrium propylene yield of non-oxidative dehydrogenation of propane at the same temperature (550^{o}C) and pressure (0.5 bar). Yields of propylene are increased over non-oxidative dehydrogenation by the addition of selective hydrogen combustion by Bi_2O_3/SBA-15.

After 60 minutes, the reactor was purged with only argon and the reactor bed regenerated. It was regenerated in oxygen to combust any coke that may have been present on the platinum-based catalyst and to reoxidize the oxygen carrier. Subsequent propane oxidative dehydrogenation cycles did not show nearly the performance of the first cycle. In fact, the conversion was lower than the (non-oxidative) dehydrogenation catalyst by itself (shown in Figure 3). This drastic reduction in performance per cycle is similar to the previous report on this type of platinum and bismuth based ODH system. Grasselli reported a 5 % decrease in performance (propylene yield) per cycle.[4] We measure very similar numbers: normalized yield falling from 115 % to 70 % over 11 cycles, which corresponds to about a 4 % decrease in performance per cycle. These decreases are not explainable by decreasing hydrogen combustion activity, but is likely due to the oxygen carrier deactivating the catalyst for two reasons. Firstly, having lower propane conversion means the dehydrogenation catalyst was of lower activity than without the oxygen carrier. Had the platinum-based catalyst been unaffected and the oxygen carrier completely inert, the system would still achieve (non-oxidative) equilibrium yields. Consequently, the catalyst itself has less activity than without the oxygen carrier present. Secondly, the subsequent cycles had excellent hydrogen combustion activity (qualitatively similar to the first cycle, high hydrogen combustion for the first thirty minutes and negligible after 30 minutes). As a result, the hydrogen combustion activity cannot be the culprit of decreased performance because hydrogen combustion activity is still similar to the first cycle. To explain these findings, we ascribe the degradation of performance not to loss of hydrogen combustion activity as in previous reports, but rather to the bismuth-based oxygen carrier deactivating the catalyst during the reoxidation step. Furthermore, it is suggested that this deactivation is

poisoning of the dehydrogenation catalyst by bismuth, which volatilizes during oxidative regeneration (not during the dehydrogenation cycle because the system performs well at first). The quartz tube that holds the reactor bed had deposits of bismuth where the tube cooled (shown in the supplemental information, Figure S3). This effect is well know for low boiling point (typical of p-block metals) oxygen carriers in literature reports[1,8,13], although its has never been implicated in dehydrogenation catalyst deactivation.

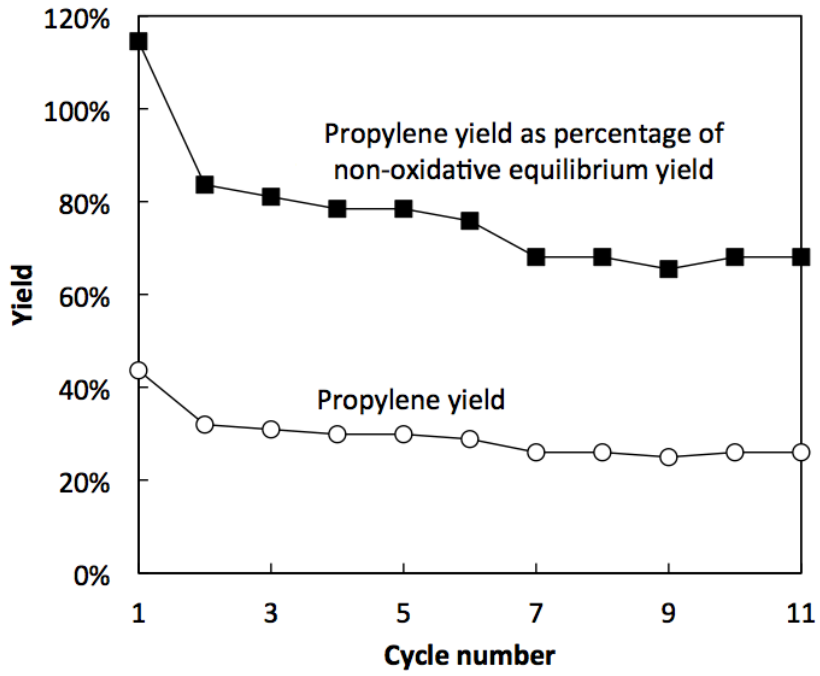

Figure 3. Propylene yield (and as a percentage of non-oxidative equilibrium yield) during repeated cycles of oxidative dehydrogenation of propane using Bi_2O_3/SBA-15 for selective hydrogen combustion and a platinum-based catalyst. The reactor bed was regenerated with oxygen to replenish the lattice oxygen in Bi_2O_3/SBA-15 consumed during hydrogen combustion. After the first cycle, the yields of propylene fall below the non-oxidative yields, indicating catalyst deactivation.

To further support the suggestion that bismuth is poisoning the dehydrogenation catalyst, XPS was performed on the dehydrogenation catalyst after the aforementioned reaction-regeneration cycling. The oxygen carrier and catalyst particles were physically mixed, but large enough (~80mesh) to differentiate from each other. Once the sample was loaded into the XPS, point of analysis (ca. 100μm x 100μm) was chosen to maximize the platinum signal. XPS of the platinum 4f and bismuth 4f regions are shown in Figure 4. These peaks correspond with platinum in various metal and oxidic moieties as would be expected after repeated oxidations and reductions (ending with an oxidation). In the Bi 4f region, the bismuth 4f peaks are not only present, but prominent. They correspond to bismuth(III) oxide, as expected from an oxidative cycle. Using atomic sensitivity factors of 2.55 for platinum and 4.25 for bismuth, the peak areas indicate there is 80% more bismuth present than platinum on the dehydrogenation catalyst particles. With such an abundance of bismuth deposited on the platinum catalyst, it is well within the realm of likelihood that some bismuth is on the platinum surface.

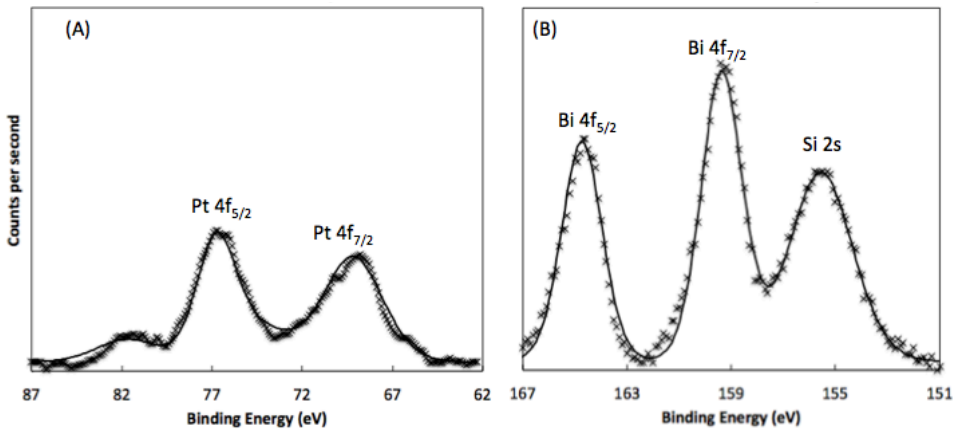

Figure 4. XPS of the platinum-based propane dehydrogenation catalyst after it was mixed with Bi_2O_3/SBA-15 and cycled between dehydrogenation of propane and regeneration with oxygen. Stars are experimentally measured data points and the line is the

summation of the synthetic peaks. Panel (A) focuses on the platinum 4f orbitals, showing binding energies characteristic of platinum metal and platinum oxides. Panel (B) focuses on the bismuth 4f peaks which are present from migration of bismuth from Bi_2O_3/SBA-15 migrating to the dehydrogenation catalyst. The binding energy of the $4f_{7/2}$ orbital corresponds to that of Bi^{3+} in Bi_2O_3. The Si 2s peak is present from the SBA-15 support.

For the reasons elaborated above, we conclude that Bi_2O_3 supported on silica is not a suitable oxygen carrier in conjunction with platinium-based dehydrogenation catalysts due to deactivation of the latter by the former. Bismuth is a known catalyst poison and was shown to be present in large amounts on the dehydrogenation catalyst; therefore, it is likely that bismuth is poisoning the active sites on the platinum, although the present work is not conclusive in this regard. In an attempt to find a more stable system, we replaced the platinum-based dehydrogenation catalyst with one based on chromium to see if the new catalyst was resistant to deactivation from bismuth and therefore more stable.

6.3.3. Oxidative dehydrogenation of propane using a chromium-based dehydrogenation catalyst and Bi_2O_3/SBA-15 for selective hydrogen combustion

Towards a stable oxidative dehydrogenation of propane system, a chromium-based catalyst was tested as a possible alternative to the quickly-deactivating platinum-based catalyst. A chromium-based catalyst was selected for its (1) propane dehydrogenation selectivity and activity, (2) occasional robustness relative to some platinum-based catalysts[5], and (3) it is well-understood for non-oxidative dehydrogenation of propane[5]. As a baseline, non-oxidative dehydrogenation was performed using this chromium-based catalyst. It achieved a conversion of 33 %, selectivity of 91 %, and a propylene yield of 30 %, which corresponds to 79 % of the maximum equilibrium propylene yield. These performance

metrics compare favorably to literature[19] for this type of catalyst. Subsequently, fresh catalyst was mixed with Bi_2O_3/SBA-15 to perform oxidative dehydrogenation of propane. Surprisingly, the chromium-based catalyst's performance (as measured by propylene yield) is not appreciably affected by the addition of the oxygen carrier and the hydrogen combustion it provides. The oxidative dehydrogenation system converts 38 % of propane at 89 % selectivity to produce propylene at 34 % yield, which corresponds to 89% of the yield determined by non-oxidative dehydrogenation equilibrium (see Figure 5 and Table 1). By-products include methane (~4 % of propane), carbon dioxide (2 %), carbon monoxide (2 %) and coke (2 %). These metrics are all within 5 % of without the oxygen carrier. Peculiarly, the hydrogen has been combusted (with normalized pressures of hydrogen less than 10%), but the propylene production has not been improved (shown for a longer time span in the supplementary information, Figure S2). One explanation for this phenomenon is that the water produced by selective hydrogen combustion is deactivating the dehydrogenation catalyst. If this were the case, the front of the reaction bed would be filled with active catalyst, which would produce propylene and hydrogen, but the later stages of the bed would be catalytically inactive from the presence of water produced via combustion. Indeed, propylene and water are the majority products, indicating the oxygen carrier is active. To further confirm his hypothesis, the effects of steam-diluted dehydrogenation over the chromium-based catalyst were investigated.

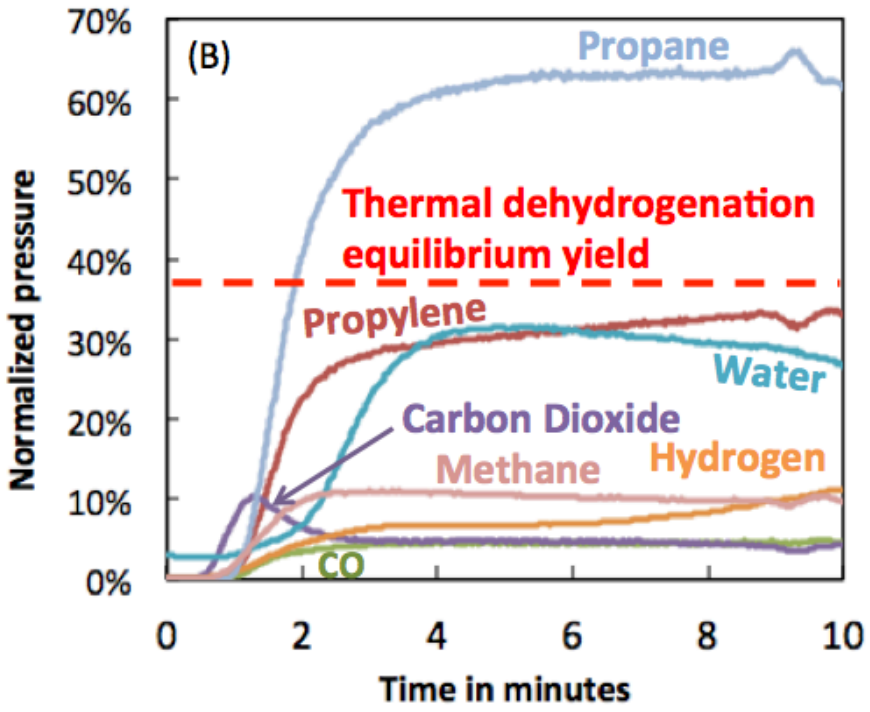

Figure 5. Oxidative dehydrogenation of propane to propylene using Bi_2O_3/SBA-15 as an oxygen source physically mixed with a chromium-based catalyst. The dashed line indicates the equilibrium propylene yield of non-oxidative dehydrogenation of propane at the same temperature (550^{o}C) and pressure (0.5 bar). Yields of propylene are increased by the addition of Bi_2O_3/SBA-15, although hydrogen combustion is active and selective.

To understand the effects of steam (usually produced *in situ* during hydrogen combustion) on the chromium-based dehydrogenation catalyst, a simulated mixture of ODH products, steam and propane with an argon carrier, were flowed over the catalyst in the absence of any hydrogen combusting oxygen carrier. Although the catalyst initially produces up to 6 % propylene, the catalyst activity quickly dies (after ca. 2 minutes) and propane flows through the reactor bed unreacted (see Figure 6 and Table 1). This is likely

due to strong hydroxylation of the surface and bulk of the chromium oxide. By integrating the missing water peak, we calculate the catalyst absorbs a significant amount of water: 60 mol% of the chromium. This is quite consistent with well-studied bulk hydroxide phases. Because of the deactivation caused by steam, the chromium-based catalyst is fundamentally incompatible with selective hydrogen combustion. To our knowledge, this measurement has not been previously reported, despite being suggested over eleven times. Operando measurements, such as *in situ* XRD or DRIFTS, could provide valuable insight in to the deactivation mechanism and the role played by water, surface hydroxyls, and bulk phase change.

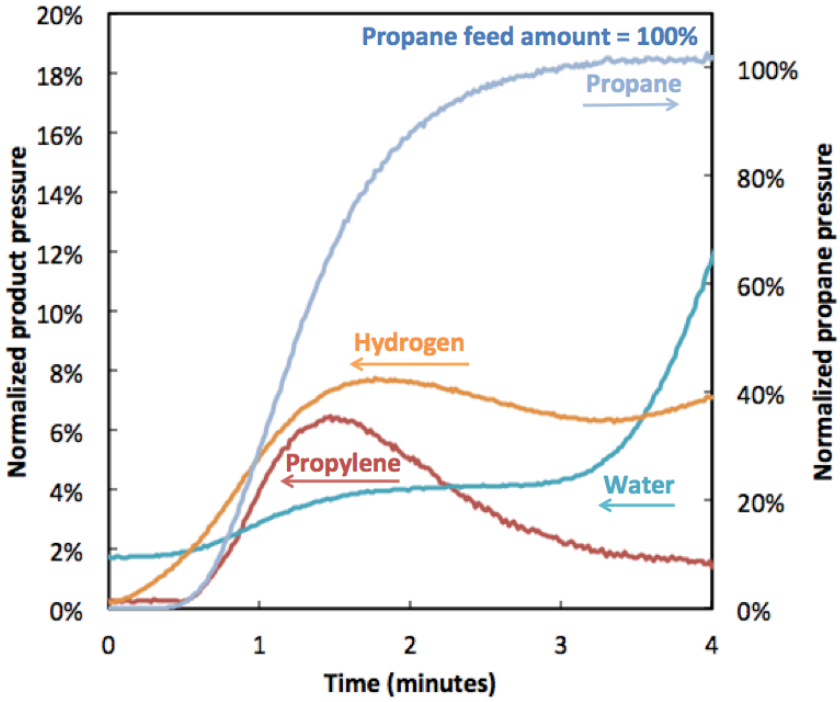

Figure 6. Non-oxidative dehydrogenation of propane to propylene in the presence of steam using a chromium-based catalyst at 500°C. Steam (fed at 40% of argon) quickly deactivates the catalyst resulting in negligible propylene production.

Table 1. Reaction metrics of non-oxidative (without Bi_2O_3/SBA-15) and oxidative (with Bi_2O_3/SBA-15) dehydrogenation of propane using either a platinum- or chromium- based catalyst. Additionally, steam-diluted dehydrogenation of propane was conducted by the introduction of 40% water to the feed. All metrics were recorded after 10 minutes on stream with fresh catalyst and Bi_2O_3/SBA-15.

Reaction	Catalyst type	Propane Conversion	Propylene Selectivity	Propylene Yield	Percent of equilibrium dehydrogenation yield
Dehydrogenation	Chromium	33%	91%	30%	79%
	Platinum	36%	95%	34%	89%
Oxidative dehydrogenation	Chromium	38%	89%	34%	89%
	Platinum	47%	93%	44%	115%
Steam-diluted dehydrogenation	Chromium	0%	N/A	0%	0%

6.4. Conclusions

Combining a selective hydrogen combustion oxygen carrier with a traditional dehydrogenation catalyst has been proposed as a promising scheme for oxidative dehydrogenation of propane. In this work, we synthesized bismuth(III) oxide on mesoporous silica (Bi_2O_3/SBA-15) and showed that it is active and selective for hydrogen combustion. Furthermore, it can be regenerated with oxygen with little degradation in activity. We then combined this solid reactant with two common dehydrogenation catalysts, one based on platinum and another based on chromium. Combining Bi_2O_3/SBA-15 with the platinum-based catalyst increased propylene yields from 89% to 119% of the non-oxidative dehydrogenation equilibrium. The platinum-based catalyst combined with the bismuth-based oxygen carrier quickly degrades in performance after alternating cycles of dehydrogenation

and regeneration. Combining Bi_2O_3/SBA-15 with the chromium-based catalyst did not appreciably improve performance. Further studies with steam-diluted propane dehydrogenation showed water (either directly fed or produced from selective hydrogen combustion) deactivated the chromium-based catalyst. Bi_2O_3 supported on silica is not a suitable oxygen carrier in conjunction with platinium-based dehydrogenation catalysts due to deactivation of the latter by the former. With this understanding in mind, future work on implementing ODH with selective hydrogen combustion must include studies on compatibility between the hydrogen combusting oxygen carrier and the dehydrogenation catalyst, as each can be cyclically stable on their own, but not in conjunction with one another. Water (and consequently, selective hydrogen combustion), is incompatible with chromium-based dehydrogenation catalysts because of water-induced deactivation. Future studies on chromium-based ODH should include studies of deactivation by water, which can, perhaps, be avoided through a novel use of promoters or another protective means.

6.5. Acknowledgements

This work was supported by the Department of Energy, Office of Science, Office of Basic Energy Sciences DE-FG03-89ER14048

6.6. Supplemental information

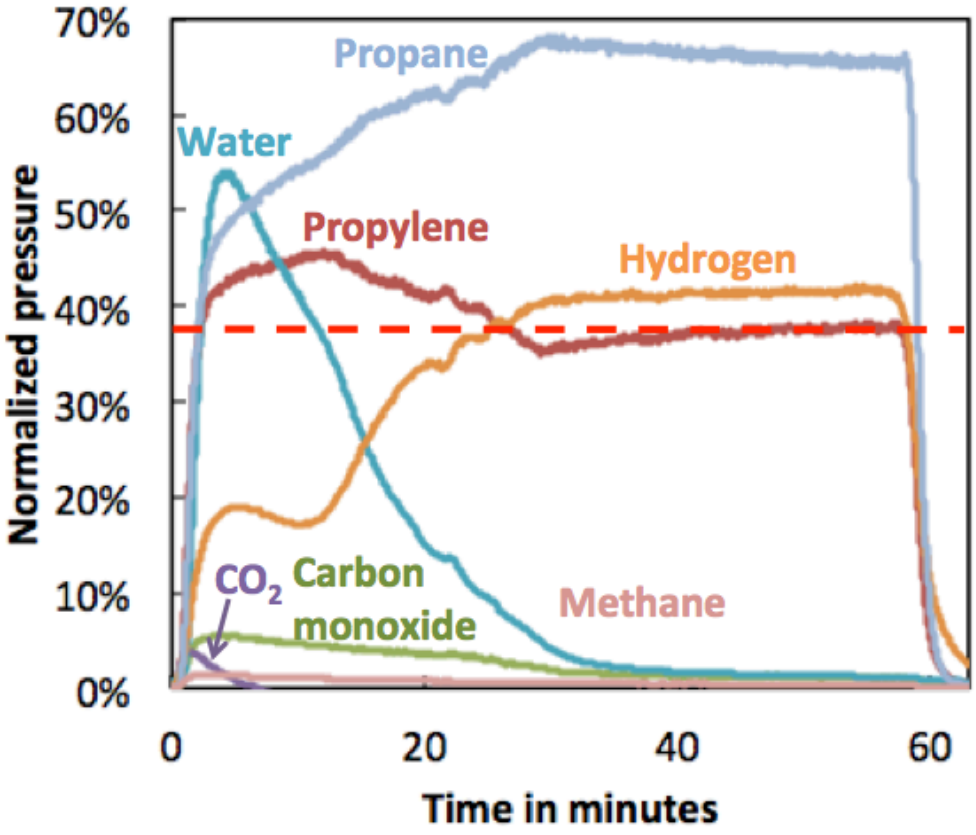

Figure S1. Oxidative dehydrogenation of propane to propylene using Bi_2O_3/SBA-15 as an oxygen source physically mixed with a platinum-based dehydrogenation catalyst. The dashed line indicates the equilibrium propylene yield of non-oxidative dehydrogenation of propane at the same temperature (550^{o}C) and pressure (0.5 bar). Yields of propylene are increased over non-oxidative dehydrogenation by the addition of selective hydrogen combustion using Bi_2O_3/SBA-15 until the 25-minute mark when the lattice oxygen is depleted from Bi_2O_3/SBA-15, after which only the dehydrogenation catalyst is active.

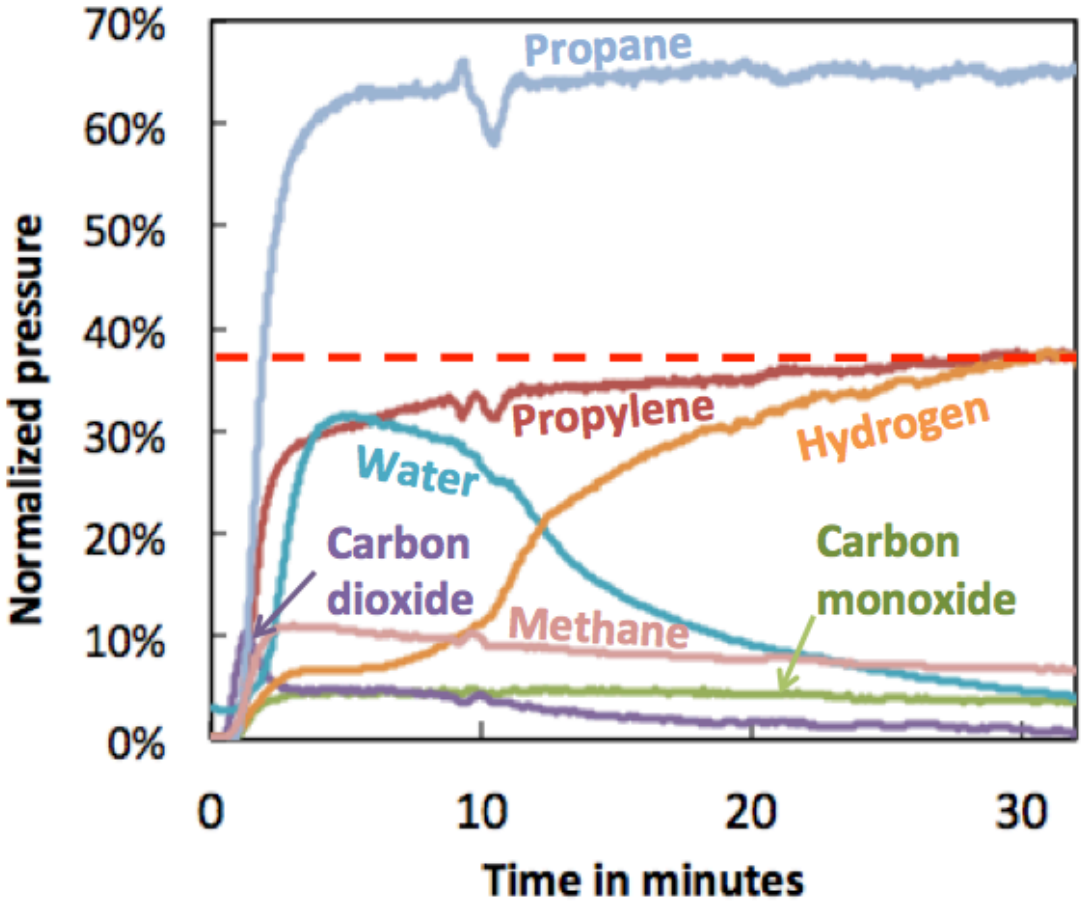

Figure S2. Oxidative dehydrogenation of propane to propylene using Bi_2O_3/SBA-15 as an oxygen source physically mixed with a chromium-based dehydrogenation catalyst. The dashed line indicates the equilibrium propylene yield of non-oxidative dehydrogenation of propane at the same temperature (550^{o}C) and pressure (0.5 bar). For the first 15 minutes while lattice oxygen in Bi_2O_3/SBA-15 is available, hydrogen produced by dehydrogenation is converted to water, although yields of propylene remain similar to without the addition of Bi_2O_3/SBA-15.

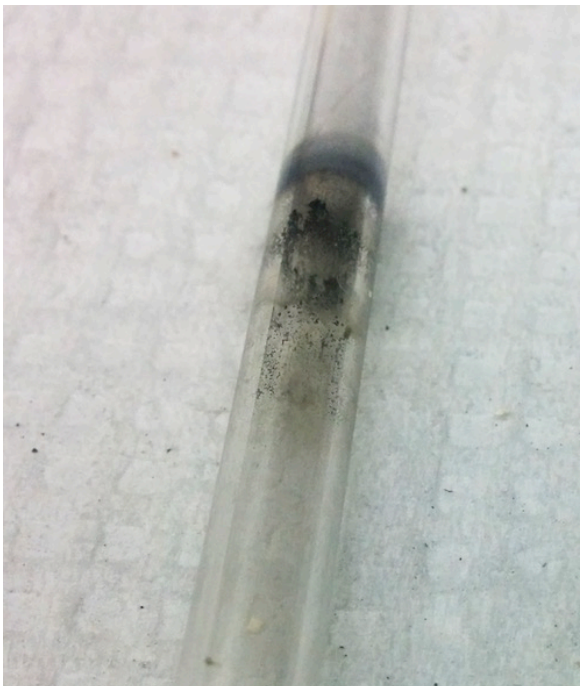

Figure S3. Bismuth metal deposited downstream of the reactor bed after repeated oxidative dehydrogenation cycles over platinum-based catalyst physically mixed with Bi_2O_3/SBA-15 at 550^{o}C.

6.7. References

1. Grasselli, R. K., Stern, D. L. & Tsikoyiannis, J. G. Catalytic dehydrogenation (DH) of light paraffins combined with selective hydrogen combustion (SHC) II. DH + SHC catalysts physically mixed (redox process mode). *Appl. Catal. A Gen.* **189,** 9–14 (1999).

2. Collins, J. P., Schwartz, R. W., Hagen, G. P. & Udovich, C. A. Catalytic Dehydrogenation of Propane in Hydrogen Permselective Membrane Reactors. **5885,** 4398–4405 (1996).

3. Grasselli, R., Stern, D. & Tsikoyiannis, J. Catalytic dehydrogenation (DH) of light paraffins combined with selective hydrogen combustion (SHC): I. DH -> SHC -> DH catalysts in series (co-fed process mode). *Appl. Catal. A Gen.* **189,** 1–8 (1999).

4. Tsikoyiannis, J. G., Stern, D. L. & Grasselli, R. K. Metal Oxides As Selective Hydrogen Combustion (SHC) Catalysts and Their Potential in Light Paraffin Dehydrogenation. *J. Catal.* **184,** 77–86 (1999).

5. Bhasin, M., McCain, J. & Vora, B. Dehydrogenation and oxydehydrogenation of paraffins to olefins. *Appl. Catal. A …* **221,** 397–419 (2001).

6. Beckers, J. & Rothenberg, G. Ce0.95Cr0.05O2 and Ce0.97Cu0.03O2: active, selective and stable catalysts for selective hydrogen combustion. *Dalton Trans.* 5673–82 (2009). doi:10.1039/b904681j

7. Beckers, J., Lee, A. F. & Rothenberg, G. Bismuth-Doped Ceria, Ce0.90Bi0.10O2: A Selective and Stable Catalyst for Clean Hydrogen Combustion. *Adv. Synth. Catal.* **351,** 1557–1566 (2009).

8. Blank, J. H., Beckers, J., Collignon, P. F. & Rothenberg, G. Redox kinetics of ceria-based mixed oxides in selective hydrogen combustion. *Chemphyschem* **8,** 2490–7 (2007).

9. Blank, J. H., Beckers, J., Collignon, P. F., Clerc, F. & Rothenberg, G. A 'green route' to propene through selective hydrogen oxidation. *Chemistry* **13,** 5121–8 (2007).

10. Beckers, J., Clerc, F., Blank, J. H. & Rothenberg, G. Selective Hydrogen Oxidation Catalysts via Genetic Algorithms. *Adv. Synth. Catal.* **350,** 2237–2249 (2008).

11. Beckers, J. & Rothenberg, G. Lead-containing solid 'oxygen reservoirs' for selective hydrogen combustion. *Green Chem.* **11,** 1550 (2009).

12. Beckers, J. & Rothenberg, G. Redox properties of doped and supported copper-ceria catalysts. *Dalton Trans.* 6573–8 (2008). doi:10.1039/b809769k

13. Gómez-Quero, S., Hernández-Mejía, C., Hendrikx, R. & Rothenberg, G. Understanding the redox behaviour of PbCrO4 and its application in selective hydrogen combustion. *Dalton Trans.* **41,** 12289–95 (2012).

14. Beckers, J., Drost, R., van Zandvoort, I., Collignon, P. F. & Rothenberg, G. Selective hydrogen oxidation in the presence of C3 hydrocarbons using perovskite oxygen reservoirs. *Chemphyschem* **9,** 1062–8 (2008).

15. Zhao, D. *et al.* Triblock copolymer syntheses of mesoporous silica with periodic 50 to 300 angstrom pores. *Science* **279,** 548–52 (1998).

16. Yokoyama, C., Bharadwaj, S. S. & Schmidt, L. D. Platinum-tin and platinum-copper catalysts for autothermal oxidative dehydrogenation of ethane to ethylene. *Catal. Letters* **38,** 181–188 (1996).

17. Weckhuysen, B. M. & Schoonheydt, R. a. Alkane dehydrogenation over supported chromium oxide catalysts. *Catal. Today* **51,** 223–232 (1999).

18. Van der Zande, L. M. (Lars), de Graaf, E. A. (Bart) & Rothenberg, G. Design and Parallel Synthesis of Novel Selective Hydrogen Oxidation Catalysts and their Application in Alkane Dehydrogenation. *Adv. Synth. Catal.* **344,** 884–889 (2002).

19. Dehydrogenation, N., Marie, V. & Herauville, T. Catalytic Dehydrogenation of Propane. (2012).

Appendix A: Hydrodebromination and Oligomerization of Dibromomethane

Methane is an abundant and potentially renewable hydrocarbon resource. Unlike petroleum, which is a liquid and relatively easy to collect remotely and transport, methane is challenging to cost-effectively collect and transport over long distances, and is frequently flared. Conversion of methane gas into a more readily transportable liquid, Gas-To-Liquid (GTL), at the site of collection has long been thought to be the ideal solution.[1−4] Several methods have been developed for the direct conversion of methane,[5] including oxidative coupling,[6,7] aromatization,[8] and selective oxidation into methanol,[9,10] but the yields have not been adequate for commercial deployment. Commercial GTL technology relies on breaking all the C−H bonds in methane in the presence of an oxygen source to produce synthesis gas, CO + H_2, as a transformable intermediate. The synthesis gas can then be used for the Fischer−Tropsch (F-T) synthesis to produce liquid fuels and chemicals. Another route is using synthesis gas for the synthesis of CH_3OH, which is used as a reactant in the Methanol-To- Gasoline process for the synthesis of liquid fuels and chemicals.[2,3] To produce economically competitive products, large commercial facilities are required for GTL conversion processes because of the cost of production (with conversion temperatures usually over 800 °C) of the synthesis-gas intermediate from methane.

A low-temperature, high-yield process with a smaller facility that could be located close to the natural gas sources is highly desirable. From this point of view, the methane halogenation process is promising. The halogen-mediated routes for con- version of methane to higher hydrocarbons are illustrated in Figure 1A. Instead of the high energy-consuming synthesis gas process, methane can be nonselectively converted to halomethanes ($CH_{4-n}X_n$)

at relatively low temperatures (below 550 °C).[11−13] Methyl halides such as CH_3Br have been shown to be directly transformed into olefins or higher hydrocarbons by a coupling process analogous to the Methanol-To-Olefins and Methanol- To-Gasoline processes over either zeolites[14−17] or bifunctional acid−base metal oxides.[18] Of the halogens, bromine has the advantage that selectivity for the formation of methyl bromide from the direct reaction of bromine with methane is relatively high; and, the C−Br bond is weak enough to allow for facile bromine removal and recovery for reuse.[11,17] However, the bromination of methane at high conversion also produces significant quantities of dibromomethane (DBM), with small amounts of tribromomethane. In general, the halogenation reaction rate increases in the order: $CH_4 < CH_3X < CH_2X_2 < CHX_3$,[11,12] with polyhalogenation being especially kinetically favored for Cl and F. Because of the reactivity of the poly- halogenated species, catalytic processes for converting these methane halogenation products to end-products have typically resulted in coke formation.19 Separation of these polyhalomethanes prior to their use in the coupling reactor makes the entire halogen- based GTL process substantially more expensive and less practical.

Several strategies can be applied to solve the polyhalomethane issue. The first is selective halogenations. Olah et al.[11] proposed that since incorporation of halogen atoms into me- thane makes the carbon progressively more electropositive, the electrophilic reaction with $X^{\delta+}$, which is produced by super- electrophiles, becomes kinetically less favorable. Thereby high methyl halide selectivities could, in principle, be achieved.

Following a similar philosophy, Lercher et al.[13] studied methane oxychlorination on LaOCl. Although the underlying rationale is sound, there are no reports of high-yield catalytic selective monohalogenation on the catalysts with long-term stability. Another

Approach is converting the polyhalomethanes into other chemicals with lower coking tendencies, which can be fed into the coupling reactor. Using the polybromomethanes as the halogenating agent for methane has been studied.[12] Although thermodynamically favored, the production of two molecules of methyl bromide from the reaction of DBM and methane requires a relatively long space time. Furthermore, the selectivity of the methyl bromide is limited by thermodynamics. Another approach is to separate the poly halomethanes from the stream and make use of these compounds to produce value-added chemicals.

Hydrodehalogenation is regarded as the most universal and effective method for the treatment and chemical destruction of organohalide compounds.[20,21] We have been motivated by the catalytic processes used commercially for this important reaction. Group VIII metals are the best known catalysts for hydro-dehalogenation because of the ability to dissociate C−X and H−H bonds as well as the high stability.20−25 In this paper we report our results on the catalytic hydrodebromination and oligomerization of DBM, which is the major byproduct from the reaction of methane and bromine. Among the catalysts studied (Ru/SiO_2, Rh/SiO_2, Pd/SiO_2, Pt/SiO_2, Ag/SiO_2, and Au/SiO_2), palladium carbide formed during the reaction on Pd/SiO_2 showed the highest activity and highest selectivity for coupling products. C_{2+} formation can be regarded as the F-T synthesis analogue. Ru/ SiO_2 showed the highest selectivity for methyl bromide, and can be regarded as a methanol synthesis catalyst analogue. Detailed reaction mechanisms are discussed. The analogous nature of halogen and oxygen mediated pathways for the conversion of methane to higher hydrocarbons is illustrated in Figure 1B.

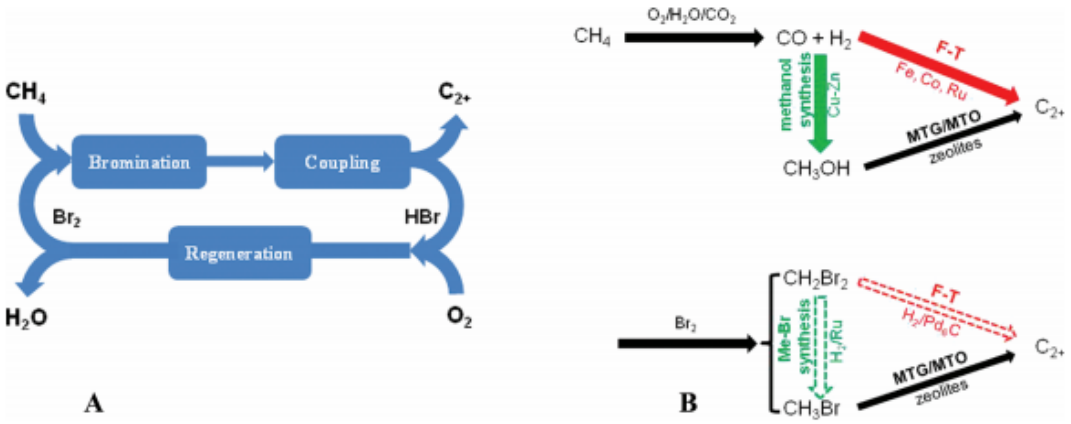

Figure 1. (A) Illustration of halogen mediated methane conversion to higher hydrocarbons; (B) The analogous nature of halogen routes to oxygen routes for methane upgrading. Dashed arrows denote the processes developed in this work.

Since propane is a major byproduct in the Methyl Bromide To-Gasoline process, we intend to make use of propane to provide H_2 for the hydrodebromination process. One possibility is integrating a propane steam reforming unit. Another alternative is adding a propane dehydrogenation unit to provide H_2; meanwhile, more olefin (propylene) will be produced, which is helpful for the Methyl Bromide-To-Gasoline process. Our findings in this paper are directed at solving the DBM issue that hinders the potential industrial application of bromine mediated GTL technology, and at the same time offering a new route for the synthesis of light olefins.

Results and Discussion

All the catalysts were prepared into 1 wt % (metal basis) by incipient impregnation, followed by a calcination and activation process before the hydrodebromination reaction. The hydrodebromination reactions were conducted in an atmospheric pressure fixed bed flow reactor system; the configuration of the reaction system was shown in Figure 2.

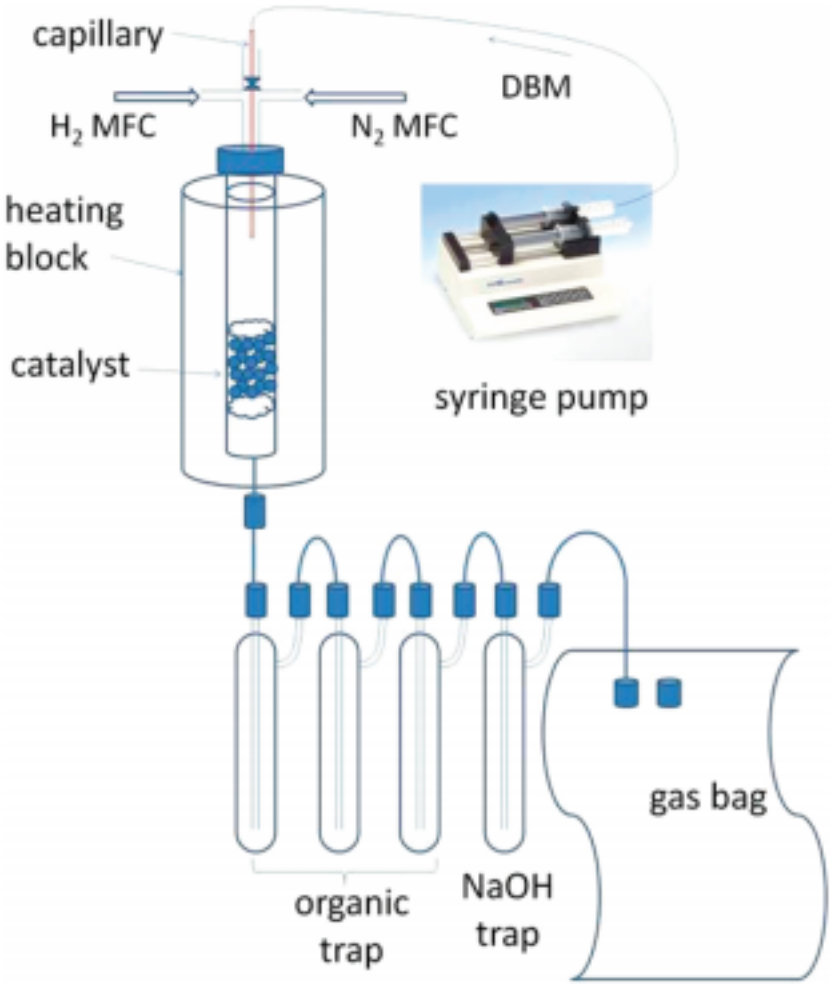

Figure 2. Experimental setup for hydrodebromination reaction: CH2Br2 + H_2 → products.

After the DBM hydrodebromination reaction was run for 30 min at 350 °C, no significant change was observed in the Ru/SiO_2, Rh/SiO_2, Pt/SiO_2, and Au/SiO_2 structures by X-ray diffraction (XRD); however, for the Ag/SiO_2 catalyst, a transformation of the Ag metallic phase into an AgBr phase was observed. For Pd/SiO_2, all the diffraction peaks shifted to lower angles. This behavior can be attributed to the formation of Pd_6C phase, which is very common for Pd catalysts in contact with many hydrocarbons.[26] The Pd-to-Pd_6C phase transformation during hydrodechlorination has been identified by other

researchers.[27] After a detailed study of this phase transformation process, we found that the Pd-to-Pd_6C transformation was complete in less than 90 s, while recovery of the metallic Pd in hydrogen, after the DBM was removed, required approximately 30 min, Figure 3A. This indicates that palladium was mainly in the form of Pd_6C during the DBM hydrodebromination reaction instead of metallic Pd.

The conversions of DBM from the reaction with hydrogen at 350 °C on Ru/SiO_2 , Rh/SiO_2, Pd_6C $/SiO_2$, Pt/SiO_2, Ag/SiO_2, and Au/SiO_2 are shown in Figure 3B. The conversions followed approximately the following order: Au/SiO_2, $Ag/SiO_2 \ll Ru/SiO_2 < Rh/SiO_2 \approx Pt/SiO_2 < Pd_6C/SiO_2$.

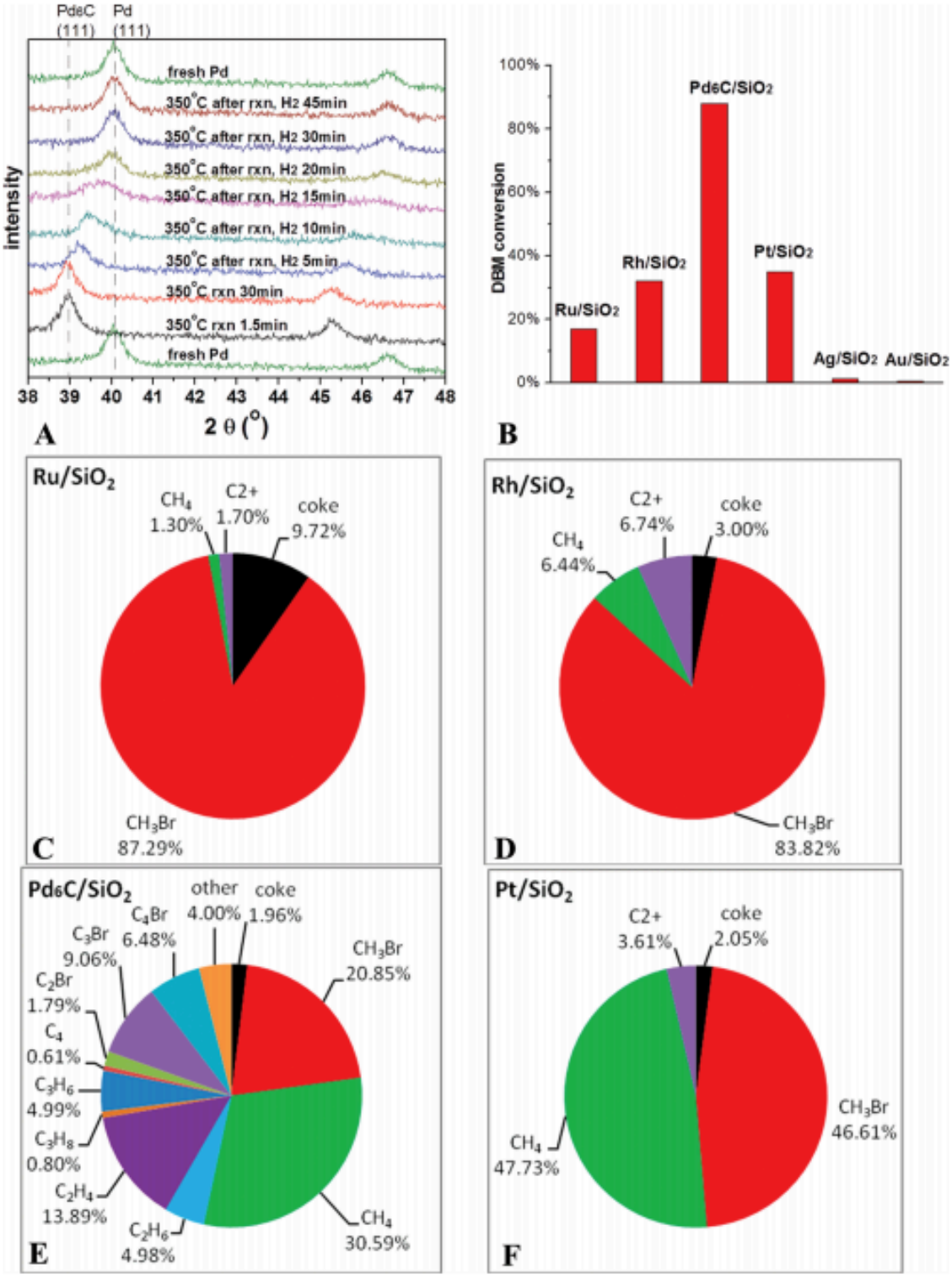

Figure 3. (A) X-ray diffraction patterns of Pd/SiO_2 catalyst after different treatment. The two peaks centered at 2θ = 39° and 40.1° can be assigned to Pd_6C(111) and Pd(111)

reflection, respectively; "rxn" denotes DBM hydrodebromination reaction under following condition: 350 °C, τ =2s (residence time), DBM:H_2 :N_2 mole ratio of 7:14:40; After reaction, the catalysts were treated with H_2 :N_2 (14 sccm:40 sccm) at 350 °C for a different period of time. (B) The conversion and (C to F) product distribution of dibromomethane when reacted with hydrogen over different metal catalysts supported on silica: (C) Ru/SiO_2 ; (D) Rh/SiO_2 ; (E) Pd_6C /SiO_2 , and (F) Pt/SiO_2 (Reaction conditions: 350 °C, τ = 2s, DBM:H_2 :N_2 mole ratio of 7:14:40, DBM total input of 8.32 mmol, product distributions are calculated based on carbon moles.).

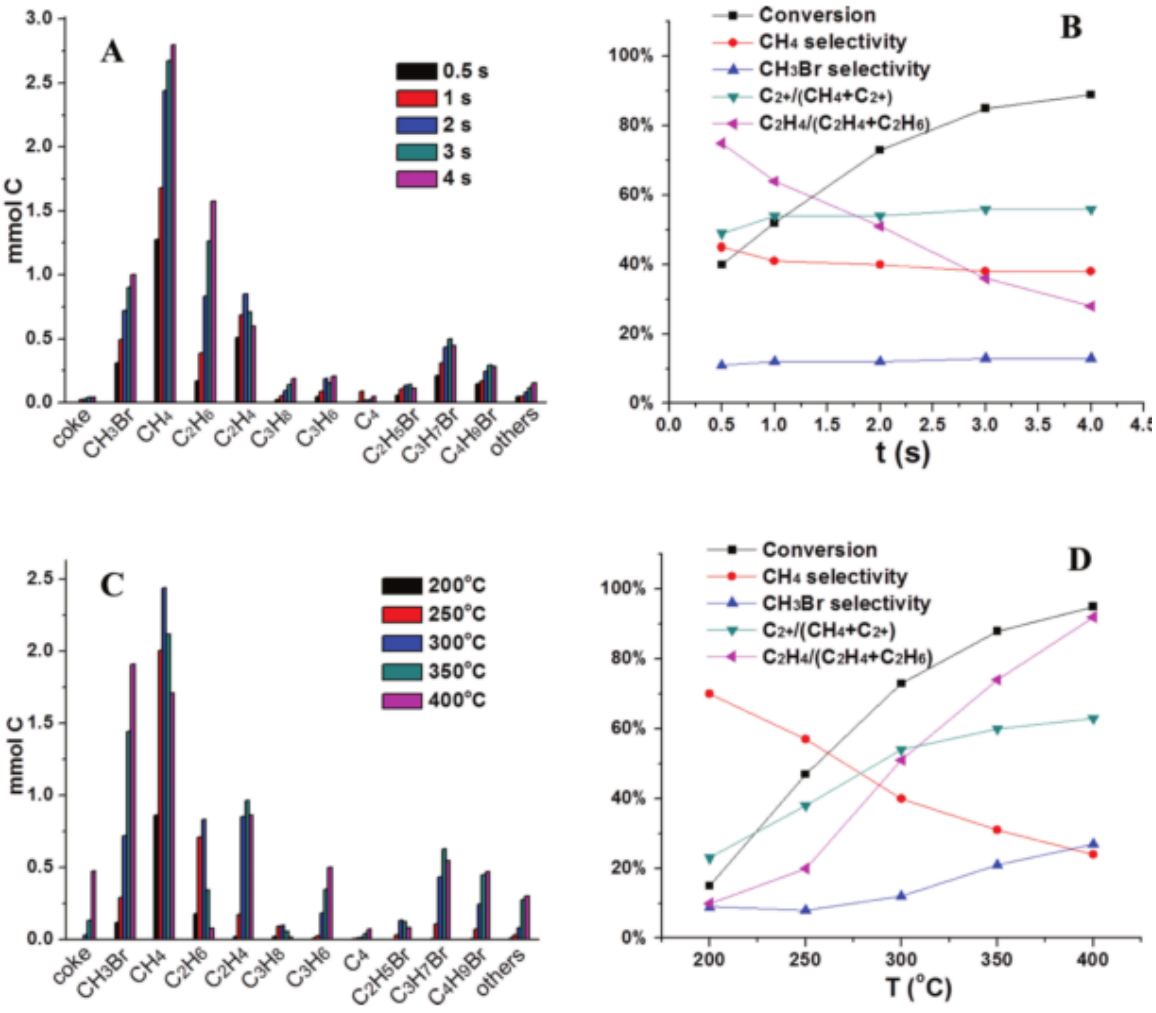

Figure 4. Residence-time-dependent (A and B) and temperature-dependent (C and D) dibromomethane reaction with hydrogen over Pd_6C /SiO_2 catalyst. (A and C) product distribution; (B and D) conversion, CH_4 selectivity, CH_3Br selectivity, C_{2+} /(CH4 +C_{2+}) ratio andC_2H_4 /(C_2H_4 +C_2H_6) ratio. All these species were calculated in carbon mole, C_{2+} =2nC_2 +3nC_3 +4nC_4 +5nC_5, nC_n = nC_nH_{2n+2} + nC_nH_{2n} + nC_nBr (Reaction conditions: (A and B) 300 °C, DBM:H_2:N_2 mole ratio of 7:14:40, DBM total input of 8.32 mmol; (C and D) τ =2s, DBM:H_2:N_2 mole ratio of 7:14:40, DBM total input of 8.32 mmol.).

Since the DBM conversions are determined by many factors, here we are not trying to quantitatively correlate the conversions to the catalytic activities. Ag/SiO_2 and Au/SiO_2 were observed to be relatively inactive for DBM hydrodebromination. These findings are consistent with results reported by other researchers who showed that Ag and Au were inactive for hydrodechlorination reactions.[28,29] The low activity observed for Ag/SiO_2 is explained by the rapid oxidation of Ag to AgBr, which cannot dissociate H_2.[28] Au/SiO_2 was also observed to be relatively inactive and although $AuBr_x$ may not form, dissociation of molecular hydrogen on Au is not facilitated.[29]

Scheme 1. (A) Potential Pathway for Dibromomethane Reaction with Hydrogen, and (B) Evolution of Surface Carbene over Pd_6C catalyst[a]

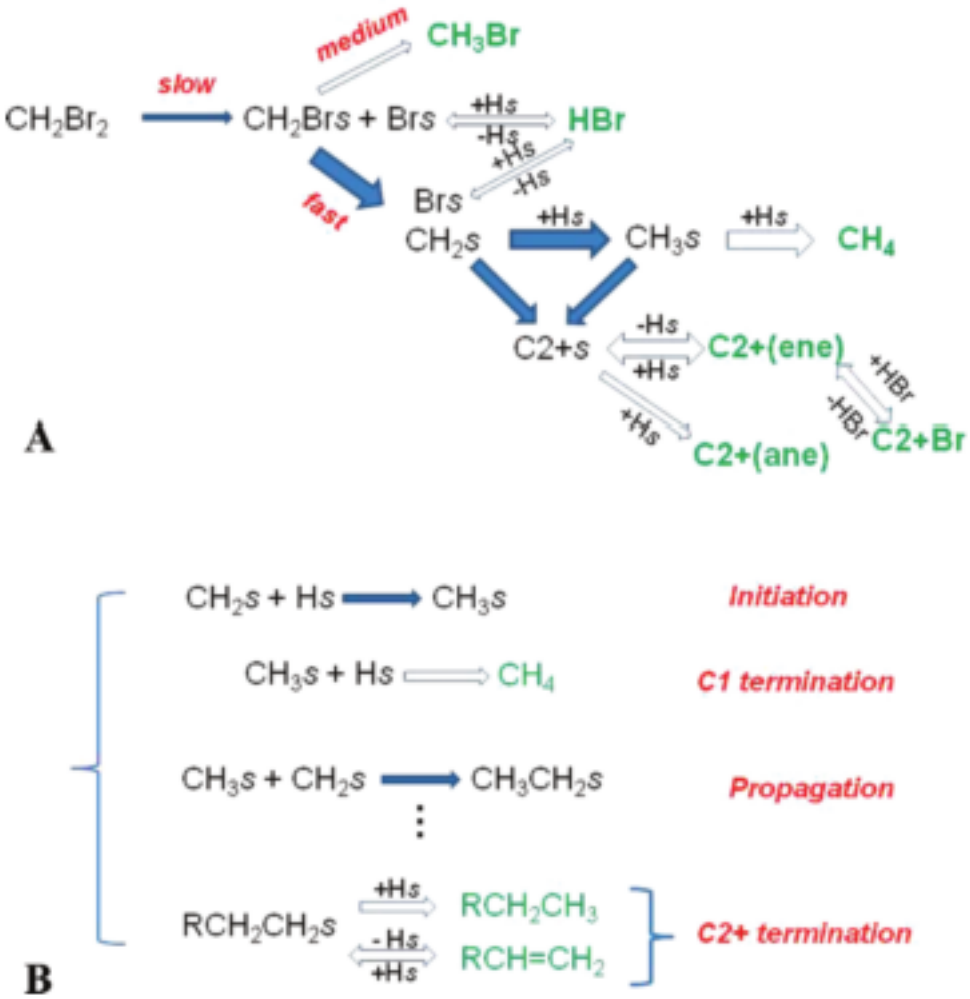

"Solid arrows indicates adsorption process or surface reaction, hollow arrows indicates desorption process or gas phase reaction. "*s*" denotes surface.

We show later in this article that the product distributions from hydrodebromination of DBM over Pd_6C catalyst are independent of the DBM conversions. Similar behavior also exists for the Ru catalyst. This allows us to compare the product distributions from Pd_6C and Ru with those from Rh and Pt, which possess similar DBM conversions (DBM conversion of 32% and 35% for Rh and Pt). The product distributions from hydrodebromination of DBM over Ru, Rh, Pd_6C, and Pt are shown in Figure 3, C to F. Extremely high methyl bromide selectivity was obtained over Ru, and only trace amounts of methane were observed. For Rh, methyl bromide was still the dominant product (more than 80%);

however, methane selectivity increased to approximately 6%. Interestingly, we observed coupling products (C_{2+}) containing up to four carbon atoms. 47% methyl bromide selectivity and 48% methane selectivity were obtained over Pt, while only trace amounts of C_{2+} were observed. DBM hydrodebromination on Pd_6C resulted in production of both methane and coupling products as the major products, while methyl bromide production was greatly suppressed.

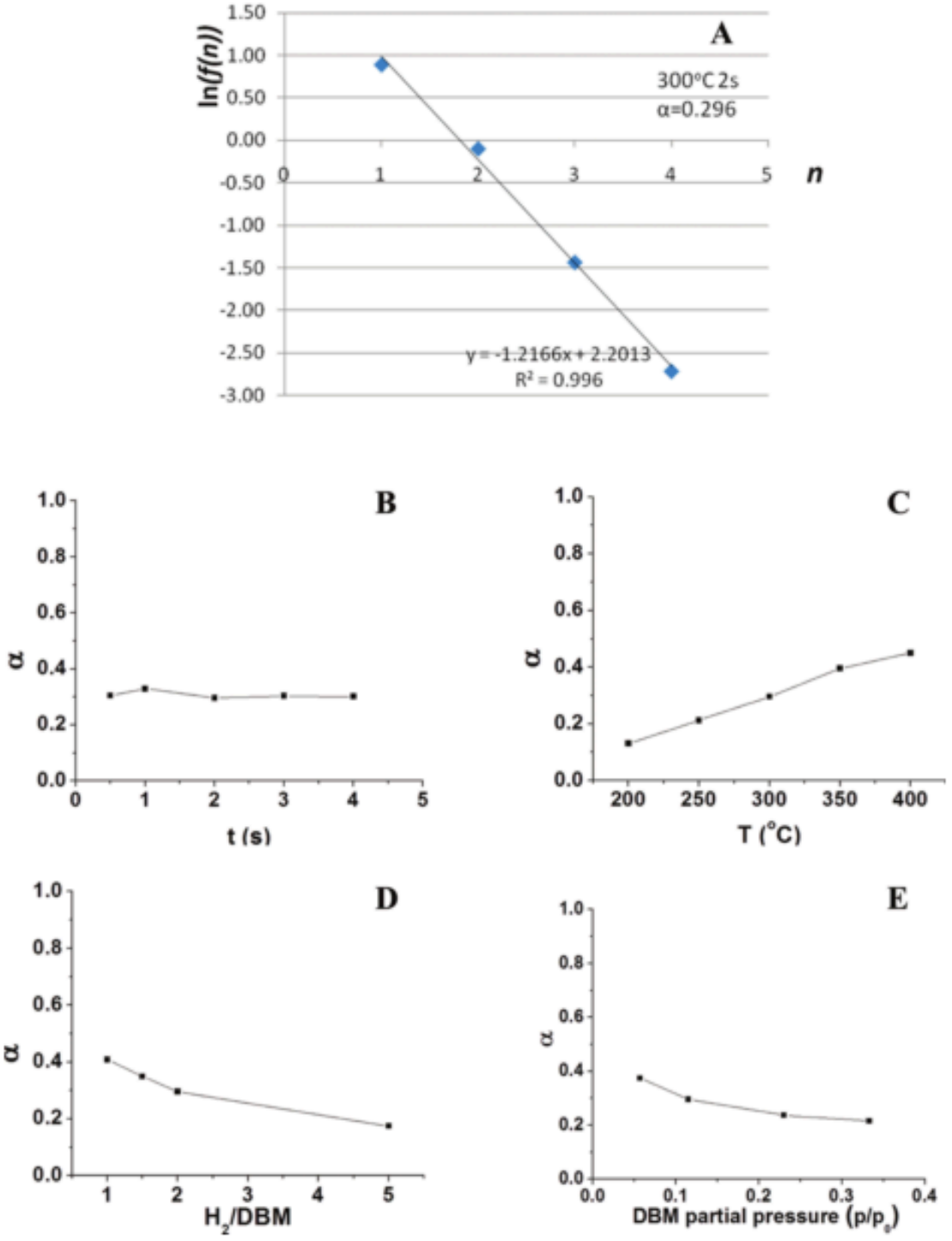

Figure 5. (A) Anderson−Schulz−Flory plotting of the product distribution of dibromomethane reaction with hydrogen over Pd_6C catalyst (300 °C, τ = 2s, DBM:H2:N_2 mole ratio of 7:14:40, DBM total input of 8.32 mmol). (B to E) Plotting of α values against

different reaction parameters (B) residence time (300 °C, DBM:H2:N_2 mole ratio of 7:14:40, DBM total input of 8.32 mmol); (C) temperature (τ = 2s, DBM:H2:N_2 mole ratio of 7:14:40, DBM total input of 8.32 mmol); (D) H2:DBM ratio (300 °C, τ = 2s, DBM total input of 8.32 mmol); (E) DBM partial pressure (300 °C, τ = 2s, DBM:H2 mole ratio of 1:2, DBM total input of 8.32 mmol).

Experiments[24] and DFT calculations[30,31] have shown that the halogen and hydrogen adsorption energy on different metal surfaces decreased in the order Ru > Rh > Pt. Stronger adsorption of Br and H on catalyst surfaces makes the HBr desorption process harder and thus leads to higher Br surface coverage. Consequently, the probability for the adsorbed CH_2Br species to desorb without losing another Br, in other words the selectivity toward CH_3Br, will be increased because of the blockage of surface adsorption sites. When we co-fed HBr with DBM-H_2 over Ru and Pt catalysts and kept all the other conditions identical with those shown in Figure 3, B to F, CH_3Br selectivity on Ru increased to 96%, while CH_4, coke, and C_{2+} formation were all suppressed. On Pt, HBr co-feeding led to similar results: CH_3Br selectivity increased to 56%, CH_4 selectivity decreased to 43%, coke and C_{2+} formation were suppressed. A discussion of C_{2+} formation over these catalysts is given later in this paper.

Balancing the price and performance of the Group VIII noble metals, Pd_6C and Ru are promising catalyst candidates for DBM hydrodebromination. Pd_6C showed the highest hydrodebromination activity and C_{2+} products selectivity, while Ru showed the highest CH3Br selectivity. Preliminary and incomplete optimization led to 60% conversion of DBM on Ru catalyst with a CH_3Br selectivity of above 96%. A time-onstream reaction was carried

out to test the durability of the Pd_6C/SiO_2 catalyst. Both conversion and selectivity were unchanged after 5 h on stream.

Detailed studies of DBM hydrodebromination were carried out over Pd_6C/SiO_2 catalyst. The following reaction parameters were studied: residence time, temperature, H_2/DBM ratio, and partial pressure. As shown in Figure 4, A and B, the DBM conversion increased with increasing residence time, while the product distribution stayed the same except that the C_2H_4 /(C_2H_4 + C_2H_6) ratio dropped. Compared to C_3 and C_4 olefins, the addition of HBr to ethylene is much slower,[32] which explained the following trend in Figure 4: $C_2Br/C_2 \ll C_3Br/C_3 < C_4Br/C_4$. In a control experiment, we used "NaOH aqueous solution + organic solution" biphase traps instead of the organic traps to collect the products, and the formation of alkyl bromides was greatly suppressed. This clearly indicates that most of the alkyl bromides are formed by the addition of HBr to olefins in organic traps. Since C_2Br does not make a significant contribution to the C_2 products distribution, the ratio of $C_2H_4/(C_2H_4 + C_2H_6)$ most likely represent the olefin selectivity of DBM hydrodebromination. Figure 4, C and D show the catalysis results at different temperature. Higher temperature led to higher DBM conversion, higher CH_3Br/CH_4 ratio, higher $C_{2+}/(CH_4 + C_{2+})$ ratio, and also higher olefin selectivity.

Although C_{2+} formation has been reported on dichloromethane (DCM) hydrodechlorination over Pd catalyst,[33,34] the high C_{2+} selectivity (~60%) and olefin selectivity (~90%) achieved in our work has not been reported for DCM. One possible reason is that most DCM hydrodechlorination studies were carried out at relative low temperature (typically below 250 °C) with a high H_2/DBM ratio (typically above 10), which does not favor olefin production. Another contributing factor is the relatively weaker bonds

of C−Br and Pd−Br, compared to the C−Cl and Pd−Cl bonds, which may cause higher coverage of carbon species on the palladium surface. In our proposed DBM hydrodebromination mechanism, which is illustrated in Scheme 1A, the first step would be DBM and H_2 adsorption and dissociation into CH2Brs, Br_s and H_s ("s" denotes surface). The reverse process, CH2Brs and Br_s association, is negligible because it is thermodynamically unfavorable. Therefore, the only way for Br_s to leave the surface is to combine with H_s and desorb as HBr. This reaction is reversible. The CH_2Br_s species can go through two parallel processes: combine with H_s and desorb as CH_3Br; lose the second Br and generate surface carbene species, CH_{2s}. The readsorption of CH_3Br might undergo hydrodebromination to generate CH_4, but this process is slow because the C−Br bond in CH_3Br is stronger than that in CH_2Br_2. Similar conclusions were reached in the hydrodechlorination study of CH_3Cl and CH_2Cl_2.[33,35]

The following trend could be found in the distribution of the DBM hydrodebromination products via a carbene intermediate: $nC1 > nC_2 > nC_3 > nC_4$, which implies that the formation of higher hydrocarbons might follow a F-T mechanism. This is also suggested by the olefin/paraffin ratio at different residence times. The domination of olefins at the short residence time is always regarded as one of the characteristics of F-T synthesis. Ponec et al.[36] first pointed out the analogous nature of the mechanism of hydrodechlorination of polychloromethane to F-T chemistry. This is consistent with Brady and Pettit's work using diazomethane to confirm the carbene mechanism of F-T synthesis.[37] It is generally assumed that there is not just a single reaction pathway on the catalyst surface during the F-T synthesis, but that a number of parallel operating pathways exist. Numerous reaction pathways have been proposed to explain the observed product distribution in the F-T

synthesis.[4] However, the carbene mechanism is still the most widely accepted mechanism describing the formation of hydrocarbons. Recent work on the F-T mechanism study using density functional theory (DFT) calculations shows that the carbene mechanism is more favorable than CO-insertion and the hydroxyl-carbene mechanism in many circumstances.[38]

According to Scheme 1B, the surface carbon species evolve to form longer chains via the addition of more and more CH_{2s}. There are two routes for chain termination: combining H_s and desorbing as paraffins (+H termination), or losing H_s by β−H elimination and desorbing as olefins (-H termination). Olefins could either readsorb on the catalyst surface and be hydrogenated into paraffins, or react with HBr to generate C_{2+} Br products. According to the Anderson−Schulz−Flory (ASF) theory,[39] the distribution of the F-T products obeys following equation:

$$F(n) = A\, x\, \alpha^{n-1}$$

Here, f(n) is the number of moles of C_n product, and $\alpha$is the chain propagation probability. Mechanistically, α is the ratio of the rate of propagation to the combined rate of propagation and termination.

For the products of Pd_6C-catalyzed DBM hydrodebromination, we denote by C_2 the number of moles of the molecules containing two C atoms, that is, C_2H_4 + C_2H_6 + C_2H_5Br; C_3 and C_4 are defined in the same way. We do not include CH_3Br in C_1, because CH_3Br is not formed by a carbene route. Except in the case of high temperature (400 °C), all others give linear ASF plots. A representative example is shown in Figure 5A. The α values calculated from these curves are plotted against different reaction parameters (Figure 5, B to E). The α values change little with residence time, increase with temperature, decrease with

the H_2/DBM ratio, and decrease with the DBM (H_2) partial pressure (keeping H_2/DBM at a constant ratio).

The change of α with the H_2/DBM ratio is similar to that seen in F-T synthesis, since increasing the ratio of H_2/DBM leads to increased chain termination probability. In DBM hydrodebromination, the change of α value against temperature and partial pressure is opposite to that observed in F-T synthesis. It is well-known that CO chemisorption is much stronger than H_2 chemisorption, and consequently the catalyst surface was believed to be dominated by carbon species rather than hydrogen under F-T operating conditions.4 The situation should be reversed in DBM hydrodebromination, because DBM adsorption is a dissociative adsorption, which involves C−Br bond breakage and is much weaker than CO chemisorption. Higher temperatures would favor the dissociative adsorption of DBM, and therefore the surface coverage ratio of carbon species to hydrogen species would be increased and the chain propagation probability (i.e., α) would be increased.

In F-T microkinetics, the reason for α values increasing with system pressure is that the surface concentration of carbon species increase with CO partial pressure, thus increasing the chain propagation probability. For DBM hydrodebromination, the DBM conversion is constant with changing DBM (H_2) partial pressure (keeping H_2/DBM at a constant ratio), which implies that the number of available DBM dissociative adsorption site does not change; so that the carbon species coverage does not change. On the other hand, olefin selectivity decreased with DBM (H_2) partial pressure, which implies that the surface hydrogen coverage is increased. Consequently, increasing DBM (H_2) partial pressure causes +H chain termination instead of the chain growth probability to be increased, and thereby, the α value is decreased.

To further support the DBM hydrodebromination mechanism, CH_2Br_2 and D2 were co-fed through Pd/SiO_2 at 300 °C. The outlet gas contained 27% DBM and nearly 100% of it was CH2Br2: no deuterium-substituted DBM was detected. This is evidence that the C−Br bond scission is irreversible on Pd6C surface. For the hydrodebromination products, only 2% of methyl bromide contained more than one deuterium atom, while 11% of methane contained more than two deuterium atoms. In a control experiment, a $CH_4 + D_2$ mixture was passed over the same catalyst under the similar reaction conditions and less than 1% of methane was deuterated. This suggests that most of the H/D exchange process took place after DBM molecules were dissociatively adsorbed. The higher degree of H/D exchange for methane compared to methyl bromide indicates that it takes longer for CH_2Br_s to evolve into CH_2D_2 than into CH_2DBr. This is reasonable since CH_2Br_s needs to break one C−Br bond and pick up two D_s to generate CH_2D_2, while it only needs to pick up one D_s to form CH_2DBr.

The degree of H/D exchange was very high in the longer chain halocarbons, such as ethyl bromide and propyl bromide. There are three possible explanations for this. First, the longer the carbon chain, the longer it stays on the surface, and the more chance for the H to be exchanged by D. Second, olefins traveling through the catalyst bed are adsorbed and desorbed repeatedly and have a chance to be deuterium-exchanged. The third reason is the "addition-elimination" equilibrium between olefins + HBr/DBr and alkyl bromides.

We compare next the four Group VIII metals studied in this work. It is well-known that the carbon chain growth probability in $CO + H_2$ system under identical conditions satisfies Ru > Rh > Pd > Pt,[40] because the CO bond dissociation ability on the metal surface varies in that order. Brady and Pettit[37] showed that diazomethane + H_2 could reacts on a series of

metals, including Ru and Pd, to produce CH_4 and C_{2+}. C_{2+} selectivity is much higher on Ru than on Pd. The most important difference between CH_2N_2 and CH_2Br_2 is that Br is harder to remove from the surface than N_2. Moreover a high Br coverage on Ru and Rh inhibits the dissociation of the second C−Br bond in DBM to generate surface carbenes and blocks the chain growth process. The former effect leads to high CH_3Br selectivity, while the blockage of the chain growth process leads to high selectivity toward CH_4 as opposed to C_{2+}.

For Pt, the surface coverage of Br is low. A considerable amount of surface carbenes are generated, as suggested by the high CH_4 selectivity. However, C_{2+} selectivity is still very low, which indicates that the chain growth probability on Pt surface is quite low. This might be caused by the much higher diffusion rate for H versus CH_x on the Pt surface than on the Pd surface. This idea is supported by the diffusion energy barriers calculated by DFT.[41−44]

Although none of these noble metals has a stable carbide phase under our reaction temperature, a metastable PdC_x phase can be formed under a carbon rich atmosphere,[26] such as C_2H_2, C_2H_4 , and CO, as well as DBM, as shown in this work. The formation of a metastable palladium carbide phase will greatly suppress the amount of bulk-dissolved hydrogen, which is believed to be responsible for the nonselective/total hydrogenation of alkynes into alkanes.[45,46] Here the inhibition on hydrogenation behavior by a carbide phase will have a positive effect on C_{2+} formation.

Conclusions

We provide here two potential routes to solve the DBM issue that hinders the industrial application of bromine-mediated GTL technology. In particular, these findings offer a new route for the synthesis of light olefins from methane. The reaction of DBM and hydrogen was studied on several silica supported transition metals. Pd_6C supported on SiO_2 showed

the highest selectivity for the conversion of DBM to higher hydrocarbons, mainly light olefins, analogous to the F-T catalysts. Silica supported ruthenium shows the highest selectivity for the conversion of DBM to methyl bromide, analogous to the methanol synthesis catalysts.

References

(1) Crabtree, R. H. Chem. Rev. 1995, 95, 987−1007.

(2) York, A. P. E; Xiao, T. C.; Green, M. L. H.; Claridge, J. B. Catal. Rev. - Sci. Eng. 2007, 49, 511−560.

(3) Mokrani, T.; Scurrell, M. Catal. Rev. - Sci. Eng. 2009, 51, 1−145.

(4) Fischer−Tropsch Technology; Steynberg, A. P., Dry, M. E., Eds.; Elsevier Science & Technology Books: Amsterdam, The Netherlands, 2004.

(5) Holmen, A. Catal. Today 2009, 142, 2−8.

(6) Keller, G. E.; Bhasin, M. M. J. Catal. 1982, 73, 9−19.

(7) Lunsford, J. H. Angew. Chem., Int. Ed. Engl. 1995, 34, 970−980.

(8) Wang, L. S.; Tao, L. X.; Xie, M. S.; Xu, G. F.; Huang, J. S.; Xu, Y. D. Catal. Lett. 1993, 21, 35−41.

(9) Periana, R. A.; Taube, D. J.; Gamble, S.; Taube, H.; Satoh, T.; Fujii, H. Science 1998, 280, 560−564.

(10) Tabata, K.; Teng, Y.; Takemoto, T.; Suzuki, E.; Banares, M. A.; Pena, M. A.; Fierro, J. L. G. Catal. Rev. - Sci. Eng. 2002, 44, 1−58.

(11) Olah, G. A.; Gupta, B.; Farina, M.; Felberg, J. D.; Ip, W. M.; Husain, A.; Karpeles, R.; Lammertsma, K.; Melhotra, A. K.; Trivedi, N. J. J. Am. Chem. Soc. 1985, 107, 7097−7105.

(12) Lorkovic, I. M.; Sun, S. L.; Gadewar, S.; Breed, A.; Macala, G. S.; Sardar, A.; Cross, S. E.; Sherman, J. H.; Stucky, G. D.; Ford, P. C. J. Phys. Chem. A 2006, 110, 8695−8700.

(13) Podkolzin, S. G.; Stangland, E. E.; Jones, M. E.; Peringer, E.; Lercher, J. A. J. Am. Chem. Soc. 2007, 129, 2569−2576.

(14) Butter, S. A.; Jurewicz, A. T.; Kaeding, W. W. U.S. Patent 3894107, 1975.

(15) Lersch, P.; Bandermann, F. Appl. Catal. 1991, 75, 133−152.

(16) Svelle, S.; Aravinthan, S.; Bjorgen, M.; Lillerud, K. P.; Kolboe, S.; Dahl, I. M.; Olsbye, U. J. Catal. 2006, 241, 243−254.

(17) Gadewar, S. B.; Wyrsta, M. D.; Grosso, P.; Zhang, A. H.; McFarland, E. W.; Komon, Z. J. A.; Sherman, J. H. U.S. Patent 7579510, 2009.

(18) Olah, G. A.; Doggweiler, H.; Felberg, J. D.; Frohlich, S.; Grdina, M. J.; Karpeles, R.; Keumi, T.; Inaba, S.; Ip, W. M.; Lammertsma, K.; Salem, G.; Tabor, D. C. J. Am. Chem. Soc. 1984, 106, 2143−2149.

(19) Nilsen, M. H.; Svelle, S.; Aravinthan, S.; Olsbye, U. Appl. Catal., A 2009, 367, 23−31.

(20) Urbano, F. J.; Marinas, J. M. J. Mol. Catal. A 2001, 173, 329− 345.

(21) Alonso, F.; Beletskaya, I. P.; Yus, M. Chem. Rev. 2002, 102, 4009−4091.

(22) Fung, S. C.; Sinfelt, J. H. J. Catal. 1987, 103, 220−223.

(23) Lunin, V. V.; Lokteva, E. S. Russ. Chem. Bull. 1996, 45, 1519− 1534.

(24) Wiersma, A.; van de Sandt, E. J. A. X.; den Hollander, M. A.; van Bekkum, H.; Makkee, M.; Moulijn, J. A. J. Catal. 1998, 177, 29−39.

(25) Kulkarni, P. P.; Deshmukh, S. S.; Kovalchuk, V. I.; d'Itri, J. L. Catal. Lett. 1999, 61, 161−166.

(26) Ziemecki, S. B.; Jones, G. A.; Swartzfager, D. G.; Harlow, R. L. J. Am. Chem. Soc. 1985, 107, 4547−4548.

(27) vandeSandt, E. J. A. X.; Wiersma, A.; Makkee, M.; vanBekkum, H.; Moulijn, J. A. Appl. Catal., A 1997, 155, 59−73.

(28) Heinrichs, B.; Noville, F.; Schoebrechts, J. P.; Pirard, J. P. J. Catal. 2003, 220, 215−225.

(29) Nutt, M. O.; Hughes, J. B.; Wong, M. S. Environ. Sci. Technol. 2005, 39, 1346−1353.

(30) Greeley, J.; Mavrikakis, M. J. Phys. Chem. B 2005, 109, 3460− 3471.

(31) Migani, A.; Illas, F. J. Phys. Chem. B 2006, 110, 11894−11906.

(32) Abell, P. I. Faraday Trans. 1964, 60, 2214−2223.

(33) Alvarez-Montero, M. A.; Gomez-Sainero, L. M.; MartinMartinez, M.; Heras, F.; Rodriguez, J. J. Appl. Catal., B 2010, 96, 148−156.

(34) de Pedro, Z. M.; Casas, J. A.; Gomez-Sainero, L. M.; Rodriguez, J. J. Appl. Catal., B 2010, 98, 79−85.

(35) Chen, N.; Rioux, R. M.; Barbosa, L.; Ribeiro, F. H. Langmuir 2010, 26, 16615−16624.

(36) Vanbarneveld, W. A. A.; Ponec, V. J. Catal. 1984, 88, 382−387.

(37) Brady, R. C.; Pettit, R. J. Am. Chem. Soc. 1980, 102, 6181−6182.

(38) Cheng, J.; Hu, P.; Ellis, P.; French, S.; Kelly, G.; Lok, C. M. Top. Catal. 2010, 53, 326−337.

(39) Van der Laan, G. P.; Beenackers, A. A. C. M. Catal. Rev. - Sci. Eng. 1999, 41, 255−318.

(40) Vannice, M. A. J. Catal. 1975, 37, 449−461.

(41) Paul, J. F.; Sautet, P. J. Phys. Chem. B 1998, 102, 1578−1585.

(42) Watson, G. W.; Wells, R. P. K; Willock, D. J.; Hutchings, G. J. J. Phys. Chem. B 2001, 105, 4889−4894.

(43) Ford, D. C.; Xu, Y.; Mavrikakis, M. Surf. Sci. 2005, 587, 159− 174.

(44) Nave, S.; Tiwari, A. K.; Jackson, B. J. Chem. Phys. 2010, 132, 054705.

(45) Teschner, D.; Borsodi, J.; Wootsch, A.; Revay, Z.; Havecker, M.; Knop-Gericke, A.; Jackson, S. D.; Schlogl, R. Science 2008, 320, 86−89.

(46) Seriani, N.; Mittendorfer, F.; Kresse, G. J. Chem. Phys. 2010, 132, 024711.

Appendix B: C-H Bond Activation by Pd-substituted CeO_2 : Substituted Ions versus Reduced Species

Introduction

Heterogeneous catalysis on the surfaces of platinum group metals (PGMs) has long been studied, and the fundamental processes are now understood in extraordinary detail from both experimental and theoretical bases. Much less is known about the surface chemistry of PGM species when they exist as ions in solid-state materials such as simple and complex oxides.[1]

In a recent review, Thomas[2] promotes the idea of catalysis on single active sites, well-separated from one another, in a manner that mimics homogeneous catalysis. This important design principle for novel approaches to element-efficient heterogeneous catalysis has been

demonstrated through the use of ionic species substituted on cation sites in metal oxides, including the use of Pd^{2+} -substituted metal oxides. Hegde and co-workers[3] have shown conclusively that substituted PGM ions are active for CO removal from gas streams,[4] and as automotive three- way catalysts.[5] Pfefferle and co-workers[6] have found that in CH_4 combustion, the role of PdO and related species is crucial. It has been further suggested that the oxidized state of Pd^{2+} (as opposed to metallic Pd^{2+}) may be the most active species when using substituted complex oxides for catalysis.[7−9] Perhaps the most compelling evidence for using Pd-substituted oxides for heterogeneous catalysis comes from the successful application of "intelligent catalysts" for automotive emissions control.[10]

In this contribution, we use ultrasonic spray pyrolysis (USP) as a simple and clean method to prepare Pd-substituted CeO_2 catalysts with particle sizes in the sub-10 nm range. We have characterized these materials using electron microscopy, X-ray photoelectron spectroscopy, and synchrotron X-ray diffraction (XRD) and observe that Pd substitutes in the lattice at least up to x = 0.10 in $Ce_{1-x}Pd_xO_{2-\delta}$. In this work, $Ce_{1-x}Pd_xO_{2-\delta}$ was tested for C−H bond activation reactions. While there are reports of complete and partial CH_4 oxidation over Pd,[11−15] a wealth of literature has been published on Pd and CeO_2 containing catalysts for CH_4 combustion,[16−23] CO oxidation,[24−27] and NO_x abatement.[28] The oxygen storage capacity of CeO_2 is enhanced when substituted with Pd,[29−33] and doping promotes the formation of oxygen vacancies in catalysis.[5,34,35] It has also been demonstrated that CeO_2 supported catalysts and Pd supported on CeO_2 are active for the water-gas shift reaction.[36−38] Additionally, it was also shown that a Pd-containing catalyst effectively converted CH_4 to a methanol derivative in solution.[39] The study of CH_4 activation reactions has important energy applications. While large reserves of CH_4 exist and considerable portions of these

reserves are currently used to heat homes and generate hydrogen for other synthetic processes, it is widely accepted that the conversion of CH_4 to liquid hydrocarbon fuels efficiently with an inexpensive and robust catalyst would be a substantial contribution to alternative energy research.[40] The usual Fischer−Tropsch strategy requires oxidation to mixtures of CO and H_2, which are then converted to higher hydrocarbons. Alternate partial oxidation strategies could be a more direct route to valuable products. For example, dry reforming of CH_4 is of value because recovered CH_4 is often found in the presence of CO_2. As large-scale separations are expensive, it would be convenient to identify a catalyst that efficiently converts CH_4 to useful products in the presence of CO_2.[41] We address the following questions in this work: (i) Does USP provide a useful route to single-phase Pd-substituted CeO_2 with high surface area? (ii) Can Pd-substituted CeO_2 be used as a catalyst for CH_4 activation in the presence of O2 (partial oxidation) or CO_2 (dry reforming)? (iii) Can it be concluded that a substituted PGM ion is active for C−H bond activation? We found that Pd-substituted CeO_2 behaves in a manner that is nearly indistinguishable from supported Pd on CeO_2 as a result of the reduction of Pd^{2+} ions to Pd nanoparticles on CeO_2 . This study complements prior work on the use of Pt substituted CeO_2 as a catalyst for CH_4 activation.[42]

Experimental Section

Pd-substituted CeO_2 was prepared using USP. The USP setup is based on the apparatus described by Skrabalak et al.,[43] which they used for the preparation of nanoporous carbon. The precursor solution, containing $Ce(NO_3)3{\cdot}6H_2O$ (99%, Aldrich) and Pd(NO3)2·2 H_2O (99.999%, Aldrich) dissolved in the appropriate molar ratios in Millipore water, was nebulized in the custom reaction vessel over a Sunpenton humidifier. The precursor mist was carried by compressed air through a vitreous silica tube in a Lindberg Blue/M tube

furnace at 500 °C. Product powders were collected in bubblers containing 4:1 H_2O/EtOH. The suspensions were evaporated in crystallization dishes at 80 °C overnight, and the dry powder was collected.

Room temperature XRD data was collected on a Philips X′PERT diffractometer, and in situ variable temperature diffraction experiments were performed with a Bruker D8 diffractometer equipped with an Anton Parr hot-stage. Synchrotron X-ray powder diffraction patterns were collected in transmission mode at room temperature on beamline 11-BM at the Advanced Photon Source, Argonne National Laboratory, with an X-ray energy of near 30 keV. No evidence for sample degradation or damage was observed. Rietveld refinements were performed using the XND code.[44] X-ray photoelectron spectra were obtained on a Kratos Axis Ultra Spectrometer with a monochromatic Al−Kα source (E = 1486.7 eV). Samples were mounted on a stainless steel sample holder using double-sided carbon tabs. The residual pressure inside the analysis chamber was below 7×10^{-9} Torr. Survey spectra over wide ranges of binding energy were acquired using an analyzer pass energy of 160 eV, and spectra of Pd 3d levels were acquired at a pass energy of 80 eV. Spectra were calibrated to the C 1s peak from adventitious hydrocarbons, expected at a binding energy of 285.0 eV. For peak fitting of the spin−orbit doublets in high resolution scans, the d3/2 to d5/2 peak area was constrained to a ratio of 2/3. Scanning electron micrographs (SEMs) were acquired on an FEI XL40 Sirion FEG digital scanning microscope. SEM sample stages were sputtered with Au plasma prior to imaging to reduce sample charging. Transmission electron micrographs (TEMs) were taken on an FEI Tecnai G2 Sphera Microscope. TEM copper-coated Cu grids were prepared by dropcasting a dilute suspension of product in ethanol onto

grids. Brunauer−Emmett−Teller (BET) surface area measurements were made on a MicroMetrics TriStar 3000 porosimeter using N_2 as probe gas.

Catalytic testing was carried out in a home-built packed bed reactor, equipped with MKS mass flow controllers and mass spectrometer (SRS) for data acquisition. Quartz tubes (inner-diameter = 4 mm) were packed with 25 mg of catalyst and 50 mg of HPLC grade aluminum oxide (Aldrich) to prevent hotspots, with quartz wool plugs on both ends of the powder. The loosely packed powder occupies a length of 1 cm to maintain a space-time of 0.18 s with a total flow rate of 30 sccm. Reactions were ramped from room temperature to 600 °C at a rate of 10 °C/min. Catalysts were pretreated with Ar, 20% H_2/Ar balance, or 20% O_2/Ar balance. During partial oxidation of CH_4 a 2:1 ratio of CH_4 /O_2 was set to flow over the catalyst. This ratio is the stiochiometric amount to produce synthesis gas: $CH_4 + 1/2\ O_2 \rightarrow CO + 2H_2$. All gases had a stated purity of better than 99.99%.

Anticipated products for partial oxidation reactions (2:1 CH_4/O_2) include combustion productions (CO_2 and H_2O), synthesis gas (various ratios of H_2 and CO), oxidative coupling products (C_2H_6, C_2H_4, C_2H_2), and methanol. The mass spectrometer was set to record the activity of the m/z ratios corresponding to these products. While heating any hydrocarbon in the presence of oxygen to high temperatures, combustion products are expected. It is possible for unreacted CH_4 to react with any CO_2 produced from combustion and proceed to do dry reforming of CH_4 to produce synthesis gas ($CO + H_2$). If CO and H_2 were produced during partial oxidation of CH_4, catalysts were tested for dry reforming of CH_4 , in which CH_4 reacts with CO_2 produced from combustion. If CH_4 reacts with CO_2 to produce synthesis gas, then this is a possible mechanistic route for syngas production during partial oxidation reactions.

The anticipated products for dry reforming of CH_4 (1:1 CH_4 / CO_2) are synthesis gas (H_2 and CO). The mass spectrometer was set to record the m/z ratios corresponding to all of the products listed for partial oxidation reactions. All subsequent reactions were chosen based on the material's behavior during partial oxidation conditions. Other reactions studied in this work include ethylene hydrogenation (1:1 C_2H_4/H_2) to 300 °C heated at 10 °C/min. Anticipated products of this reaction include ethane and water. The results of characterization of $Ce_{1-x}Pd_xO_{2-\delta}$ and catalytic testing follow.

Results and Discussion

Characterization of $Ce_{1-x}Pd_xO_{2-\delta}$

Pd-substituted CeO_2 ($Ce_{1-x}Pd_xO_{2-\delta}$) was prepared with x = 0.025, 0.05, 0.075, 0.1 via USP. Representative scanning electron micrographs for a sample with x = 0.05 of the as-prepared powders are shown in Figure 1a. The hollow sphere morphology of the powders is evident in the higher magnification image presented in the inset. The morphology presumably results from evaporation of liquid as the mist traveled through the furnace, leaving behind polydispersed hollow spheres. Despite the relatively large size of the agglomerates, the crystallites of which the spheres are composed are rather fine, with grain sizes on the order of 5 nm, as seen in the transmission electron micrographs of Figure 1b. The $Ce_{0.95}Pd_{0.05}O_{2-\delta}$ powder prepared by USP has BET surface area of about 32 m^2/g.

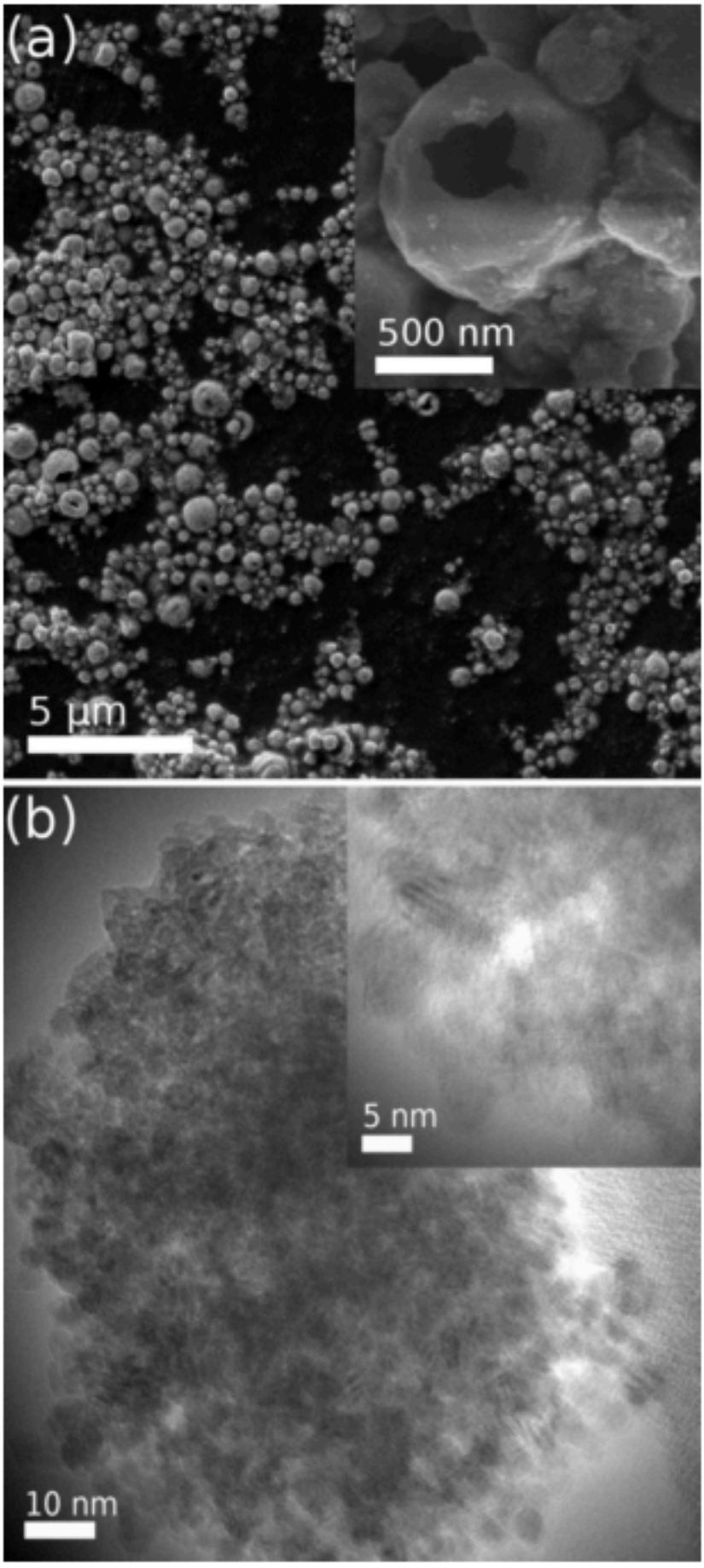

asdfasd

Figure 1. (a) Scanning electron micrograph of $Ce_{0.95}Pd_{0.05}O_{2-\delta}$ particles prepared by nebulized USP showing a hollow sphere morphology. (b) Transmission electron micrograph of the $Ce_{0.95}Pd_{0.05}O_{2-\delta}$ particles showing that hollow spheres are composed of approximately 5 nm crystallites, confirming the correlation length obtained from line broadening from synchrotron XRD.

High-resolution synchrotron X-ray powder diffraction patterns and corresponding Rietveld refinements are shown in Figure 2 for the as-prepared samples and after calcination at 700 °C for 16 h. Pure fluorite CeO_2 is the only phase observed, and no phase segregation occurs in any of the compositions. We did not attempt to prepare materials with Pd concentrations higher than 10 mol %. The diffraction profiles are broader in the substituted materials, relative to pure CeO_2 , and this is especially pronounced in the calcined samples. Refinements were performed with models fixed at the nominal stoichiometry of each sample ($\delta = x$) with Pd residing on the Ce site, and the atomic displacement parameters (ADP) of Pd and Ce were constrained to the same value. Because the Pd and O occupancies, ADPs, and global scale factor are strongly correlated, the occupancies cannot be refined. For this reason, it is not possible to directly demonstrate the solid solubility of Pd in CeO_2 from average structure (Rietveld) refinement techniques using XRD data.

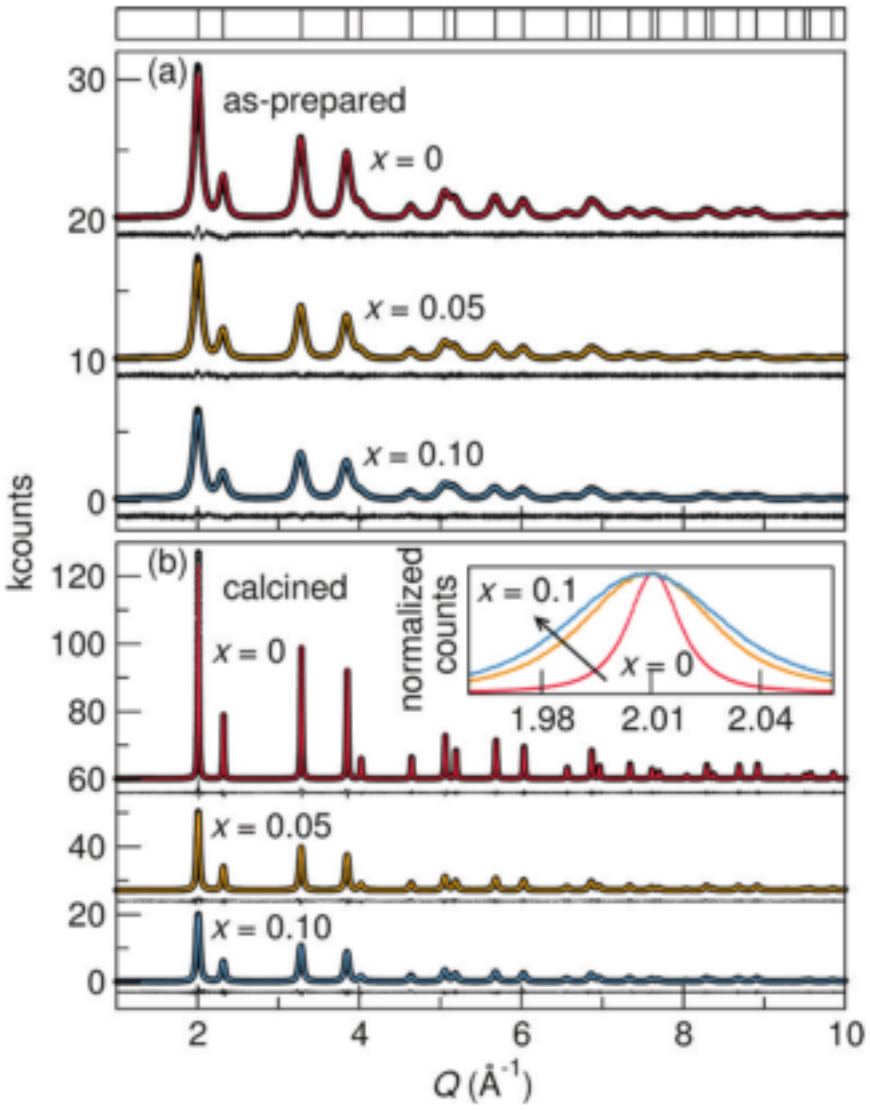

Figure 2. (a) Synchrotron XRD data for as-prepared $Ce_{1-x}Pd_xO_{2-\delta}$ with x = 0, 0.05, and 0.1. All samples are single-phase fluorite. Vertical bars in the topmost panel indicate expected fluorite CeO_2 reflection positions. (b) Diffraction from samples after calcining in air for 16 h at 700 °C, with significant peak narrowing because of sintering. The inset shows the strongest reflection, with height normalized, for samples with increasing Pd^{2+} substitution, x. Samples with higher x values are seen to possess significantly broader peaks.

Thermodiffraction shows the evolution of the 111 and 200 reflections of CeO_2 between room temperature and 700 °C for unsubstituted CeO_2 (x = 0) and 5% Pd-substituted CeO_2 (x

= 0.05). Diffraction profiles of pure CeO_2 narrow with increasing temperatures, while the peak widths of the substituted material remain significantly broader. The distinct behaviors are indirect evidence that Pd is substituted into the CeO_2 lattice, and suggests that sintering may be suppressed in the substituted material. These points are discussed in greater detail with respect to analysis of synchrotron X-ray powder diffraction studies of the $Ce_{1-x}Pd_xO_{2-\delta}$ series.

There are considerable challenges associated with structure determination and refinement of nanoscale materials from Bragg scattering-based diffraction analysis. While it is known that systematic errors arise in the determination of lattice parameters for nanocrystalline materials,[45] this is infrequently acknowledged. Using the Debye function, Palosz and co- workers simulated diffraction patterns for perfect SiC nano- crystallites with sizes ranging from 3 to 8 nm and refined the simulated data by the Rietveld method.[45] Interestingly, they found that in the approximation of a perfect experiment, that is, no sample-offset error, the refined lattice constant was systematically overestimated, increasingly as the crystallite size decreased. In refinements approximating an imperfect experiment in which the sample-offset error was allowed to float, the refined lattice constant was increasingly underestimated as the crystallite size decreased. Thus, even within the approximation that a nanomaterial is a small single-crystalline piece of the bulk material, Rietveld refinement fails to accurately extract the lattice parameters. In this light, it is clear that great care must be taken when establishing trends in the variation of lattice parameters determined by Rietveld analysis.

The situation is further complicated by the fact that nanocrystallites are not simply small portions of a bulk material. Conventional crystallographic analysis operates on the

assumption that the environment of each lattice point is identical. While this may be well approximated by atoms within the core of a nanoparticle, it certainly does not apply to the under-coordinated atoms at or near the surface. For this reason, a single group of lattice constants does not capture the complexity inherent to real nanocrystals. Palosz et al. have extensively discussed limitations of Rietveld analysis for structure determination in nanocrystalline materials.[45−47]

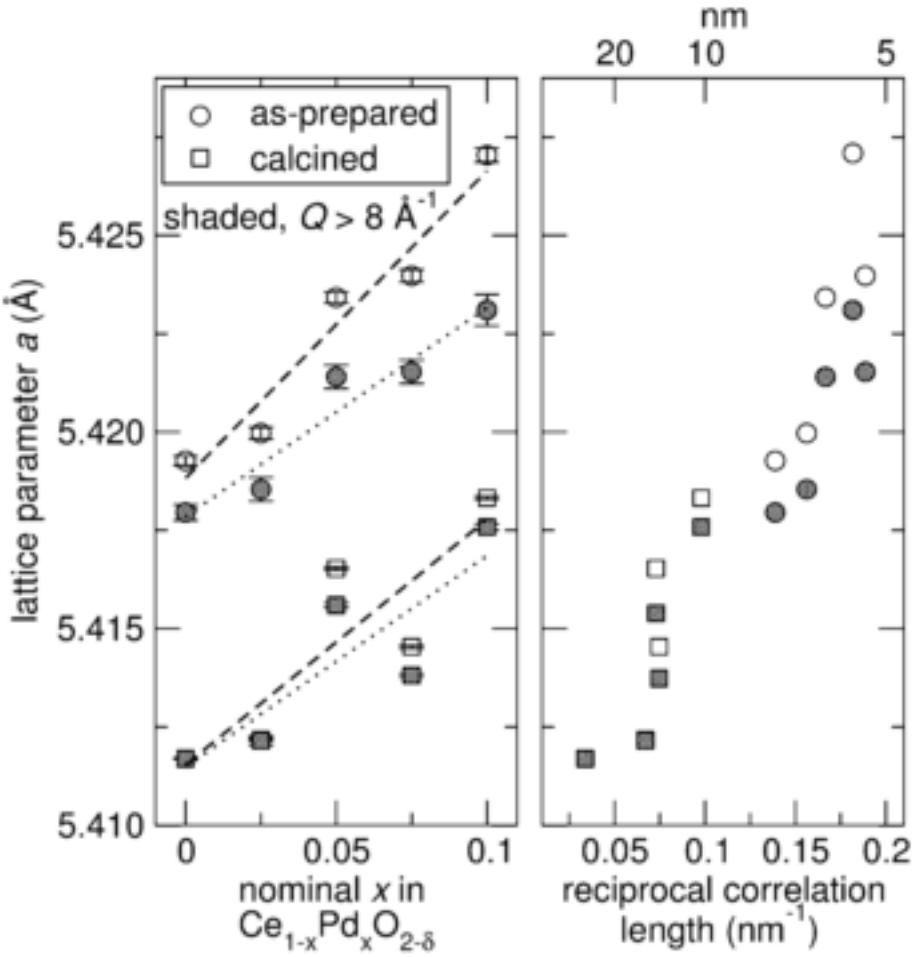

Figure 3. (a) Variation of the cubic cell parameter of $Ce_{1-x}Pd_xO_{2-\delta}$ as a function of nominal Pd substitution x. Data are displayed for as- prepared and calcined samples separately, as described in the text. The cubic cell parameter was determined for the whole Q range of data, and separately for data with Q > 8 Å−1, shown with shaded symbols. (b)

Cell parameters displayed as a function of the reciprocal crystalline correlation length as obtained from Williamson−Hall analysis of synchrotron XRD data.

With these limitations in mind, we address the observed variation of the lattice constant as a function of substitution level with caution. It is clear from the thermodiffraction and synchrotron studies that Pd-substitution in CeO_2 reduces the XRD-coherent correlation length. In Figure 3a, the refined lattice parameters of the as-prepared and calcined samples are plotted against the nominal Pd content x. One method for reducing the error associated with lattice parameter determi- nation in nanoparticles is to refine only the high Q portion of a diffraction pattern, although this is only effective in the approximation of a perfect crystallite. Despite this known limitation, the lattice parameters from refining over the entire Q range (open symbols) and only the high Q portion of the patterns (shaded symbols, $Q > 8$ $Å^{-1}$) are compared in Figure 3a. It is immediately clear that the as-prepared samples appear to have larger lattice constants than the calcined materials. The lattice constants of the as-prepared materials are reduced when only the high Q portions of the patterns are refined; the effect is less pronounced in the calcined materials. $Ce_{1-x}Pd_xO_{2-\delta}$ seems to exhibit Végard style behavior with a lengthening of a as the Pd concentration is increased. This would be consistent with increased cation−cation repulsion arising from the removal of oxygen because of the aliovalent substitution of Pd^{2+} for Ce^{4+}. However, the Shannon−Prewitt ionic radius of 4-coordinate Pd^{2+} (0.64 Å) is significantly smaller than the radius of 8- coordinate Ce^{4+} (0.97 Å), so it is difficult to know whether the observed expansion is an artifact of differences in crystalline correlation lengths, or accurately representative of differences in the lattice constants.

Table 1. Volume Weighted Particle Sizes (D_v) and Strain (ε) Obtained from a Williamson−Hall Analysis of Synchrotron X-ray Powder Diffraction for $Ce_{1-x}Pd_xO_{2-\delta}$ Where x = 0, 0.025, 0.05, 0.075, 0.1

		calcined			
	as-prepared	(00*l*)		other reflections	
x	D_v (Å)	D_v (Å)	ε (%)	D_v (Å)	ε (%)
0	72 ± 15	293 ± 2	0.03 ± 1	296 ± 9	0.06 ± 3
0.025	64 ± 11	157 ± 4	0.13 ± 1	149 ± 5	0.16 ± 1
0.05	60 ± 5	118 ± 3	0.11 ± 1	137 ± 1	0.27 ± 1
0.075	53 ± 7	123 ± 5	0.11 ± 2	134 ± 6	0.24 ± 1
0.10	55 ± 12	101	0.16	102 ± 5	0.30 ± 2

To address whether the variation in the lattice parameter across the series is due to systematic differences in the crystallite sizes, we performed a Williamson−Hall analysis[48] on each of the patterns. It is important to point out that neither Scherrer nor Williamson−Hall analyses are quantitatively accurate methods for extracting correlation lengths, though they do provide reasonable first-order estimates.[45] Additionally, in the case of nanocrystallites of relatively small sizes, < 10 nm, the strain parameter extracted by the WH method carries little physical meaning.[47] We elected to do a Williamson−Hall analysis because it involves fitting over the entire observed Q range, but we note that similar estimates of the correlation lengths were obtained by Scherrer analysis of a single reflection. The refined lattice constants are plotted in Figure 3b as a function of the inverse correlation length estimated from the WH analysis; the volume weighted particle sizes and strains are given in Table 1. As a function of the inverse correlation length, the lattice parameters follow an approximately linear trend. It is not possible to conclude whether the observed differences result from systematic errors inherent to the Rietveld method, or whether they genuinely

reflect differences between the samples. Within the associated error, the estimated strain is almost constant across the series of as-prepared samples. In the calcined materials, the estimated strain increases significantly in going from the x = 0 unsubstituted material to x = 0.025, and then gradually increases with the Pd concentration.

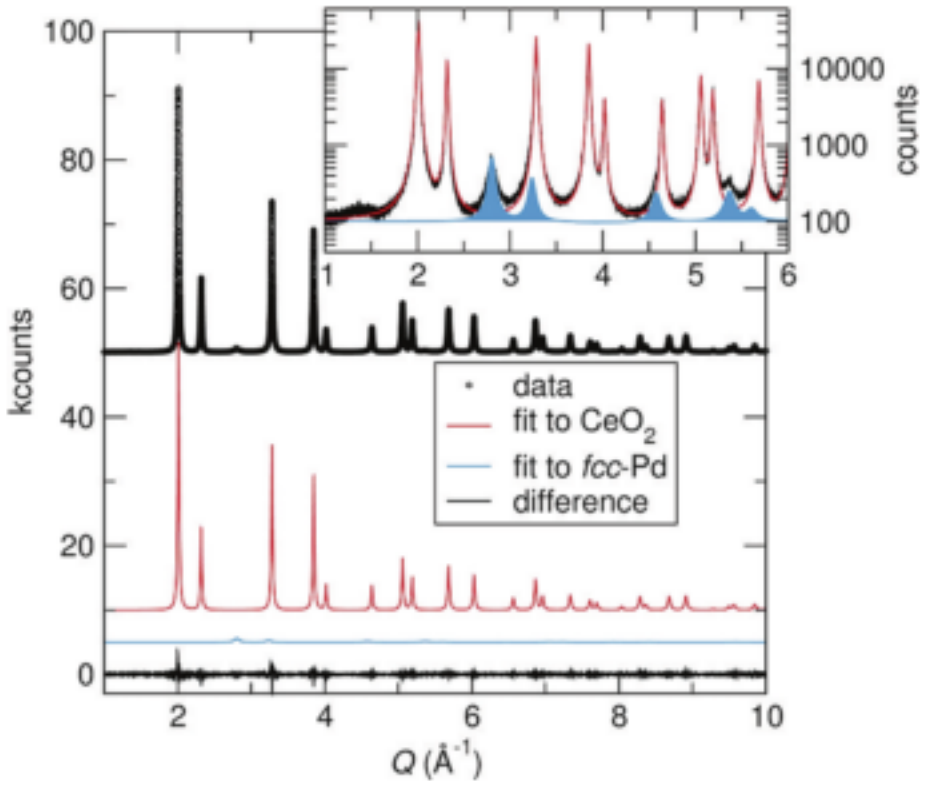

Figure 4. Synchrotron XRD data for $Ce_{0.95}Pd_{0.05}O_{2-\delta}$ reduced in 5% H_2 in Ar at 700 °C for 8 h. The Rietveld refinement shows fcc-Pd metal to be quantitatively present with a mole ratio of 0.05.

It is clear that Rietveld analysis cannot provide direct evidence that Pd substitution occurs in CeO_2, complicated by the many factors we have discussed. Nonetheless, the fact that these are single-phase materials displaying significantly different behavior upon calcination compared to pure CeO_2 , coupled with the observation that the XRD-coherent correlation length changes as a function of Pd concentration, are highly suggestive that Pd is

dispersed in the CeO_2 lattice. Verification that the nominal Pd concentrations are indeed reflective of the actual compositions is obtained by fully reducing the samples to two- phase mixtures of CeO_2 and *fcc*-Pd metal. A synchrotron XRD pattern and corresponding Rietveld refinement for one such sample (x = 0.05) are shown in Figure 4. The *fcc*-Pd contribution is estimated to be 4.7 mol % by quantitative phase analysis, in excellent agreement with the presumed Pd content.

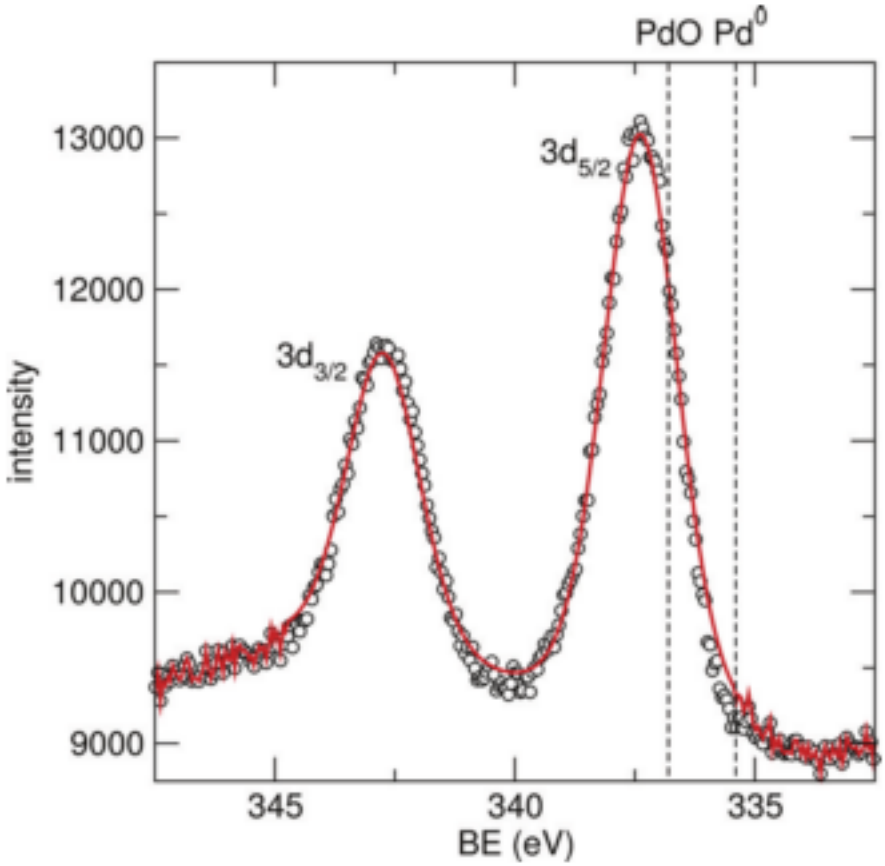

Figure 5. X-ray photoelectron spectrum of the Pd 3d region of as- prepared $Ce_{0.95}Pd_{0.05}O_{2-\delta}$ acquired with a pass energy of 80 eV. The Pd 3d5/2 peak is shifted to higher binding energy than found in PdO (dashed line indicates position) suggesting a more ionic charge state than that of PdO. No evidence for metallic Pd is seen.

Scanlon et al. recently described an ab initio study of Pd and Pt substitution in CeO_2 and demonstrated that because of crystal field stabilization effects, the PGM substituents prefer to displace off the ideal Ce lattice position by about 1.2 Å to adopt square planar coordination, the most common coordination geometry for d8 cations.33 This result emphasizes the importance of applying structural probes that are sensitive to local environments. While EXAFS studies have been reported on the $Ce_{1-x}Pd_xO_{2-\delta}$ system,[49,50] we are not aware of any attempts to fit models similar to the one proposed by Scanlon et al.

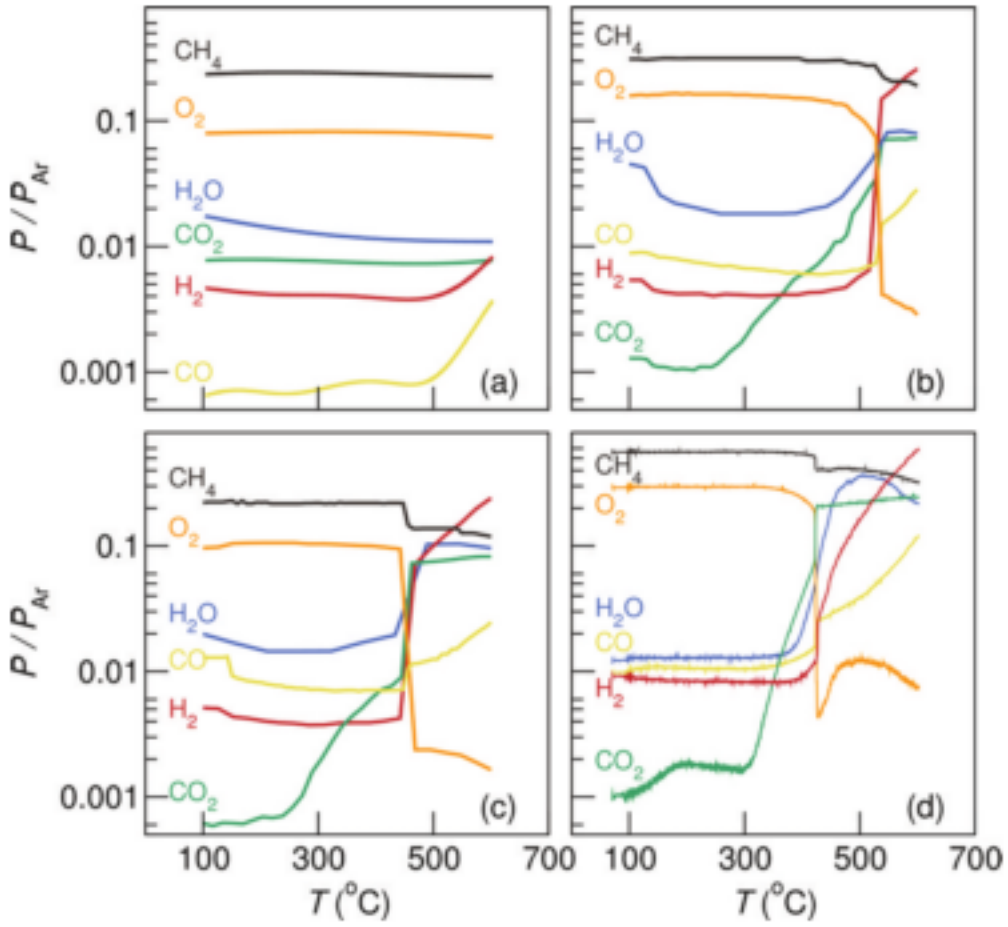

Figure 6. Partial oxidation of methane (2:1 CH_4 /O2) in Ar heated at 10 °C/min to 600 °C over (a) CeO_2 , (b) preoxidized (20% O2 in Ar to 500 °C 1 h) $Ce_{0.95}Pd_{0.05}O_{2-\delta}$, (c) prereduced (20% H_2 in Ar to 500 °C 1 h) $Ce_{0.95}Pd_{0.05}O_{2-\delta}$, and (d) prereduced (20% H_2 in Ar

to 500 °C 1 h) PdO/CeO_2 . Almost no reaction is observed over pure CeO_2 . The substituted Pd catalyst produces combustion products and non- stoichiometric synthesis gas during partial oxidation and behaves similarly to the supported Pd catalyst under reaction conditions.

X-ray photoelectron spectroscopy (XPS) of the Pd 3d region was investigated to determine the charge state of substituted Pd in $Ce_{0.95}Pd_{0.05}O_{2-\delta}$. Indicated in Figure 5 are the binding energies for the Pd $3d_{5/2}$ signal in PdO (336.8 eV) and Pd metal (335.4 eV).[51] In Figure 5, the Pd $3d_{5/2}$ signal for $Ce_{0.95}Pd_{0.05}O_{2-\delta}$ is seen at 337.4 eV, a slightly higher binding energy than that of PdO or Pd metal. The increased ionic character suggests Pd lattice substitution. This shift to higher binding energy is in agreement with the XPS of the Pd 3d region taken by Singh et al. for $Ce_{0.95}Pd_{0.05}O_{2-\delta}$ prepared via solution combustion synthesis in which the $3d_{5/2}$ signal is seen at 337.4 eV.[52] Though this does not entirely rule out the possibility of PdO clusters on the surface, both bulk probes like diffraction and surface probes like XPS suggest ionic Pd is incorporated into the CeO_2 lattice. The purpose of this study of was also to determine if amorphous PdO, undetectably by XRD, was present on the sample. Because of the low resolution of the XPS data, it would not be possible to deconvolute the two Pd^{2+} signals. However, if amorphous PdO were present, it would crystallize upon calcination.

Reactivity Studies

The $Ce_{1-x}Pd_xO_{2-\delta}$ series was tested for C−H bond activation in partial oxidation of CH_4 and dry reforming of CH_4 . Partial oxidation was tested over pure CeO_2 as a control (Figure 6a). Even at 600 °C there is no conversion of CH_4 to products of interest. Whereas the USP

prepared CeO_2 was inactive, Figure 6 shows the Pd-substituted CeO_2 catalyst is active for CH_4 combustion.

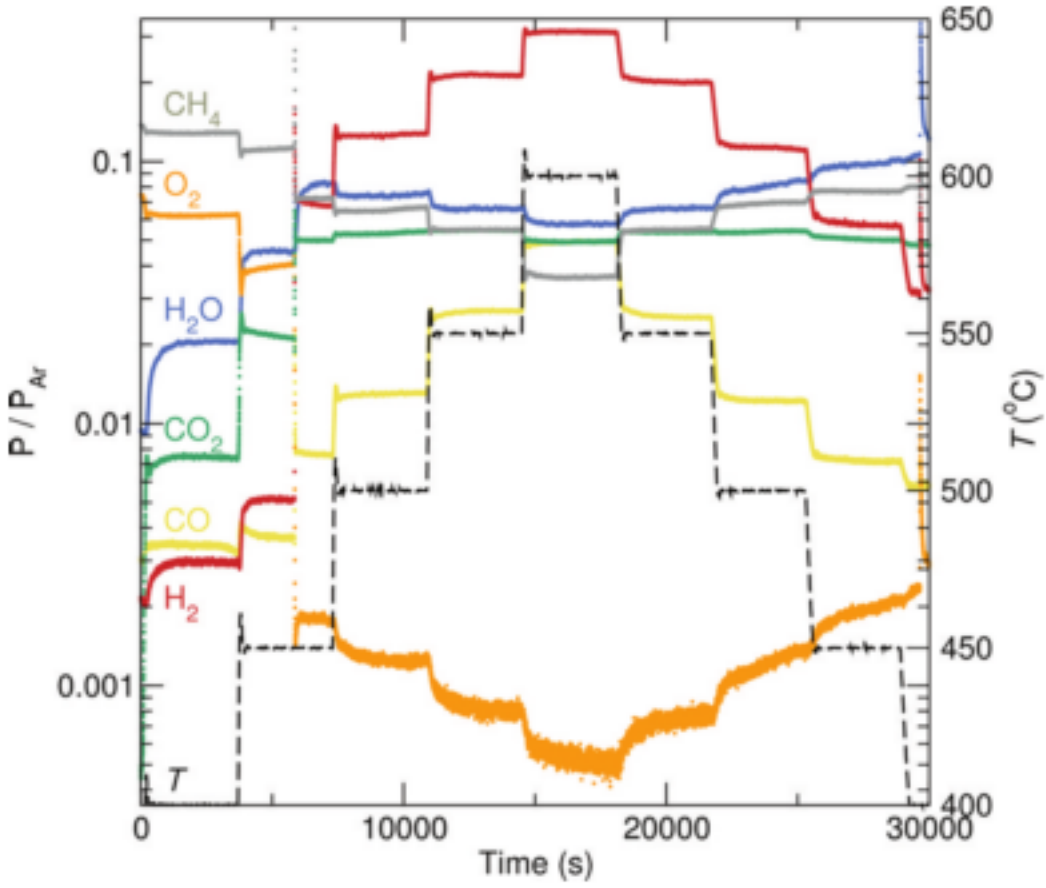

Figure 7. Steady state partial oxidation of methane (2:1 CH_4 /O2) in Ar heated in 50 °C increments from 450 to 600 °C with a dwell time of 1 h at each temperature step over $Ce_{0.95}Pd_{0.05}O_{2-\delta}$. At 450 °C sufficient Pd metal is present to produce nonstoichiometric synthesis gas, H_2 in excess. After combustion, several secondary reactions occur including steam reforming and water gas shift.

It was of interest to use a minimum amount of PGM while still achieving C−H bond activation. The quantitative work was performed primarily on $Ce_{0.95}Pd_{0.05}O_{2-\delta}$ which was found by us to be slightly more active than $Ce_{0.95}Pd_{0.05}O_{2-\delta}$ and approximately the same as

$Ce_{0.925}Pd_{0.075}O_{2-\delta}$. For partial oxidation of CH_4, $Ce_{0.95}Pd_{0.05}O_{2-\delta}$ was subjected to either prereduction or preoxidation. In both pretreatment cases, the same reaction character is observed. The only difference the pretreatment yields is a slightly lower activation temperature for the prereduced sample. In partial oxidation over $Ce_{0.95}Pd_{0.05}O_{2-\delta}$ (Figures 6b,c), combustion products (CO_2 and H_2O) were observed along with nonstoichiometric synthesis gas. Excess H_2 is produced from the partial oxidation of CH_4 over $Ce_{0.95}Pd_{0.05}O_{2-\delta}$.

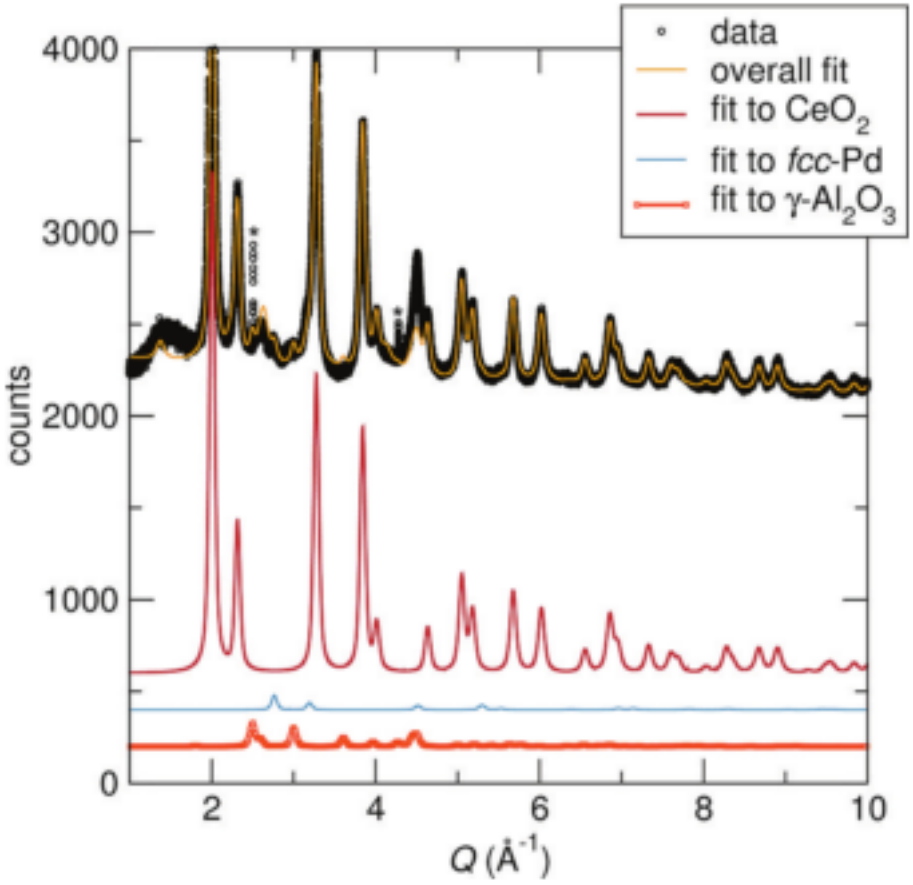

Figure 8. Synchrotron XRD data for $Ce_{0.95}Pd_{0.05}O_{2-\delta}$ mixed with γ-Al_2O_3 after use as catalyst under partial oxidation conditions to 600 °C. The Rietveld refinement shows fcc-Pd metal present along with diluent Al_2O_3. The asterisks indicate an unidentified impurity.

To consider if CH_4 is reacting with CO_2 produced from combustion, dry reforming of CH_4 was tested separately. The same two pretreatments were performed individually. The

pretreatment makes very little difference in the reaction character and the activation temperature of the catalyst. Very minimal synthesis gas was producing during dry reforming of CH_4 over $Ce_{0.95}Pd_{0.05}O_{2-\delta}$. Dry reforming is not the sole mechanism by which excess H_2 is produced.

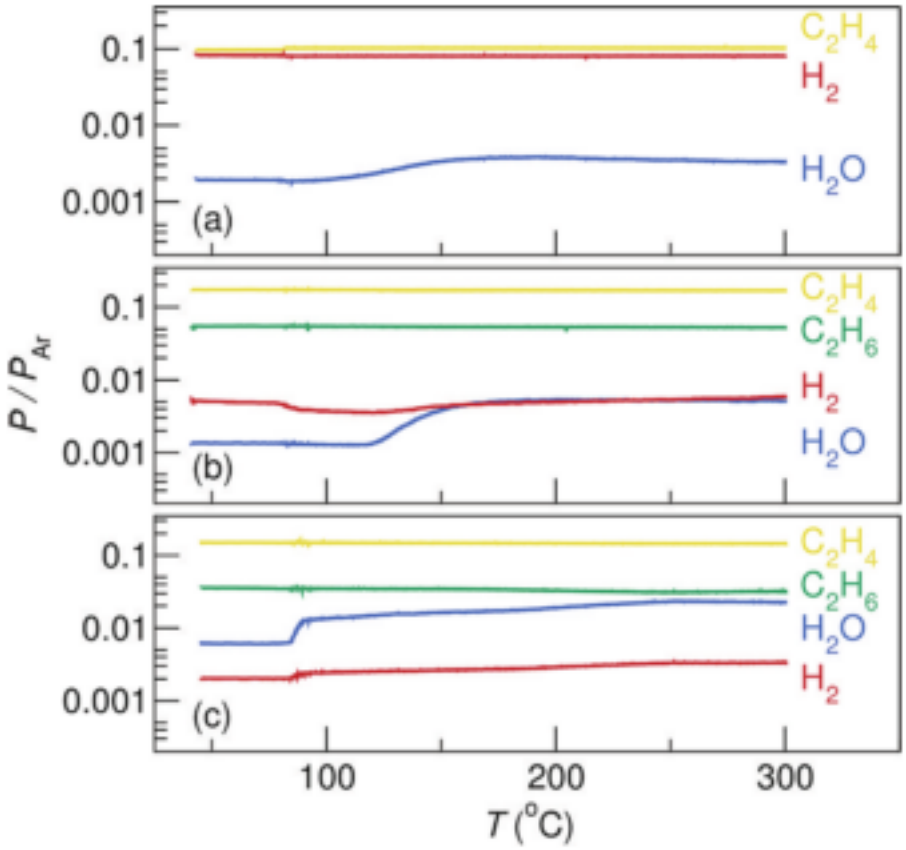

Figure 9. Ethylene hydrogenation (1:1 C_2H_4/ H_2) in Ar heated at 10 °C/min to 300 °C over (a) CeO_2 , (b) prereduced (20% H_2 in Ar to 300 °C 1 h) $Ce_{0.95}Pd_{0.05}O_{2-\delta}$, (c) prereduced (20% H_2 in Ar to 300 °C 1 h) PdO/CeO_2 . The reduced Pd substituted catalyst is active for a reaction known to take place on Pd metal and performs similarly to the supported Pd catalyst.

To further probe the mechanism by which partial oxidation of CH_4 over $Ce_{0.95}Pd_{0.05}O_{2-\delta}$ produces excess H_2 a steady state reaction was performed. While the gas ratios for partial

oxidation remained the same, the temperature ramp was changed to allow the catalyst to come to steady state at each temperature stage before continuing. The temperature ramping for the steady state reaction was 1 h dwells in 50 °C increments starting at 400 °C, increasing to 600 °C, and back down again. As shown in Figure 7, the steady state reaction clearly shows consumption of water during partial oxidation of CH_4, suggesting steam reforming. Along with the consumption of water, more CO_2 is produced than expected. This is likely a result of the water-gas shift reaction. The excess H_2 observed during partial oxidation of CH_4 over $Ce_{0.95}Pd_{0.05}O_{2-\delta}$ also likely results from a combination of some dry reforming, steam reforming, and water gas shift reactions. The long time steady state reaction for partial oxidation of methane over $Ce_{0.95}Pd_{0.05}O_{2-\delta}$ was carried out for 24 h at 600 °C.

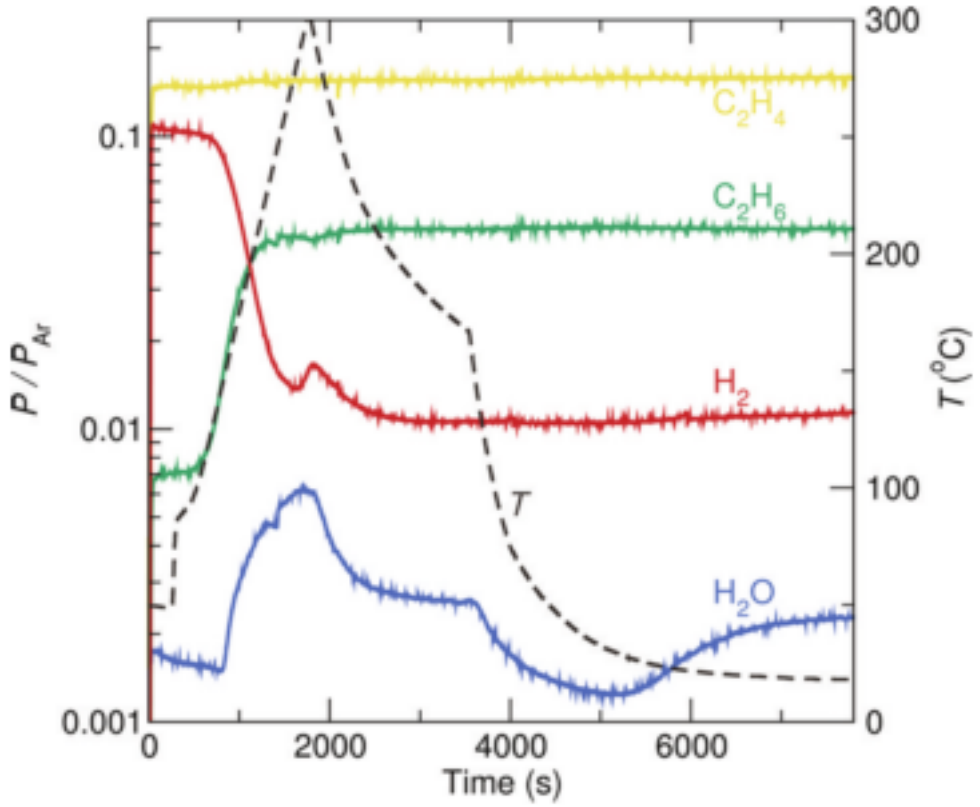

Figure 10. Ethylene hydrogenation (1:1 C_2H_4/ H_2) over as-prepared $Ce_{0.95}Pd_{0.05}O_{2-\delta}$ heated at 10 °C/min to 300 °C. The material becomes active and produces C_2H_6 only once the material become sufficiently reduced around 120 °C, further confirming that the catalytically active form of this material is Pd supported on CeO_2 .

To explain why prereduction causes this catalyst to become active at a slightly lower temperature than the preoxidized sample, we chose to further investigate how reducing conditions affected this material. Synchrotron powder XRD of the prereduced catalyst in Figure 4 distinctly shows fcc-Pd in addition to cubic CeO_2. It appears that Pd-substituted CeO_2 becomes Pd supported on CeO_2 under reducing conditions, and this is the catalytically active phase for C−H bond activation. Pd-substituted CeO_2 is not active for C−H bond activation. To confirm that the substituted material behaves like Pd metal under reaction conditions, partial oxidation was recorded for a prereduced sample of PdO supported on CeO_2 (Figure 6d). Partial oxidation of CH_4 over Pd metal supported on CeO_2 shows identical reaction character to partial oxidation over the Pd-substituted CeO_2 , but with activity for excess hydrogen production igniting at about 400 °C as opposed to about 450 °C in Pd-substituted CeO_2 .

The reaction character observed for partial oxidation and dry reforming of methane over Pd-substituted CeO_2 is in contrast to that Pt-substituted CeO_2 . Partial oxidation of methane over Pt-substituted CeO_2 does produce stoichiometric synthesis gas between 450 and 500 °C, while Pd-substituted CeO_2 produces nonstoichiometric synthesis gas in the form of excess H_2. Pt- substituted CeO_2 is also active for dry reforming of methane to synthesis gas with relatively high conversion, while Pd-sub ceria produces nonstoichiometric synthesis gas with a very low yield. Pd-substituted CeO_2 likely undergoes several secondary reactions

during partial oxidation of methane, including dry reforming of methane, water-gas shift, and steam reforming of methane.

The synchrotron powder diffraction pattern was collected for postreaction $Ce_{0.95}Pd_{0.05}O_{2-\delta}$ mixed with Al_2O_3. Just as *fcc*-Pd was seen in the reduced material (Figure 4), so too is this phase observed in the diffraction pattern shown in Figure 8 along with the γ-Al_2O_3 diluent. We took special care to cool the material in an inert atmosphere after becoming active under reaction conditions. The material was also handled carefully, quickly contained, and promptly sent for characterization. We recognize that some reoxidation may take place but the fcc- Pd phase is very clearly seen in the postreaction material. Certainly no PdO phase is observed in the postreaction material. Moreover, the fact that the catalytic behavior matches that of Pd/CeO_2 further supports that the postreaction material does contain Pd metal. The correlation length of fcc-Pd determined from synchrotron XRD and the Scherrer line broadening equation is near 7 nm for postreaction $Ce_{0.95}Pd_{0.05}O_{2-\delta}$ and near 100 nm for the as-prepared Pd/ CeO_2 used for comparison. However, it should be noted that the Scherrer line broadening equation does not provide the most accurate measure of coorelation length at these length scales. It seems that the catalytically active phase of $Ce_{0.95}Pd_{0.05}O_{2-\delta}$ for partial oxidation of CH_4 is actually the reduced Pd supported on CeO_2 . Other reactions and chemical probes were considered to determine the presence of metallic Pd in this catalyst.

It would appear that Pd-substituted CeO_2 becomes Pd supported on CeO_2 under reaction conditions. Since Pd supported on oxides is capable of catalyzing ethylene hydrogenation, we performed ethylene hydrogenation over $Ce_{0.95}Pd_{0.05}O_{2-\delta}$.[53] As seen in Figure 9a, no ethane was produced over unsubstituted CeO_2 . However, ethane was produced over

prereduced $Ce_{0.95}Pd_{0.05}O_{2-\delta}$ at room temper- ature (Figure 9b). Increasing the temperature did not increase the ethylene conversion in this reaction. The same behavior was observed for reduced PdO/CeO_2 (Figure 9c). It is interesting to note that there appears to be a slightly higher selectivity toward ethane production for reduced $Ce_{0.95}Pd_{0.05}O_{2-\delta}$ δ than the reduced PdO/CeO_2 used for comparison. To confirm that this reaction proceeds over Pd metal supported on CeO_2 , and not the as-prepared $Ce_{0.95}Pd_{0.05}O_{2-\delta}$, we attempted ethylene hydrogenation without a prereduction. The catalyst does not become active until it becomes sufficiently reduced by the ethylene and hydrogen flowing over the catalyst. Figure 10 shows that at around 110 °C the catalyst was reduced to Pd metal supported on CeO_2 at which point ethylene was converted to ethane. The catalyst continued to actively produce ethane while it was cooled back to room temperature.

Pd-substituted CeO_2 catalysts have been successfully prepared via USP with a surface area of 32 m^2/g and hollow sphere morphology. These materials are phase pure up to 10 mol % Pd substitution. This material becomes catalytically active for C−H bond activation only after the Pt2+ ions have been reduced to Pd metal supported on CeO_2. Partial oxidation of CH_4 over $Ce_{0.95}Pd_{0.05}O_{2-\delta}$ yields the expected combustion products along with nonstiochiometric synthesis gas in the form of excess hydrogen gas. The excess hydrogen is a result of several secondary reactions occurring after combustion, including dry reforming of CH_4, steam reforming of CH_4, and water gas shift. The catalytically active phase for this material is Pd supported on CeO_2, confirmed by the ethylene hydrogenation reaction. Additionally, we have identified USP as an adequate method for the preparation of substituted metal oxides and potentially for the preparation of well-dispersed metal nanoparticles on oxide supports upon reduction.

References

(1) Crabtree, R. H. The organometallic chemistry of the transition metals; John Wiley & Sons Inc: New York, 2009; p 505.

(2) Thomas, J. M. J. Chem. Phys. 2008, 128, 182502.

(3) Hegde, M. S.; Madras, G.; Patil, K. C. Acc. Chem. Res. 2009, 42, 704−712.

(4) Bera, P.; Priolkar, K. R.; Gayen, A.; Sarode, P. R.; Hegde, M. S.; Emura, S.; Kumashiro, R.; Jayaram, V.; Subbanna, G. N. Chem. Mater. 2003, 15, 2049−2060. 5438

(5) Baidya, T.; Marimuthu, A.; Hegde, M. S.; Ravishankar, N.; Madras, G. J. Phys. Chem. C 2007, 111, 830−839.

(6) Datye, A.; Bravo, J.; Nelson, T.; Atanasova, P.; Lyubovsky, M.; Pfefferle, L. Appl. Catal., A 2000, 198, 179−196.

(7) Singh, U.; Li, J.; Bennett, J.; Rappe, A.; Seshadri, R.; Scott, S. J. Catal. 2007, 249, 349−358.

(8) Li, J.; Singh, U. G.; Bennett, J. W.; Page, K.; Weaver, J. C.; Zhang, J.-P.; Proffen, T.; Rappe, A. M.; Scott, S.; Seshadri, R. Chem. Mater. 2007, 19, 1418−1426.

(9) Li, J.; Singh, U. G.; Schladt, T. D.; Stalick, J. K.; Scott, S. L.; Seshadri, R. Chem. Mater. 2008, 20, 656

7−6576.

(10) Nishihata, Y.; Mizuki, J.; Akao, T.; Tanaka, H.; Uenishi, M.; Kimura, M.; Okamoto, T.; Hamada, N. Nature 2002, 418, 164−167.

(11) Ribeiro, F.; Chow, M. J. Catal. 1994, 146, 537−544.

(12) Escandon, L.; Ordonez, S.; Vega, A. Chemosphere 2005, 58, 9− 17.

(13) Hicks, R.; Qi, H.; Young, M. J. Catal. 1990, 122, 280−294.

(14) Basile, A.; Paturzo, L. Catal. Today 2001, 67, 65−75.

(15) Cullis, C. F.; Nevell, T. G.; Trimm, D. L. J. Chem. Soc., Faraday Trans. 1 1972, 68, 1406.

(16) Muller, C.; Maciejewski, M.; Koeppel, R.; Baiker, A. J. Catal. 1997, 166, 36−43. (17) Muller, C.; Maciejewski, M.; Koeppel, R.; Baiker, A. Catal. Today 1999, 47, 245−252.

(18) Ciuparu, D.; Altman, E.; Pfefferle, L. J. Catal. 2001, 203, 64−74.

(19) Groppi, G.; Cristiani, C.; Lietti, L.; Ramella, C.; Valentini, M.; Forzatti, P. Catal. Today 1999, 50, 399−412.

(20) Carstens, J.; Su, S.; Bell, A. J. Catal. 1998, 176, 136−142.

(21) Strobel, R.; Grunwaldt, J.; Camenzind, A.; Pratsinis, S.; Baiker, A. Catal. Lett. 2005, 104, 9−16.

(22) Grunwaldt, J.-D.; Maciejewski, M.; Baiker, A. Phys. Chem. Chem. Phys. 2003, 5, 1481−1488.

(23) Persson, K.; Ersson, A.; Jansson, K.; Iverlund, N.; Jaras, S. J. Catal. 2005, 231, 139−150.

(24) Roy, S.; Hegde, M. S.; Ravishankar, N.; Madras, G. J. Phys. Chem. C 2007, 111, 8153−8160.

(25) Roy, S.; Marimuthu, A.; Hegde, M. S.; Madras, G. Appl. Catal., B 2007, 73, 300−310.

(26) Bera, P. J. Catal. 2000, 196, 293−301.

(27) Baidya, T.; Dutta, G.; Hegde, M. S.; Waghmare, U. V. Dalton Trans. 2008, 455.

(28) Roy, S.; Hegde, M. S.; Madras, G. Appl. Energy 2009, 86, 2283− 2297.

(29) Singh, P.; Hegde, M. S. J. Solid State Chem. 2008, 181, 3248− 3256.

(30) Gupta, A.; Waghmare, U. V.; Hegde, M. S. Chem. Mater. 2010, 22, 5184−5198. (31) Baidya, T.; Gayen, A.; Hegde, M. S.; Ravishankar, N.; Dupont, L. J. Phys. Chem. B 2006, 110, 5262−5272.

(32) Baidya, T.; Gupta, A.; Deshpandey, P. A.; Madras, G.; Hegde, M. S. J. Phys. Chem. C 2009, 113, 4059−4068.

(33) Scanlon, D. O.; Morgan, B. J.; Watson, G. W. Phys. Chem. Chem. Phys. 2011, 13, 4279.

(34) Haneda, M.; Mizushima, T.; Kakuta, N. J. Phys. Chem. B 1998, 102, 6579−6587.

(35) Ciuparu, D.; Bozon-Verduraz, F.; Pfefferle, L. J. Phys. Chem. B 2002, 106, 3434−3442.

(36) Fu, Q. Science 2003, 301, 935−938.

(37) Gorte, R.; Zhao, S. Catal. Today 2005, 104, 18−24.

(38) Sharma, S.; Deshpande, P. A.; Hegde, M. S.; Madras, G. Ind. Eng. Chem. Res. 2009, 48, 6535−6543.

(39) Kao, L. C.; Hutson, A. C.; Sen, A. J. Am. Chem. Soc. 1991, 113, 700−701.

(40) Lunsford, J. Catal. Today 2000, 63, 165−174.

(41) Bradford, M.; Vannice, M. Catal. Rev. 1999, 41, 1−42.

(42) Tang, W.; Hu, Z.; Wang, M.; Stucky, G. D.; Metiu, H.; McFarland, E. W. J. Catal. 2011, 273, 125−137.

(43) Skrabalak, S. E.; Suslick, K. S. J. Am. Chem. Soc. 2006, 128, 12642−12643.

(44) Bérar, J.; Baldinozzi, G. Procedures for the refinement of incommensurate structures using XND. Coding issues for the refinement of incommensurate structures In Newsletter No. 5, Commission on Crystallographic Computing; Billinge, S., Chapuis, G., Cranswick, L.. Lifshitz, R., Eds.; International Union of Crystallog- raphy, 2005; pp 5−9.

(45) Palosz, B.; Grzanka, E.; Gierlotka, S.; Stel makh, S.; Pielaszek, R.; Bismayer, U.; Neuefeind, J.; Weber, H. P.; Proffen, T.; Dreele, Von, R.; Palosz, W. Z. Kristallogr. 2002, 217, 497−509.

(46) Palosz, B.; Grzanka, E.; Gierlotka, S.; Stel'makh, S.; Pielaszek, R.; Lojkowski, W.; Bismayer, U.; Neuefeind, J.; Weber, H. P.; Palosz, W. GPHT 2003, 76, 171−185.

(47) Palosz, B.; Grzanka, E.; Gierlotka, S.; Stelmakh, S. Z. Kristallogr. 2010, 225, 588−598.

(48) Williamson, G.; Hall, W. Acta Metall. 1953, 1, 22−31.

(49) Baidya, T.; Priolkar, K. R.; Sarode, P. R.; Hegde, M. S.; Asakura, K.; Tateno, G.; Koike, Y. J. Chem. Phys. 2008, 128, 124711.

(50) Priolkar, K. R.; Bera, P.; Sarode, P. R.; Hegde, M. S.; Emura, S.; Kumashiro, R.; Lalla, N. P. Chem. Mater. 2002, 14, 2120−2128.

(51) Brun, M.; Berthet, A.; Bertolini, J. J. Electron Spectrosc. 1999, 104, 55−60.

(52) Singh, P.; Hegde, M. S. Cryst. Growth Des. 2010, 10, 2995− 3004.

(53) McGown, W. T.; Kemball, C.; Whan, D. A.; Scurrell, M. S. J. Chem. Soc., Faraday Trans. 1: 1977, 73, 632−647.